

UNIVERSITY OF CALIFORNIA,
IRVINE

**Acoustically Enhanced Ganglia Mobilization in the Presence
of Colloids**

DISSERTATION

submitted in partial satisfaction of the requirements for the degree of

DOCTOR OF PHILOSOPHY

in Civil Engineering

by

John Matthew Thomas

Dissertation Committee:
Professor Brett F. Sanders, Chair
Professor William J. Cooper
Professor Soroosh Soroshian

2009

The dissertation of John Matthew Thomas
is approved and is acceptable in quality and form for
publication on microfilm and in digital formats:

Committee Chair

University of California, Irvine

2009

Dedication

To my amazing wife and best friend Hayley Dawn Thomas. We did it!!!

Contents

LIST OF TABLES	viii
LIST OF FIGURES	ix
NOMENCLATURE	xii
ACKNOWLEDGMENTS	xv
CURRICULUM VITAE	xvi
ABSTRACT OF THE DISSERTATION	xxii
1 INTRODUCTION	1
1.1 Significance of Research	1
1.1.1 The DNAPL Problem	1
1.1.2 Conventional Remediation Methods	2
1.1.3 Alternative Remediation Methods	2
1.1.4 Acoustic Waves For Remediation	3
1.1.5 Colloids In The Subsurface Environment	4
1.2 Research Objectives	5

2	LITERATURE REVIEW	6
2.1	Acoustic Wave Propagation	6
2.1.1	Wave Propagation In Saturated Porous Media	6
2.1.2	Effects of Acoustics on Pore Fluid	8
2.1.3	Effects of Acoustics on Solute Transport	8
2.1.4	Effects of Acoustics on NAPL Ganglia	9
2.1.5	Effects of Acoustics on Colloid Transport	9
2.2	Physicochemical Characteristics of Colloids	10
2.2.1	Physical Structure of Colloids	10
2.2.2	Surface Chemistry	11
2.3	Transport and Deposition of Colloids	11
2.3.1	Solution Chemistry	13
2.3.2	Physicochemical Properties of Porous Media	13
2.4	Colloid-Facilitated Contaminant Transport	14
3	ACOUSTICALLY ENHANCED COLLOID TRANSPORT	16
3.1	Chapter Abstract	16
3.2	Mathematical Model Development	17
3.3	Experimental Design and Procedures	28
3.3.1	Physical Description of Apparatus	28
3.3.2	Experimental Procedure	32
3.3.3	Tracer Properties	35
3.3.4	Method of Sample Analysis	38

3.4	Results and Discussion	44
3.4.1	Determination of Column Parameters	44
3.4.2	Effects of Various Model Parameters	45
3.4.3	Experimental Results	48
3.5	Conclusions	53
4	NEW EXPERIMENTAL METHODS	58
4.1	Chapter Abstract	58
4.2	Introduction	59
4.3	Methodology	62
4.3.1	Fabrication of Sintered-Glass-Bead Column	62
4.3.2	Photographic Methods	67
4.3.3	Image Processing	68
4.4	Calibration	70
4.4.1	Mass Scaling	72
4.4.2	Optical Dispersion Correction	73
4.5	Verification	75
5	INVESTIGATION OF MECHANISMS	77
5.1	Chapter Abstract	77
5.2	Introduction	78
5.3	Experimental Design and Procedures	79
5.4	Results and Discussion	80

5.4.1	Parametric Investigation	80
5.4.2	Experimental Results	83
5.5	Conclusions	88
5.5.1	Scale Dependency	89
6	ACOUSTICALLY ENHANCED GANGLIA DISSOLUTION WITH COLLOIDS	98
6.1	Chapter Abstract	98
6.2	Introduction	99
6.3	Experimental Design and Procedures	99
6.4	Preliminary Results and Discussion	100
6.5	Future Processing	101
	REFERENCES	106

List of Tables

3.1	Water Purity Parameters	33
3.2	Emission Scan Settings	56
3.3	Column Parameters	57

List of Figures

1.1	The Persistence of DNAPL and LNAPL In Ground Water	2
3.1	Photographs of Syringe Injector Before and After Injection	29
3.2	Schematic of Column, Bead Pack, Screen, Endcap, and Retainer	30
3.3	Experimental Apparatus	31
3.4	Top-down Detail of Pressure Transducer, Plunger, Diaphragm, and Acoustic Reservoir	32
3.5	Schematic of AB2 Luminescence Spectrometer Performing An Emis- sion Scan	39
3.6	Shifted Curves for Confidence Measurements	42
3.7	The Effects of Average Interstitial Velocity On the Analytical Solution	45
3.8	The Effects of Hydrodynamic Dispersion On the Analytical Solution .	46
3.9	The Effects of Forward Rate Constant On the Analytical Solution . .	47
3.10	The Effects Reverse Rate Constant On the Analytical Solution	48
3.11	Experimental Data and Fitted Solution For Uranine and Colloids For the Base Case (No Acoustic Pressure)	50
3.12	Experimental Data and Fitted Solution For Uranine, Blue, and Red Microspheres at Base Case, 30 Hz, and 110 Hz	51

3.13	Attenuation of Acoustic Pressure Along the Column at Different Frequencies	52
3.14	Acoustic Component of Velocity	53
3.15	Acoustic Component of Dispersion	54
3.16	Acoustic Component of Effective Dispersion	55
4.1	Furnace Temporal-Variation Sintering Program	64
4.2	Column-Mold Assembly For Sintering	66
4.3	Images From an Experiment With Intensity Curve	71
4.4	Intensity Curve and Calibrated Concentration Curve	74
4.5	First Moment Versus Time	76
5.1	Effects of Interstitial Velocity On the <i>In Situ</i> Analytical Solution	80
5.2	Effects of Hydrodynamic Dispersion On the <i>In Situ</i> Analytical Solution	81
5.3	Effects of Clogging Rate Constant On the <i>In Situ</i> Analytical Solution	82
5.4	Combined Effects of Clogging and Declogging Rate Constants On the <i>In Situ</i> Analytical Solution	83
5.5	Mass-Corrected Concentration Data and Fitted Curves	84
5.6	Calibrated Concentration Data and Fitted Curves	85
5.7	Uranine Concentration Curves	86
5.8	Fitted Effective Interstitial Velocity With Error Versus Frequency - Separated	91
5.9	Fitted Effective Interstitial Velocity Versus Frequency - Combined	92
5.10	Acoustic Component of Interstitial Velocity Versus Frequency - Combined	93

5.11	Effective Hydrodynamic Dispersion Versus Frequency	94
5.12	Effective Interstitial Velocity Versus Influent Pressure	95
5.13	Attenuation Versus Acoustic Frequency	96
5.14	Attenuation Versus Influent Acoustic Pressure	97
6.1	Adobe Illustrator Mask File of Pore Geometry	102
6.2	Fabrication of Etched-Glass Micromodels	103
6.3	The Finished Network Micromodel	104
6.4	TCE Injected Into Micromodel	104
6.5	TCE Mobilization Due to Acoustic Source	105

Nomenclature

a	dummy variable.
A	cross-sectional area of column, $[\text{L}^2]$.
\mathcal{A}	defined in (3.7).
b	dummy variable.
\mathcal{B}	defined in (3.8).
c	dummy variable.
C	concentration of colloids in suspension, $[\text{M}/\text{L}^3]$.
C^*	mass of colloids adsorbed, $[\text{M}/\text{M}]$.
d	dummy variable.
D	hydrodynamic dispersion coefficient, $[\text{L}^2/\text{t}]$.
D_e	effective hydrodynamic dispersion coefficient, $[\text{L}^2/\text{t}]$.
D^*	component of dispersion attributed to acoustics, $[\text{L}^2/\text{t}]$.
\mathcal{D}	molecular diffusion coefficient, $[\text{L}^2/\text{t}]$.
\mathcal{D}_e	effective molecular diffusion coefficient, $[\text{L}^2/\text{t}]$.
f	arbitrary function.
h	dummy variable.
\mathcal{H}	defined in (3.9).
I_1	Modified Bessel function of order one, [-].
k_c	forward rate coefficient, $[1/\text{t}]$.
k_r	reverse rate coefficient, $[\text{M}/\text{L}^3/\text{t}]$.
l	dummy variable.
L	column length, $[\text{cm}]$.

\mathcal{L}	Laplace transform, [-].
\mathcal{L}^{-1}	inverse Laplace transform, [-].
M	defined in (3.22).
M_0	mass injected over cross-section of column, [M/L ²].
M_{beads}	mass of glass beads in column, [M].
M_{inj}	mass injected, [M].
N	defined in (3.22).
P_1	influent acoustic pressure, [kPa].
P_2	effluent acoustic pressure, [kPa].
ΔP	acoustic pressure gradient, [kPa/cm].
q	seepage velocity, [L/t].
Q	volumetric flow rate, [L ³ /t].
r_1	forward rate coefficient, [1/t].
r_2	reverse rate coefficient, [M/L ³ /t].
s	Laplace time variable, [-].
t	time, [t].
u	dummy variable.
U	average interstitial fluid velocity, [L/t].
U_e	effective interstitial fluid velocity, [L/t].
U^*	component of velocity attributed to acoustics, [L/t].
V_{beads}	volume of beads, [L ³].
V_{total}	total volume of solid matrix, [L ³].
V_{voids}	volume of void space, [L ³].
x	longitudinal spatial coordinate, [L].

Greek Letters

α_1	dummy variable.
α_2	dummy variable.
α_L	longitudinal dispersivity, [L].
γ	Laplace space variable, [-].
δ	Dirac delta function, [1/t].

ζ	dummy integration variable.
θ	porosity (void volume/total volume), $[\text{L}^3/\text{L}^3]$.
Θ	defined in (3.34).
λ	inactivation constant of suspended colloids, $[\text{t}^{-1}]$.
λ^*	inactivation constant of adsorbed colloids, $[\text{t}^{-1}]$.
π	constant, [-].
ρ	bulk density of the solid matrix, $[\text{M}/\text{L}^3]$.
τ	dummy integration variable.
τ^*	tortuosity, [-].
Φ	defined in (3.49).
Ω	defined in (3.58).

Acknowledgments

First, I want to thank my loving and beautiful bride, Hayley Dawn. She put up with many hours of me working late in the lab or typing late into the night after she went to bed. I could never have done this without you. I want to thank my first advisor Dr. Costas Chrysikopoulos who gave me the necessary guidance and prodding to finish. Your patience is greatly appreciated. I also sincerely thank Dr. Brett Sanders who has served as my advisor for the past several years. You have gone above and beyond the call of duty to help me out. Thanks to Drs. Bill Cooper and Soroosh Sorooshian for serving on my committee. Thanks to Drs. Russ Detwiler and Diego Rosso for your help and encouragement. Thanks to my officemates, especially Zach Scott, Matt Zwartjes, Humberto Gallegos, Timu Gallien, and Linda Tseng all of whom both encouraged me and shared in the pain. There's just something about knowing that you're not the "only one". Thanks to my family and many friends who stood by me and supported me through all the difficult times. Without all of you, I quite literally would not have made it. Thanks especially to Marc Shay who has been there for me time after time through the past several years. Thanks to Dr. Eric Vogler who was of invaluable help in the laboratory and in learning the ropes of university politics. Thanks to Steve Bowen who convinced me not only that I could, but also that I should go to graduate school. The value of your love, compassion, encouragement, advice, and admonishment cannot be overstated. My sincerest thanks! Thanks to the Department of Civil and Environmental Engineering at UCI and the ARCS Fellowship people for the financial support that enabled me to finish this work.

CURRICULUM VITAE

Matt Thomas

Department of Civil & Environmental Engineering
UNIVERSITY OF CALIFORNIA, IRVINE, CA 92697

(949) 232-3923 cell

(949) 824-7711 office

jmthomas@uci.edu

EDUCATION

- Doctor of Philosophy: Civil Engineering, Water Resources, June 2009
UNIVERSITY OF CALIFORNIA, IRVINE
Dissertation: Acoustically Enhanced Ganglia Mobilization
in the Presence of Colloids
- Master of Science: Civil Engineering, Water Resources, March 2005
UNIVERSITY OF CALIFORNIA, IRVINE
Thesis: Acoustically Enhanced Colloid Transport In
Saturated Porous Media
- Bachelor of Science: Environmental Engineering, September 2002
UNIVERSITY OF CALIFORNIA, IRVINE

AWARDS AND HONORS

- American Geophysical Union (AGU) Student Travel Grant, 2008
Civil Engineers and Land Surveyors of California (CELSOC) Scholarship, 2006

Achievement Rewards For College Scientists (ARCS) Foundation Fellow, 2005, 2006
Fariborz Maseeh Fellow, 2004
NSF Foundation Undergraduate Scholarship Recipient, 2001

TEACHING EXPERIENCE

Introduction to Fluid Mechanics - CEE170 (F02, F05, F07)
Introduction to Environmental Chemistry - CEE162 (W03, W04)
Water and Wastewater Treatment - CEE161 (S03)
Groundwater Hydrology - CEE172 (F03)
Infrastructure Hydraulics Lab - CEE171 (W06, W07, W08, W09)
Engineering Problem Solving - CEE20 (S06, S08, S09)

EMPLOYMENT

- (06/07-present) ENGINEER INTERN, Fuscoe Engineering, Irvine, California
- Created primary soil sampling plan for MCAS El Toro (Superfund Site) - the location for the Orange County Great Park.
 - Conducted groundwater modeling to ensure compliance with Navy's currently active remediation.
- (01/07-04/07) TEACHING ASSISTANT, Department of Civil and Env. Engineering, University of California, Irvine, California
- (09/05-06/06) TEACHING ASSISTANT, Department of Civil and Env. Engineering, University of California, Irvine, California
- (08/05-09/05) ENGINEER, Boyle Engineering Corp., Newport Beach, California
- Acquired groundwater well sampling data from various water agencies and water districts.
 - Created integrated database utilizing USGS, water district, and privately owned well data for groundwater modeling.

- (01/03-05/04) ENGINEER, Boyle Engineering Corp., Newport Beach, California
- Conducted search and study of nitrate/nitrite contamination from septic systems for litigation purposes.
- (09/02-03/04) TEACHING ASSISTANT, Department of Civil and Env. Engineering, University of California, Irvine, California
- (9/02-12/02) RESEARCH ASSISTANT, University of California, Irvine California
- (07/01-01/03) ENGINEER INTERN, TRC Solutions, Irvine, California
- Generated, edited, and assured quality control of operations and maintenance reports for dual-phase hydrocarbon remediation systems.
 - Reviewed permits and sampling schedules and directed field technicians to ensure NPDES/AQMD permit compliance.
 - Interacted with engineers and geologists to recommend hydrocarbon remediation strategies.

JOURNAL PUBLICATIONS

THOMAS, J. M., and C. V. CHRYSIKOPOULOS, Experimental investigation of acoustically enhanced colloid transport in water-saturated packed columns, *J. Colloid Interface Sci.*, 308, 200-207, doi:10.1016/j.jcis.2006.12.062, 2007.

PUBLICATIONS UNDER REVIEW

THOMAS, J. M., and C. V. CHRYSIKOPOULOS, A new method for *in situ* concentration measurements in packed-column transport experiments. *Environ. Sci. Technol.*, 2009.

PUBLICATIONS UNDER PREPARATION

THOMAS, J. M., and C. V. CHRYSIKOPOULOS, Acoustically-enhanced transport, dissolution, and mobilization in porous media: a review of methods and results.

THOMAS, J. M., and C. V. CHRYSIKOPOULOS, Experimental determination of the mechanisms responsible for acoustically enhanced transport in water-saturated packed columns.

THOMAS, J. M., and C. V. CHRYSIKOPOULOS, Acoustically enhanced NAPL ganglia mobilization and dissolution in the presence of colloids.

CONFERENCE PUBLICATIONS

THOMAS, J. M., and C. V. CHRYSIKOPOULOS, Investigation of acoustically enhanced colloid transport in water-saturated packed columns, (paper), *Protection and Restoration of the Environment VIII, Chania, Greece*, FTP_17, 2006.

POSTER PRESENTATIONS

THOMAS, J. M., and C. V. CHRYSIKOPOULOS, A new method for accurate *in situ* concentration measurements in packed columns, (poster), *EGU, European Geoscience Union General Assembly 2009 Vienna, Austria*, HS3-3527-4, 2009.

THOMAS, J. M., and C. V. CHRYSIKOPOULOS, Experimental determination of the mechanisms responsible for acoustically enhanced contaminant transport in water-saturated packed columns, (poster), *AGU, American Geophysical Union Fall Meeting 2008 San Francisco, California*, H21D-0846, 2008.

THOMAS, J. M., and C. V. CHRYSIKOPOULOS, Experimental investigation of acoustically enhanced colloid transport in water-saturated packed columns, (poster), *EGU, European Geoscience Union General Assembly 2007 Vienna, Austria*, HS7-1FR2P-0084, 2007.

THOMAS, J. M., and C. V. CHRYSIKOPOULOS, Investigation of acoustically enhanced colloid transport in water-saturated packed columns, (poster), *Protection and Restoration of the Environment VIII, Chania, Greece*, FTP_17, 2006.

THOMAS, J. M., and C. V. CHRYSIKOPOULOS, Experimental investigation of acoustically enhanced colloid transport in water-saturated packed columns, (poster), *AGU, American Geophysical Union Fall Meeting 2005 San Francisco, California*, H23F-1492, 2005.

SCIENTIFIC AND PROFESSIONAL SOCIETY MEMBERSHIPS

American Geophysical Union (AGU)

American Society of Civil Engineers (ASCE)

Urban Water Research Center (UWRC)

ACTIVITIES

President: Intercollegiate Christian Club, UC Irvine Chapter, 2000-2002

Volunteer: HOPE Worldwide/HOPE Youth Corps

REFERENCES

Professor Brett Sanders, Ph.D.

Dept. Civil & Environmental Engineering

University of California, Irvine

Irvine, CA 92697-2175

(949) 824-4327 Office

(949) 824-3672 Fax

email: bsanders@uci.edu

Professor Constantinos Chrysikopoulos, Ph.D.

Dept. Civil Engineering

University of Patras
26500 Patras, GREECE
+011(30) 2610 996.531 Office
+011(30) 6945 373.208 Cell
email: gios@upatras.gr

Hooshang Nezafati, Ph.D., P.E.
Worley Parsons
3901 Via Oro Ave #100
Long Beach, CA 90810
(714) 379-1157 Office
(949) 933-7884 Cell
email: Hooshang.Nezafati@worleyparsons.com

Abstract of The Dissertation

Acoustically Enhanced Ganglia Mobilization in the Presence of Colloids

by

John Matthew Thomas

Doctor of Philosophy in Civil Engineering

University of California, Irvine, 2009

Professor Brett F. Sanders, Chair

Due to their toxicity and persistence in the subsurface environment, dense non-aqueous phase liquids (DNAPLs) continue to be an important area of research for contaminated groundwater remediation technologies. New remediation techniques utilizing acoustic waves have recently received attention. However, these studies do not consider colloids, which are ubiquitous in groundwater aquifers, may act as mobile sorption sites for DNAPLs, or may be used in some cases for remediation themselves. The focus of this work was to investigate the effects of acoustic waves on colloid transport and deposition in porous media and the effects of colloids on NAPL ganglia dissolution and mobilization in the presence of acoustic waves. These effects have not previously been investigated to the knowledge of the author.

In Chapter 3, a series of packed-column experiments in the presence of acoustic waves ranging in frequency from 0 to 150 Hz was performed to determine their effects on colloid transport. An analytical model was formulated to quantify the effects and a parametric study performed. Due to a number of inherent weaknesses in stan-

dard packed-column effluent analysis the mechanisms responsible for the observations could not be specifically addressed.

Chapter 4 details a new experimental method including a new apparatus design, photographic procedures, and quantification method aimed at overcoming the weaknesses in order to explore the mechanisms responsible for the observations.

In Chapter 5, the new method is employed in a series of packed-column laboratory experiments in order to increase our understanding of the mechanisms responsible for the observed effects. A number of possible mechanisms are included and discussed and new empirical mathematical models are suggested.

Finally, in Chapter 6, new etched-glass porous-media micromodels were constructed and utilized in experiments to explore the additional effects of adding colloid suspensions to NAPL dissolution/mobilization experiments with acoustic waves. The results presented are preliminary and directions for future research is discussed. More detailed and specific abstracts are included in each chapter.

Chapter 1

INTRODUCTION

1.1 Significance of Research

1.1.1 The DNAPL Problem

Groundwater aquifers are often contaminated by light and dense non-aqueous phase liquids (LNAPLs and DNAPLs) such as gasoline, fuel additives, and solvents such as TCE, and PCE, that enter the ground from leaking storage tanks, leaking pipelines, accidental spills, or unregulated disposal [Gross *et al.*, 2003; Chrysikopoulos *et al.*, 2002; Bao *et al.*, 2003; Tien and Li, 2002]. LNAPLs are less dense than water and therefore create a floating pool on top of the water table. Because DNAPLs are denser than water they migrate downward through the soil creating a pool when they reach an impermeable layer such as bedrock. Consequently, DNAPL contamination is more difficult to treat. Both LNAPL and DNAPL pools slowly dissolve into flowing groundwater creating a persisting source of contamination. Figure 1.1 demonstrates how these contaminants migrate and persist once they have entered the aquifer. Their low aqueous solubility and persistence in the subsurface make the achievement of complete reclamation impossible in most cases [Gross *et al.*, 2003].

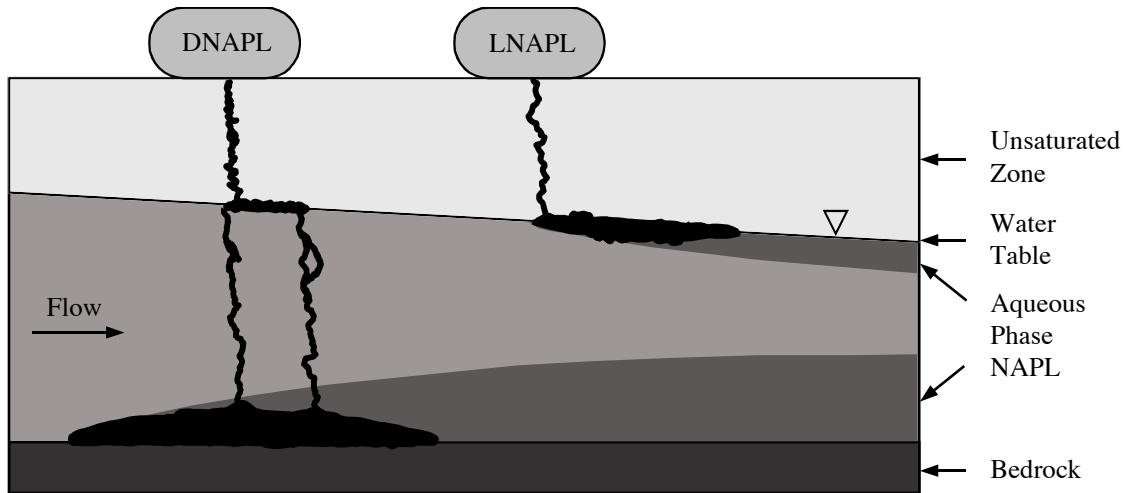


Figure 1.1: DNAPLs and LNAPLs form pools in the aquifer and then slowly dissolve into flowing groundwater creating a lasting contamination source.

1.1.2 Conventional Remediation Methods

The prevalence, toxicity, and mobility of DNAPLs in groundwater aquifers have facilitated development of groundwater remediation technologies. There are a number of available technologies for treatment of DNAPL contaminated groundwater that have been utilized with varying degrees of success: filtration through granular activated carbon (GAC), soil removal and/or washing, air stripping, and biological contact or trickle filtration. Each of these remediation technologies rely heavily on a pump-and-treat methodology such that the amount of contaminant mass removed is proportional to the amount of water pumped from the subsurface and the aqueous solubility of the particular contaminant. Unfortunately, DNAPLs have low aqueous solubilities [Vogler and Chrysikopoulos, 2001], and may have high affinities for adsorption onto the subsurface formation creating a persisting source of contamination.

1.1.3 Alternative Remediation Methods

Various methods have been explored in recent years to enhance contaminant transport and dissolution to address this issue. Some methods involve introduction of

nonindigenous colloids or humic substances, specialized biocolloids, surfactants, or cosolvents. These methods could be problematic as all of the added substances are considered to be either contaminants themselves or undesirable in the drinking water supply. A desired groundwater remediation approach is a ‘clean’ technology that will increase contaminant mass transport and dissolution in porous media with conventional pump-and-treat methods, thereby enhancing remediation without adding further contaminants to the subsurface.

1.1.4 Acoustic Waves For Remediation

An example of such a technology is the introduction of acoustic waves for aquifer remediation, which has recently been given attention. Several preliminary studies have been conducted with promising results. For example, experimental evidence has shown that acoustic waves can increase both mobilization and dissolution in multi-phase systems (i.e. NAPL/water) [*Beresnev and Johnson, 1994; Vogler and Chrysikopoulos, 2004; Chrysikopoulos and Vogler, 2004, 2006*]. Thomas and Narayanan [2002] showed that solute mass transfer is enhanced by several orders of magnitude when the fluid medium is subject to oscillatory motion, even if there is no net total flow over a cycle of oscillation. Experimental evidence has shown that effluent aqueous DNAPL concentration increased with the application of acoustic pressure waves with the greatest dissolution enhancement occurring at different frequencies depending upon the experimental setup [*Vogler and Chrysikopoulos, 2004; Chrysikopoulos and Vogler, 2004, 2006*]. Furthermore, ganglia that were immobile under steady background flow were mobilized when acoustic pressure was added [*Chrysikopoulos and Vogler, 2004, 2006*]. Gross et al. [2003] have suggested that the unique significance and economic potential of introducing pressure waves into an aquifer is in the ability to focus on cleaning groundwater at localized sites, mobilize trapped contaminants, and guide the motion of a contaminant plume by controlling the intensity and direction of the applied pressure. However, none of the studies that have been performed have considered the critical role of colloids in contaminated

groundwater aquifers.

1.1.5 Colloids In The Subsurface Environment

There are a number of reasons colloids must be considered. First, natural colloidal particles (very fine particles that have some linear dimension between 0.001 and 10 micrometers [*Chyrikopoulos and Sim, 1996*]) are ubiquitous in groundwater aquifers, and may significantly affect the subsurface fate and transport of other contaminants. For example, there is substantial evidence from both laboratory and field experiments that colloids are efficient sorbents for contaminants such as heavy metals, nonpolar organic compounds (e.g., DNAPL), and radionuclides [*Um and Papelis, 2002; Mill et al., 1991; McCarthy, 1998*]. Tatalovich et al. [2000] showed that applying humic substances to groundwater contaminated with a DNAPL pool enhanced the mass transfer of DNAPL to the aqueous phase. Second, sites contaminated with DNAPLs may also be contaminated with biological colloids (e.g. bacteria, viruses, or protozoa) or radio colloids (e.g., radionuclides) that are themselves contaminants. Finally, nonindigenous colloids such as ferrous nanoparticles are being studied for use as oxidizing agents for *in situ* DNAPL remediation [*Zhang, 2003*].

Furthermore, experimental evidence has shown that colloids can have a faster breakthrough compared to solute tracers in packed columns (e.g. [*Kretzschmar and Sticher, 1998; Champ and Schroeter, 1988; Enfield et al., 1989; Niehren and Kinzelbach, 1998; Keller et al., 2004*]). This effect is attributed to size exclusion and electrostatic repulsive forces [*Um and Papelis, 2002*]. It is also widely accepted that colloids migrate faster than nonsorbing conservative tracers in natural fractures [*Abdel-Salam and Chrysikopoulos, 1995; Reimus et al., 1995; James and Chrysikopoulos, 2003*]. Failure to include the effects of colloid-associated contaminant transport can lead to drastic underestimation of the extent of contaminant migration. Therefore, understanding the effects of acoustic wave application on both the transport of colloids and the interaction of colloids with DNAPLs in saturated porous media is necessary

before acoustics can be effectively applied for aquifer remediation. However, these effects have not been investigated to the knowledge of the author, and they are the focus of the present work.

1.2 Research Objectives

The critical importance of colloids in groundwater systems and their implications for contaminant transport are discussed more thoroughly in the literature review. The specific objectives of this research are to quantify how acoustic waves affect colloid transport and deposition in porous media, to develop a method for measuring *in situ* colloid and tracer concentrations, to investigate the mechanisms responsible for the observed effects, and to investigate the effects of both acoustic waves and colloids on DNAPL dissolution and mobilization.

Chapter 2

LITERATURE REVIEW

2.1 Acoustic Wave Propagation

Wave propagation in porous media is of interest in many areas of science and engineering. The theory of the phenomenon has been studied extensively in soil mechanics, seismology, earthquake engineering, ocean engineering, geophysics, and many other disciplines [*Corapcioglu and Bear, 1991*]. However, only recently has the concept of using waves for aquifer remediation been given attention. Gross et al. [2003] have suggested that the unique significance of introducing pressure waves (a type of wave including acoustic waves) into an aquifer as well as its economic potential is in the ability to focus on cleaning groundwater at localized sites, mobilize trapped contaminants, and guide the motion of a contaminant plume by controlling the intensity and direction of the applied pressure.

2.1.1 Wave Propagation In Saturated Porous Media

Acoustics is a general term referring to time-varying deformations or vibrations in materials. When the particles of a medium are displaced from their equilibrium positions, while remaining within the elastic limit of the medium, internal (electro-

static) restoration forces and inertia of the particles lead to oscillatory motion of the medium. The atoms in the material move in unison to produce a mechanical wave.

Acoustic waves (pressure waves in the audible frequency range) can propagate as longitudinal waves, shear waves, surface waves, and in thin materials, as plate waves. The waves of interest in saturated porous media are longitudinal and shear waves. In longitudinal waves, the oscillations occur in the direction of wave propagation. Since compression and dilation forces are active in these waves, they are also called pressure or compression waves. Compression waves can be generated in liquids as well as solids because the energy travels through the atomic structure by a series of compression and expansion (rarefaction) movements. In the transverse or shear wave, the particles oscillate at a right angle or transverse to the direction of propagation. Shear waves require a solid material for effective propagation and, therefore, are not effectively propagated in materials such as liquids or gases. Shear waves are relatively weak when compared to longitudinal waves.

Porous media is viewed as a continuum consisting of a solid phase (either compressible or incompressible) and one or more fluids (gases and liquids). The solid phase constitutes the solid matrix with interconnected void space filled by fluids. Both longitudinal and shear waves propagate in the solid phase and longitudinal waves only in the liquid phase. The speed of a wave traveling within the solid or liquid phase is a function of the material properties of the solid or liquid and is therefore different in each. Wave speed is also independent of the amplitude of the acoustic wave. Stress-strain relations for the medium are generally expressed in terms of elastic constants of the solid and fluid phases. Biot [1956a,b] was the first to introduce these relations into the conservation of linear momentum and solid and fluid mass balance equations. Thus he mathematically described the process of wave propagation in porous media. The solutions to his equations give the velocity of the waves traveling through the media. This is useful in some applications such as seismology, but not particularly for remediation. The important consideration for remediation is how acoustic waves affect fluid dynamics on the pore scale and how they affect

transport and dissolution.

2.1.2 Effects of Acoustics on Pore Fluid

Acoustics have a profound affect on the hydrodynamic processes within individual pores. One of the distinct features of oscillatory forcing is that it is possible to reach significant pore-scale Reynolds numbers in porous media where such Reynolds numbers would be impossible to achieve in a steady pressure-driven flow [Graham and Higdon, 2002]. At these high Reynolds numbers a number of non-linear flow regimes may exist. Graham and Higdon [2002] identified three nonlinear phenomena that may lead to enhanced transport in the presence of oscillatory driving forces: nonlinear dependence of flow rate on driving force, existence of multiple solutions with different flow rates at the same forcing level, and anisotropy arising in certain geometries at finite Reynolds numbers. It should be noted that Graham and Higdon concluded that the final disposition of the flow depends on the influence of the unsteady inertial terms in the time-dependent Navier-Stokes equations. Lab and field tests have also shown that acoustic stimulation can increase the effective permeability of the porous medium resulting in higher flow rates for a given pressure drop [Beresnev and Johnson, 1994].

2.1.3 Effects of Acoustics on Solute Transport

Several studies have shown that acoustic waves can increase solute mobilization in saturated porous media. For example, acoustic waves were found to enhance transport of a conservative tracer in packed column experiments with the effective velocity of the solute being approximately inversely proportional to the frequency of the acoustic wave [Vogler and Chrysikopoulos, 2002]. Other experimental results have also shown that significant displacement of solute in saturated porous media results from the propagation of pulsed compression waves [Gross *et al.*, 2003]. A similar effect was demonstrated using shockwaves and other types of pressure waves with

conservative tracers. It should be noted that the governing mechanisms responsible for the enhanced transport phenomenon are still under investigation.

2.1.4 Effects of Acoustics on NAPL Ganglia

Experimental evidence also shows that acoustic waves can increase both mobilization and dissolution in multi-phase systems (i.e., oil/water, NAPL/water) [Roberts *et al.*, 2001; Chrysikopoulos and Vogler, 2004, 2006]. Thomas and Narayanan [2002] showed that mass transfer of a species is enhanced several orders of magnitude when it is present in a fluid medium that is subjected to oscillatory motion, even if there is no net total flow over a cycle of the oscillation. Fieldwork has also shown that the application of acoustic waves can increase oil production from oil-saturated rock [Beresnev and Johnson, 1994]. While the exact physical mechanisms for enhanced oil production through acoustic stimulation are unclear, there are several possible mechanisms hypothesized. Acoustic oscillations may act to force a suspended oil droplet through a narrow constriction, to reduce the flow resistance by deforming the droplet or to displace droplets attached to solid surfaces [Graham and Higdon, 2002]. Experimental evidence has shown that effluent aqueous DNAPL concentration increased with the application of acoustic pressure waves with the greatest dissolution enhancement occurring at different frequencies, depending on the experimental setup [Chrysiopoulos and Vogler, 2004, 2006; Vogler and Chrysiopoulos, 2004]. Furthermore, ganglia mobilization occurred at lower background pressure-driven flow rates with acoustic pressure added [Chrysikopoulos and Vogler, 2004].

2.1.5 Effects of Acoustics on Colloid Transport

The effects of acoustic waves on colloid transport in saturated porous media have not previously been investigated to the knowledge of the author. Because we know that the transport behavior of colloids is quite different than that of conservative tracers under the same flow conditions, it is reasonable to expect that acoustic waves applied

for remediation purposes will have different effects on colloids than on conservative tracers.

2.2 Physicochemical Characteristics of Colloids

In general, colloid transport in the subsurface is a function of hydraulic factors, geological structure, and interactions between the surfaces of colloids and porous media. These in turn are the result of the physical structure and surface chemistry of the colloids as well as the chemistry of the groundwater and the physical and chemical nature of the porous media.

2.2.1 Physical Structure of Colloids

Colloids represent a class of very fine particles that have some linear dimension between 1 and 1000 nanometers [*Stumm, 1993; Chrysikopoulos and Sim, 1996*]. The particle dimension rather than chemical composition, source, or physical state (phase), designates it a colloid [*Hiemenz and Rajagopalan, 1997*]. Colloids are ubiquitous in groundwater aquifers. Typical colloids present in groundwater include clay minerals, oxides or hydroxides of Fe and Al, colloidal silica, organic matter such as humic macromolecules, and biocolloids such as viruses and bacteria [*Kretzschmar and Sticher, 1998; Tatalovich et al., 2000; Chrysikopoulos and Abdel-Salam, 1997*]. An important result of their small size is that they tend to remain suspended in solution due to Brownian motion: the random motion of molecules. Colloidal particles will remain in suspension unless they aggregate to form larger particles that can settle due to gravity or they adhere to surfaces of larger particles [*McCarthy and Wobber, 1993*]. There are two important consequences of the size range of colloids: colloidal materials have enormous surface areas and surface energies, and the properties of colloidal particles are not always those of the corresponding bulk matter or those of the corresponding atoms or molecules [*Hiemenz and Rajagopalan, 1997*]. The

result is that in addition to physical structure, surface chemistry becomes extremely important in colloid interactions.

2.2.2 Surface Chemistry

The increasing importance of the surface area as the linear dimensions of particles decrease can be understood by considering a quantity known as the specific surface area, A_{sp} , of a substance. This quantity is determined as the ratio of the area divided by the mass of an array of particles as

$$A_{sp} = \frac{A_{tot}}{m_{tot}} \quad (2.1)$$

For spherical particles equation (2.1) becomes

$$A_{sp} = \frac{3}{\rho R_s} \quad (2.2)$$

where ρ is the density of the particle and R_s is the particle radius. From the equation (2.2) it can be seen that as the particle radius, and hence the size of the particle decrease, a larger number of atoms in the particle become surface atoms. The result is that relatively weak forces such as van der Waals forces, electric double layer forces, and electrostatic forces become important and influence the transport and deposition of colloids and their ability to mobilize other contaminants.

2.3 Transport and Deposition of Colloids

The mobilization, transport, deposition, and release of colloidal particles in natural subsurface porous media have received a great deal of attention in the past decade. Their understanding is important for many subsurface applications: to assess contamination potential and protect drinking water supplies from mobile pathogenic microorganisms or radionuclides, to develop engineered bioaugmentation and bioremediation strategies, and to quantitatively predict colloid-facilitated transport of

many organic and inorganic contaminants [*Bradford et al.*, 2003; *Camesano et al.*, 1999; *Sirivithayapakorn and Keller*, 2003].

The transport of colloids through porous media strongly depends on the kinetics of colloid deposition and release [*Kretzschmar and Sticher*, 1998]. A good synopsis of the development of transport and deposition models for colloids has been provided by Loveland et al. [2003]: “Initially, colloid transport models portrayed the attachment of colloids (and “biocolloids”) to porous media as equilibrium sorption. Later, colloid filtration (irreversible first-order attachment) was introduced in conjunction with equilibrium sorption in two-site models. In most cases, colloid transport in homogeneous porous media was adequately characterized by first order attachment and release.” For example, Sim and Chrysikopoulos [1995] presented models of biocolloid (virus) transport with first order attachment, release, and inactivation for the case of linear reversible sorption equilibrium and nonequilibrium adsorption. Loveland goes on to say that further advances have focused on the dynamics of particle deposition (blocking and ripening), the geochemical heterogeneity of aquifer grain surfaces, and the physical heterogeneity of the porous medium.

Deposition of colloids in the subsurface involves several interrelated processes such as aggregation, straining or collision filtration, and settling. As has been discussed, the factors affecting these processes are physical structure of colloids such as colloid density, size, and shape; and surface chemistry, especially specific area. Other important processes that affect colloid transport and deposition in groundwater are solution chemistry, especially pH and ionic strength; and properties of the porous media such as size exclusion effects that lead to increased interstitial velocity, and surface charges [*Kretzschmar and Sticher*, 1998; *McCarthy and Zachara*, 1989; *OMelia et al.*, 1997; *Sirivithayapakorn and Keller*, 2003].

2.3.1 Solution Chemistry

Solution chemistry is important in colloid mobilization because of its ability to affect the weak surface interactions that have been previously mentioned: van der Waals forces, electric double layer forces, and electrostatic forces. For example, increasing the charge development by pH manipulation of the solution can promote detachment and mobilization of colloids. Likewise, colloids such as clays may be immobilized through van der Waals attractions that exceed electrostatic repulsions, reduced by narrow, diffuse double layers. McCarthy and Wobber [1993] reported that if subsurface ionic strength were lowered with the concomitant expansion of double-layer thicknesses around the clays, these aluminosilicate colloids could be dispersed into the flowing groundwater.

2.3.2 Physicochemical Properties of Porous Media

One of the most interesting properties of colloids in subsurface systems is that mobile colloids can be transported through natural porous media at a greater velocity than conservative solute tracers. Abundant experimental evidence shows that in column experiments, colloids can have a faster breakthrough compared to solute tracers (e.g. [Champ and Schroeter, 1988; Enfield et al., 1989; Kretzschmar and Sticher, 1998; Niehren and Kenzelbach, 1998]). It is also widely accepted that colloids arrive earlier in the effluent than a nonsorbing conservative tracer in well-characterized natural fractures [Reimus et al., 1995]. This is a direct result of the physicochemical properties of both the colloids and the porous media.

There are a number of ways this early breakthrough effect is explained in the literature. Grindrod et al. [1996] explained that in natural porous media there exist zones of low-permeability. Colloids are either physically excluded from low-permeability zones or are entrapped there physically or chemically. In general, these low-permeability zones are saturated and may still allow solute tracers into them. Others have explained this as a size exclusion chromatographic effect where colloids

are physically excluded from small pore spaces where conservative tracers can diffuse [Kretzschmar and Sticher, 1998; Kretzschmar et al., 1995; Enfield et al., 1989; Higgo et al., 1993]. These pore spaces are either smaller than the colloids or, if larger, have a constriction in their opening (throat) that is smaller than the colloid so that they are physically excluded. Another way this has been stated is that if colloids are large enough, they do not experience matrix diffusion (diffusion into tiny pores in the actual media) simply because they are larger than the pores [Reimus et al., 1995]. Still others have shown that because of their large size and low diffusivity they tend to be excluded from regions of low groundwater velocity [McCarthy and Zachara, 1989; Smith and Degueldre, 1993]. Assuming a no slip boundary condition or zero velocity at all interfaces between water and porous media, this means that colloids can not diffuse into the regions of lowest velocity streamlines. Whatever the physical mechanism, the result is that colloids follow preferential flow paths and may break through before conservative tracers. Whether or not colloids actually experience enhanced mobility depends on the nature of the colloid-matrix interactions (surface chemistry), with unfavorable deposition interactions resulting in enhanced mobility [Reimus et al., 1995], and on the size of the pore spaces in the porous media.

2.4 Colloid-Facilitated Contaminant Transport

In 1988, the U.S. Department of Energy's Subsurface Science Program established a research program that emphasized research on the critical role of colloidal-size particles and biocolloids in facilitating contaminant transport and in remediation. Since then a great deal of research has been done in this area.

There is substantial evidence from both laboratory and field experiments that colloids are efficient sorbents for contaminants such as heavy metals, nonpolar organic compounds, and radionuclides. Transport in groundwater of some contaminants, such as radionuclides, can be facilitated in the presence of colloidal particles (e.g., [Mill et al., 1991; Corapcioglu and Jiang, 1993; McCarthy, 1998]). This is a direct

result of colloid surface chemistry, as was previously discussed, because colloids have a large number of reactive surface functional groups per unit mass (i.e., a high specific area, Asp) [Kretzschmar and Sticher, 1998; Chrysikopoulos and Abdel-Salam, 1997]. Tatalovich et al. [2000] showed that applying humic substances to groundwater contaminated with a DNAPL pool enhanced the mass transfer of DNAPL to the aqueous phase.

These phenomena become important in groundwater aquifers for contaminant transport and remediation considerations. From the negative viewpoint, some colloids such as bacteria, viruses, and radionuclides, are contaminants themselves, while others such as clay particles and humic substances can increase contamination by acting as mobile sorption sites for other contaminants. Thus these colloids can cause additional contaminant migration. However, because colloids have the ability to increase mass transport of some types of contaminants, this phenomenon can be exploited to enhance remediation techniques. The key from a remediation standpoint is to enhance colloid mass transport in the contaminated porous media while utilizing conventional pump-and-treat methods. Consequently this has potential to reduce the required pump-and-treat aquifer remediation time.

Chapter 3

ACOUSTICALLY ENHANCED COLLOID TRANSPORT

3.1 Chapter Abstract

The effects of acoustic wave propagation in the direction of flow on the transport and deposition of colloids in saturated porous media were investigated by injecting a multicomponent tracer pulse into a glass-bead-packed column with a background flow and an acoustic source connected on the influent end. The multicomponent tracer consisted of Uranine (conservative tracer) as well as blue and red polystyrene microspheres (colloids of different diameters; 0.10 and 0.028 μm , respectively). Acoustic pressure at the influent was maintained at 23.0 kPa. Experiments were conducted at acoustic frequencies of 30, 50, 70, 90, 110, 130, and 150 Hz. An analytical mathematical model was developed to fit the effective parameters associated with the concentration curves. The fitted hydrodynamic dispersion for the case of no acoustic pressure (base case) for Uranine (molecular solute), and blue and red polystyrene microspheres was 5.35, 7.07, and 7.12 cm^2/h , respectively. The fitted values of the forward and reverse rate constants, r_1 and r_2 , were $5.38 \times 10^{-2} \text{ h}^{-1}$ and 2.49 h^{-1} for blue microspheres, and $5.31 \times 10^{-2} \text{ h}^{-1}$ and 2.51 h^{-1} for red microspheres. Acoustic

pressure forcing caused an increase in effective interstitial velocity at all frequencies for the conservative tracer and colloids of both sizes, with a maximum increase at 30 Hz. Furthermore, acoustic waves enhanced the dispersion process at all experimental frequencies, with a maximum at 30 Hz. For the range of experimental frequencies, applied acoustic pressure increases the rate of colloid transport and dispersion in saturated porous media.

3.2 Mathematical Model Development

An analytical mathematical model was developed to fit the effective parameters of the concentration curves. The solution is utilized for the experiments in Chapters 3, 4, and 5. The following is a detailed presentation of the steps employed. Readers uninterested in the rigorous mathematical development should skip this section.

The one-dimensional advection-dispersion equation for colloidal particles in homogeneous saturated porous media with adsorption (or filtration) and inactivation was derived from mass balance equations of a control volume under a constant hydraulic gradient and is given by the following linear second-order partial differential equation:

$$\frac{\partial C(t, x)}{\partial t} + \frac{\rho}{\theta} \frac{\partial C^*(t, x)}{\partial t} = D_e \frac{\partial^2 C(t, x)}{\partial x^2} - U_e \frac{\partial C(t, x)}{\partial x} - \lambda C(t, x) - \lambda^* \frac{\rho}{\theta} C^*(t, x), \quad (3.1)$$

where C is the concentration of colloids in suspension [M/L³], C^* is the mass of colloids adsorbed on the solid matrix [M/M], D_e is the effective hydrodynamic dispersion coefficient [L²/t], U_e is the effective interstitial fluid velocity [L/t], ρ is the bulk density of the porous media [M/L³], λ is the inactivation constant of suspended colloids [t⁻¹], λ^* is the inactivation constant of adsorbed colloids [t⁻¹], θ is the porosity of soil medium [-], and t is time [t]. The effective interstitial fluid velocity is defined as

$$U_e = U + U^*, \quad (3.2)$$

where U is the steady-state background interstitial fluid velocity [L/t], and U^* is the additional velocity component attributed to acoustic pressure [L/t]. Similarly, the

effective dispersion coefficient is defined as

$$D_e = D + D^* = (U + U^*)\alpha_L + \mathcal{D}_e = U_e\alpha_L + \mathcal{D}_e, \quad (3.3)$$

where $D = U\alpha_L + \mathcal{D}_e$ is the hydrodynamic dispersion coefficient [L^2/t], α_L is the longitudinal dispersivity [L], $\mathcal{D}_e = \mathcal{D}/\tau^*$ is the effective molecular diffusion coefficient [L^2/t] (where \mathcal{D} is the molecular diffusion coefficient [L^2/t], and $\tau^* > 1$ is the tortuosity coefficient [-]), and D^* is the additional dispersion component attributed to acoustic pressure [L^2/t]. It should be noted that the concept of effective parameters has been applied in numerous groundwater flow and solute transport studies [Valocchi, 1989; Chrysikopoulos et al., 1990, 1992; Kabala and Sposito, 1991; Chrysikopoulos, 1995; Vogler and Chrysikopoulos, 2002]. The rate of colloid attachment onto the solid matrix is described by the following first-order equation:

$$\frac{\rho}{\theta} \frac{\partial C^*(t, x)}{\partial t} = r_1 C(t, x) - r_2 C^*(t, x), \quad (3.4)$$

where r_1 is the forward rate coefficient [t^{-1}], and r_2 is the reverse rate coefficient [$M/L^3/t$]. It should be noted that (3.4) is a generalized expression which can be easily adapted to two different colloid attachment processes: nonequilibrium reversible adsorption and modified colloid filtration, [Sim and Chrysikopoulos, 1995].

The desired expression for C^* is obtained by solving (3.4) subject to an initial condition of zero sorbed (or filtered) colloid concentration ($C^*(0, x) = 0$) as

$$C^*(t, x) = \frac{r_1 \theta}{\rho} \int_0^t C(\tau, x) \exp \left[-\frac{r_2 \theta}{\rho} (t - \tau) \right] d\tau. \quad (3.5)$$

In view of (3.2)–(3.5) the governing equation (3.1) can be written as

$$\begin{aligned} \frac{\partial C(t, x)}{\partial t} = & D_e \frac{\partial^2 C(t, x)}{\partial x^2} - U_e \frac{\partial C(t, x)}{\partial x} - \mathcal{A} C(t, x) \\ & - \mathcal{B} \int_0^t C(\tau, x) \exp [-\mathcal{H}(t - \tau)] d\tau, \end{aligned} \quad (3.6)$$

where the following substitutions have been employed:

$$\mathcal{A} = r_1 + \lambda, \quad (3.7)$$

$$\mathcal{B} = r_1(\lambda^* - \mathcal{H}), \quad (3.8)$$

$$\mathcal{H} = \theta r_2 / \rho. \quad (3.9)$$

For a semi-infinite one-dimensional porous medium, the appropriate initial and boundary conditions are given by

$$C(0, x) = 0, \quad (3.10)$$

$$-D_e \frac{\partial C(t, 0)}{\partial x} + U_e C(t, 0) = M_0 \delta(t), \quad (3.11)$$

$$\frac{\partial C(t, \infty)}{\partial x} = 0, \quad (3.12)$$

where $M_0 = M_{inj}/A\theta$ is the mass injected over the cross-sectional area of the column (where M_{inj} is the injected mass [M], A is the cross sectional area of the porous medium [L²], and θ is porosity [-]), and δ is the Dirac delta function [1/t]. Initial condition (3.10) establishes a zero background colloid concentration. Boundary condition (3.11) describes the flux influent pulse concentration. The downstream boundary condition (3.12) preserves concentration continuity for a semi-infinite system. The solution to the governing equation (3.6) subject to conditions (3.10)–(3.12) is obtained analytically following the methods of Lapidus and Amundson, [1952], Chrysikopoulos et al., [1990], and Sim and Chrysikopoulos, [1995]. Taking Laplace transforms of (3.6) and (3.10)–(3.12) with respect to time and space yields

$$\begin{aligned} s\dot{\check{C}}(s, \gamma) - \dot{C}(0, \gamma) &= D_e \left[\gamma^2 \dot{\check{C}}(s, \gamma) - \gamma \tilde{C}(s, 0) - \frac{d\tilde{C}(s, 0)}{dx} \right] \\ &\quad - U_e [\gamma \dot{\check{C}}(s, \gamma) - \tilde{C}(s, 0)] - \mathcal{A} \dot{\check{C}}(s, \gamma) \\ &\quad - \frac{\mathcal{B}}{s + \mathcal{H}} \dot{\check{C}}(s, \gamma), \end{aligned} \quad (3.13)$$

$$\dot{C}(0, \gamma) = 0, \quad (3.14)$$

$$-D_e \frac{d\tilde{C}(s, 0)}{dx} + U_e \tilde{C}(s, 0) = M_0, \quad (3.15)$$

$$\frac{d\tilde{C}(s, \infty)}{dx} = 0, \quad (3.16)$$

where the following properties of Laplace transform were employed [Roberts and Kaufman, 1966]

$$\dot{\check{C}}(s, \gamma) = \int_0^\infty \int_0^\infty C(t, x) e^{-st} e^{-\gamma x} dx dt, \quad (3.17)$$

$$\mathcal{L}\{C_{t^2}(t)\} = s^2\tilde{C}(s) - sC(0) - C_t(0), \quad (3.18)$$

$$\mathcal{L}\left\{\int_0^t C(\tau)d\tau\right\} = \frac{C(s)}{s}, \quad (3.19)$$

$$\mathcal{L}\{e^{bt}\} = \frac{1}{s-b}. \quad (3.20)$$

The “tilde” and solid “dot” signify Laplace transform with respect to time and space, respectively, and s and γ are the corresponding Laplace domain variables. Substituting boundary conditions (3.14) and (3.15) into (3.13) and solving for $\dot{\tilde{C}}(s, \gamma)$ yields

$$\dot{\tilde{C}}(s, \gamma) = \frac{\gamma\tilde{C}(s, 0) - \frac{M_0}{D_e}}{\left(\gamma - \frac{U_e}{2D_e}\right)^2 - \left(\frac{s}{D_e} + \frac{\mathcal{A}}{D_e} + \frac{U_e^2}{4D_e^2} + \frac{\mathcal{B}}{D_e(s + \mathcal{H})}\right)}. \quad (3.21)$$

For mathematical convenience let

$$\begin{cases} M = -\frac{U_e}{2D_e} & (< 0), \\ N = \left(\frac{s}{D_e} + \frac{\mathcal{A}}{D_e} + \frac{U_e^2}{4D_e^2} + \frac{\mathcal{B}}{D_e(s + \mathcal{H})}\right)^{1/2} & (> 0). \end{cases} \quad (3.22)$$

Substituting (3.22) into (3.21) yields

$$\begin{aligned} \dot{\tilde{C}}(s, \gamma) &= \frac{\gamma\tilde{C}(s, 0) - \frac{M_0}{D_e}}{(\gamma + M)^2 - N^2} \\ &= \frac{\gamma\tilde{C}(s, 0)}{(\gamma + M + N)(\gamma + M - N)} - \frac{\frac{M_0}{D_e}}{(\gamma + M + N)(\gamma + M - N)}. \end{aligned} \quad (3.23)$$

The above equation is easily inverted from the Laplace space variable γ back to the space variable x . The first term on the right hand side of (3.23) is inverted as follows

$$\mathcal{L}^{-1}\left\{\frac{\gamma}{(\gamma + M + N)(\gamma + M - N)}\right\} = \frac{(M + N)e^{-(M+N)x} - (M - N)e^{-(M-N)x}}{2N}, \quad (3.24)$$

similarly, the Laplace inversion of the second term at the right hand side of (3.23) is given by

$$\mathcal{L}^{-1}\left\{\frac{1}{(\gamma + M + N)(\gamma + M - N)}\right\} = \frac{e^{-(M-N)x} - e^{-(M+N)x}}{2N}, \quad (3.25)$$

where the following Laplace inversion identities were utilized [Roberts and Kaufman, 1966]

$$\mathcal{L}^{-1}\left\{\frac{\gamma}{(\gamma + \alpha_1)(\gamma + \alpha_2)}\right\} = \frac{\alpha_1 e^{-\alpha_1 x}}{\alpha_1 - \alpha_2} + \frac{\alpha_2 e^{-\alpha_2 x}}{\alpha_2 - \alpha_1}, \quad (3.26)$$

$$\mathcal{L}^{-1}\left\{\frac{1}{(\gamma + \alpha_1)(\gamma + \alpha_2)}\right\} = \frac{e^{-\alpha_1 x} - e^{-\alpha_2 x}}{\alpha_2 - \alpha_1}. \quad (3.27)$$

Applying (3.24) and (3.25) into (3.23) yields

$$\begin{aligned} \tilde{C}(s, x) &= \tilde{C}(s, 0) \left[\frac{(M + N)e^{-(M+N)x} - (M - N)e^{-(M-N)x}}{2N} \right] \\ &\quad - \frac{M_0}{D_e} \left[\frac{e^{-(M-N)x} - e^{-(M+N)x}}{2N} \right]. \end{aligned} \quad (3.28)$$

Evaluation of $\tilde{C}(s, 0)$ can be easily done by taking the derivative with respect to x of (3.28) and, recalling boundary condition (3.16), setting the result equal to zero:

$$\begin{aligned} \frac{d\tilde{C}(s, x)}{dx} &= \tilde{C}(s, 0) \left[\frac{-(M + N)^2 e^{-(M+N)x} + (M - N)^2 e^{-(M-N)x}}{2N} \right] \\ &\quad - \frac{M_0}{D_e} \left[\frac{-(M - N)e^{-(M-N)x} + (M + N)e^{-(M+N)x}}{2N} \right] \\ &= 0. \end{aligned} \quad (3.29)$$

Rearranging (3.29), taking the limit as $x \rightarrow \infty$, and recalling from (3.22) that $M < 0$ and $N > 0$ yields

$$\tilde{C}(s, 0) = -\frac{M_0}{D_e} \frac{1}{M - N}. \quad (3.30)$$

Substituting (3.30) into (3.28) and arranging the resulting equation yields

$$\tilde{C}(s, x) = -\frac{M_0 e^{-(M+N)x}}{D_e (M - N)}. \quad (3.31)$$

Resubstituting M and N as they were defined in (3.22) into (3.31) yields

$$\tilde{C}(s, x) = \frac{M_0}{\sqrt{D_e}} \exp\left[\frac{U_e x}{2D_e}\right] \frac{\exp\left[-\frac{x}{\sqrt{D_e}}\left(s + \mathcal{A} + \frac{U_e^2}{4D_e} + \frac{\mathcal{B}}{s + \mathcal{H}}\right)^{1/2}\right]}{\left[\frac{U_e}{2\sqrt{D_e}} + \left(s + \mathcal{A} + \frac{U_e^2}{4D_e} + \frac{\mathcal{B}}{s + \mathcal{H}}\right)^{1/2}\right]}. \quad (3.32)$$

For simplicity, (3.32) is rewritten as

$$\tilde{C}(s, x) = \frac{M_0}{\sqrt{D_e}} \exp\left[\frac{U_e x}{2D_e}\right] \Theta, \quad (3.33)$$

where the following substitution is employed

$$\Theta = \frac{\exp\left[-\frac{x}{\sqrt{D_e}}\left(s + \mathcal{A} + \frac{U_e^2}{4D_e} + \frac{\mathcal{B}}{s + \mathcal{H}}\right)^{1/2}\right]}{\left[\frac{U_e}{2\sqrt{D_e}} + \left(s + \mathcal{A} + \frac{U_e^2}{4D_e} + \frac{\mathcal{B}}{s + \mathcal{H}}\right)^{1/2}\right]}. \quad (3.34)$$

For reasons that will become clear, equation (3.33) is rewritten equivalently as

$$\tilde{C}(s, x) = \frac{M_0}{\sqrt{D_e}} \exp\left[\frac{U_e x}{2D_e}\right] \left\{ \mathcal{H} \frac{1}{s + \mathcal{H}} \Theta + \frac{s}{s + \mathcal{H}} \Theta \right\}. \quad (3.35)$$

The inverse Laplace transform of (3.35) can be found by using a similar technique to that of Lapidus and Amundson, 1952, given by

$$\mathcal{L}^{-1} \left\{ \frac{1}{s + \mathcal{H}} \tilde{f} \left(s + \mathcal{H} + \frac{a}{s + \mathcal{H}} \right) \right\} = e^{-\mathcal{H}t} \int_0^t J_0 \left[2\sqrt{a\zeta(t - \zeta)} \right] f(\zeta) d\zeta, \quad (3.36)$$

where the arbitrary function $f(t)$ is the inverse Laplace transform of $\tilde{f}(s)$, and J_0 is the Bessel function of zero order. It should be noted that the same technique has been employed to find inverse Laplace transforms of several different problems [Chrysikopoulos *et al.*, 1990] and [Sim and Chrysikopoulos, 1995].

First, consider the inverse Laplace transform of the first term containing the Laplace variable s in the right hand side of (3.35)

$$\frac{1}{s + \mathcal{H}} \Theta. \quad (3.37)$$

Note that the \mathcal{H} in said term is ignored for now since the inverse Laplace transform of \mathcal{H} is simply \mathcal{H} . In order to apply (3.36), we assume that

$$\frac{1}{s + \mathcal{H}} \Theta = \frac{1}{s + \mathcal{H}} \tilde{f} \left(s + \mathcal{H} + \frac{a}{s + \mathcal{H}} \right), \quad (3.38)$$

or in other words, Θ has the form of

$$\tilde{f} \left(s + \mathcal{H} + \frac{a}{s + \mathcal{H}} \right).$$

In view of (3.36) and (3.38) then, the inverse Laplace transform of (3.37) is

$$\mathcal{L}^{-1} \left\{ \frac{1}{s + \mathcal{H}} \Theta \right\} = e^{-\mathcal{H}t} \int_0^t J_0 \left[2\sqrt{a\zeta(t - \zeta)} \right] f(\zeta) d\zeta. \quad (3.39)$$

We must determine $f(\zeta)$, which is the inverse Laplace transform of Θ , in order to complete the inverse Laplace transform of (3.37). In view of (3.34), the Laplace transform of the arbitrary function $f(t)$, which is given by $\tilde{f}(s)$ is assumed to be of the form

$$\tilde{f}(s) = \frac{e^{-l\sqrt{s+d}}}{h + \sqrt{s+d}}. \quad (3.40)$$

This step is not obvious but is done because we know the inverse Laplace transform of (3.40). Thus $f(t)$ can be determined from the inverse Laplace transform of $\tilde{f}(s)$ using Laplace transform tables as [Roberts and Kaufman, 1966; Spiegel, 1990; Sim and Chrysikopoulos, 1995]

$$\begin{aligned} f(t) &= \mathcal{L}^{-1}\{\tilde{f}(s)\} \\ &= \frac{\exp\left[\frac{-l^2}{4t} - dt\right]}{\sqrt{\pi t}} - h \exp\left[lh + (h^2 - d)t\right] \operatorname{erfc}\left[\frac{l}{2\sqrt{t}} + h\sqrt{t}\right]. \end{aligned} \quad (3.41)$$

The unknown constants h , l , d , and a are determined using the assumption given in (3.38) as follows. First, the left hand side of (3.38) is rearranged as

$$\begin{aligned} \frac{1}{s + \mathcal{H}} \Theta &= \frac{1}{s + \mathcal{H}} \frac{\exp\left[-\frac{x}{\sqrt{D_e}} \left(s + \mathcal{A} + \frac{U_e^2}{4D_e} + \frac{\mathcal{B}}{s + \mathcal{H}}\right)^{1/2}\right]}{\left[\frac{U_e}{2\sqrt{D_e}} + \left(s + \mathcal{A} + \frac{U_e^2}{4D_e} + \frac{\mathcal{B}}{s + \mathcal{H}}\right)^{1/2}\right]} \\ &= \frac{1}{s + \mathcal{H}} \frac{\exp\left[-\frac{x}{\sqrt{D_e}} \left(\frac{s^2 + \left(\mathcal{H} + \mathcal{A} + \frac{U_e^2}{4D_e}\right)s + \left(\mathcal{A} + \frac{U_e^2}{4D_e}\right)\mathcal{H} + \mathcal{B}\right)^{1/2}}{s + \mathcal{H}}\right]}{\left[\frac{U_e}{2\sqrt{D_e}} + \left(\frac{s^2 + \left(\mathcal{H} + \mathcal{A} + \frac{U_e^2}{4D_e}\right)s + \left(\mathcal{A} + \frac{U_e^2}{4D_e}\right)\mathcal{H} + \mathcal{B}\right)^{1/2}\right]}. \end{aligned} \quad (3.42)$$

Second, the correct form of the Laplace transform of the arbitrary function, $\tilde{f}(s)$, is determined by substituting the variable s in (3.40) with $s + \mathcal{H} + \frac{a}{s + \mathcal{H}}$ from (3.36) as

$$\tilde{f}\left(s + \mathcal{H} + \frac{a}{s + \mathcal{H}}\right) = \frac{\exp\left[-l \left(\frac{s^2 + (2\mathcal{H} + d)s + \mathcal{H}^2 + \mathcal{H}d + a}{s + \mathcal{H}}\right)^{1/2}\right]}{h + \left(\frac{s^2 + (2\mathcal{H} + d)s + \mathcal{H}^2 + \mathcal{H}d + a}{s + \mathcal{H}}\right)^{1/2}}. \quad (3.43)$$

Finally, in view of (3.43) the right hand side of (3.38) can be written as

$$\frac{1}{s + \mathcal{H}} \tilde{f} \left(s + \mathcal{H} + \frac{a}{s + \mathcal{H}} \right) = \frac{1}{s + \mathcal{H}} \frac{\exp \left[-l \left(\frac{s^2 + (2\mathcal{H} + d)s + \mathcal{H}^2 + \mathcal{H}d + a}{s + \mathcal{H}} \right)^{1/2} \right]}{h + \left(\frac{s^2 + (2\mathcal{H} + d)s + \mathcal{H}^2 + \mathcal{H}d + a}{s + \mathcal{H}} \right)^{1/2}}. \quad (3.44)$$

By simple comparison of (3.42) and (3.44), the unknown constants are obtained as

$$h = \frac{U_e}{2\sqrt{D_e}}, \quad (3.45)$$

$$l = \frac{x}{\sqrt{D_e}}, \quad (3.46)$$

$$d = \mathcal{A} + \frac{U_e^2}{4D_e} - \mathcal{H}, \quad (3.47)$$

$$a = \mathcal{B}. \quad (3.48)$$

After substituting (3.45)-(3.48) into (3.39) and (3.41), we define the resulting function as

$$\begin{aligned} \Phi(t) = & e^{-\mathcal{H}t} \int_0^t J_0 \left[2\sqrt{\mathcal{B}\zeta} (t - \zeta) \right] \left\{ \frac{\exp \left[\frac{-x^2}{4D_e\zeta} + \left(\mathcal{H} - \mathcal{A} - \frac{U_e^2}{4D_e} \right) \zeta \right]}{\sqrt{\pi\zeta}} \right. \\ & \left. - \frac{U_e}{2\sqrt{D_e}} \exp \left[\frac{U_e x}{2D_e} + (\mathcal{H} - \mathcal{A}) \zeta \right] \operatorname{erfc} \left[\frac{x}{2\sqrt{D_e\zeta}} + \frac{U_e}{2} \sqrt{\frac{\zeta}{D_e}} \right] \right\} d\zeta \end{aligned} \quad (3.49)$$

Therefore, we obtain the inverse Laplace transform of (3.37) as

$$\mathcal{L}^{-1} \left\{ \frac{1}{s + \mathcal{H}} \Theta \right\} = \Phi(t). \quad (3.50)$$

Now we will consider the inverse Laplace transform of the second term containing the Laplace variable s in the right hand side of (3.35)

$$\frac{s}{s + \mathcal{H}} \Theta, \quad (3.51)$$

which can be found using the following property of Laplace transforms

$$\mathcal{L} \left\{ \frac{d\Phi(t)}{dt} \right\} = s\tilde{\Phi}(s) - \Phi(0), \quad (3.52)$$

where again the “tilde” signifies the Laplace transform with respect to time of Φ . From the limits of the integral in (3.49) it is clear that $\Phi(0) = 0$. Taking the Laplace transform of both sides of (3.50) yields

$$\frac{1}{s + \mathcal{H}}\Theta = \tilde{\Phi}(s). \quad (3.53)$$

substitution of (3.53) into (3.52) gives

$$\mathcal{L}\left\{\frac{d\Phi(t)}{dt}\right\} = \frac{s}{s + \mathcal{H}}\Theta. \quad (3.54)$$

Taking the inverse Laplace transform of both sides of (3.54) gives us

$$\Phi'(t) = \mathcal{L}^{-1}\left\{\frac{s}{s + \mathcal{H}}\Theta\right\}, \quad (3.55)$$

where $\Phi'(t)$ is the derivative with respect to t of $\Phi(t)$. In view of (3.50) and (3.55) the inverse Laplace transform of (3.35) is

$$\tilde{C}(t, x) = \frac{M_0}{\sqrt{D_e}} \exp\left[\frac{U_e x}{2D_e}\right] \{\mathcal{H}\Phi(t) + \Phi'(t)\}. \quad (3.56)$$

Now we must evaluate $\Phi'(t)$. For mathematical convenience we rewrite (3.49) as

$$\Phi(t) = e^{-\mathcal{H}t} \int_0^t \Omega(t, \zeta) d\zeta, \quad (3.57)$$

where

$$\Omega(t, \zeta) = J_0 \left[2\sqrt{\mathcal{B}\zeta(t - \zeta)} \right] f(\zeta), \quad (3.58)$$

and $f(\zeta)$ was previously determined (see (3.41) and its final form in (3.49)). Using the Product Rule and taking the derivative with respect to t of both sides of (3.57) yields

$$\Phi'(t) = e^{-\mathcal{H}t} \cdot \frac{d}{dt} \left[\int_0^t \Omega(t, \zeta) d\zeta \right] - \mathcal{H}e^{-\mathcal{H}t} \int_0^t \Omega(t, \zeta) d\zeta, \quad (3.59)$$

In view of (3.57) notice that the second term on the right hand side of (3.59) is just

$$-\mathcal{H}\Phi(t). \quad (3.60)$$

The derivative in the first term on the right hand side of (3.59) can be evaluated using Leibniz’s Integral Rule, which is stated as

$$\frac{d}{dc} \int_a^b f(x, c) dx = \int_a^b \frac{\partial}{\partial c} f(x, c) dx + f(b, c) \frac{db}{dc} - f(a, c) \frac{da}{dc}, \quad (3.61)$$

where a and b are functions of c [Abramowitz and Stegun, 1972]. For the case of

(3.59) we find the following are true

$$c = t, \quad (3.62)$$

$$a(t) = 0, \quad (3.63)$$

$$b(t) = t, \quad (3.64)$$

$$x = \zeta, \quad (3.65)$$

$$f = \Omega. \quad (3.66)$$

Substitution of (3.62)-(3.66) into (3.61) yields

$$\frac{d}{dt} \int_0^t \Omega(t, \zeta) d\zeta = \int_0^t \frac{\partial}{\partial t} \Omega(t, \zeta) d\zeta + \Omega(t, t) \frac{dt}{dt} - \Omega(0, t) \frac{d0}{dt}. \quad (3.67)$$

Because

$$\frac{dt}{dt} = 1, \quad (3.68)$$

$$\frac{d0}{dt} = 0, \quad (3.69)$$

(3.67) becomes

$$\frac{d}{dt} \int_0^t \Omega(t, \zeta) d\zeta = \int_0^t \frac{\partial}{\partial t} \Omega(t, \zeta) d\zeta + \Omega(t, t). \quad (3.70)$$

In view of (3.58), the second term on the right hand side of (3.70) is

$$\begin{aligned} \Omega(t, t) &= J_0(0) \cdot f(t) \\ &= f(t). \end{aligned} \quad (3.71)$$

Now the partial derivative in the first term on the right side of (3.70) can be evaluated as follows. In view of (3.58)

$$\begin{aligned} \frac{\partial}{\partial t} \Omega(t, \zeta) &= \frac{\partial}{\partial t} \left\{ J_0 \left[2\sqrt{\mathcal{B}\zeta(t-\zeta)} \right] f(\zeta) \right\} \\ &= f(\zeta) \cdot \frac{\partial}{\partial t} \left\{ J_0 \left[2\sqrt{\mathcal{B}\zeta(t-\zeta)} \right] \right\}. \end{aligned} \quad (3.72)$$

Application of the chain rule to the right hand side of (3.72) yields

$$f(\zeta) \cdot \frac{\partial}{\partial t} \left\{ J_0 \left[2\sqrt{\mathcal{B}\zeta(t-\zeta)} \right] \right\} = f(\zeta) \cdot J_0' \left[2\sqrt{\mathcal{B}\zeta(t-\zeta)} \right] \frac{\mathcal{B}\zeta}{\sqrt{\mathcal{B}\zeta(t-\zeta)}}. \quad (3.73)$$

From recurrence relations we have that

$$J_0'(u) = -J_1(u), \quad (3.74)$$

where $J_1(u)$ is the first order Bessel function. Substitution of (3.74) into (3.73) gives us

$$-f(\zeta) \cdot J_1 \left[2\sqrt{\mathcal{B}\zeta(t-\zeta)} \right] \frac{\mathcal{B}\zeta}{\sqrt{\mathcal{B}\zeta(t-\zeta)}}, \quad (3.75)$$

and rearranging (3.75) we have obtained

$$\frac{\partial}{\partial t} \Omega(t, \zeta) = -f(\zeta) \cdot J_1 \left[2\sqrt{\mathcal{B}\zeta(t-\zeta)} \right] \frac{\mathcal{B}\zeta}{\sqrt{\mathcal{B}\zeta(t-\zeta)}}. \quad (3.76)$$

Substituting (3.76) and (3.71) into (3.70) gives us

$$\frac{d}{dt} \int_0^t \Omega(t, \zeta) d\zeta = - \int_0^t \frac{\mathcal{B}\zeta}{\sqrt{\mathcal{B}\zeta(t-\zeta)}} \cdot J_1 \left[2\sqrt{\mathcal{B}\zeta(t-\zeta)} \right] f(\zeta) d\zeta + f(t). \quad (3.77)$$

Substitution of (3.77) and (3.60) into (3.59) gives us

$$\Phi'(t) = -e^{-\mathcal{H}t} \int_0^t \frac{\mathcal{B}\zeta}{\sqrt{\mathcal{B}\zeta(t-\zeta)}} J_1 \left[2\sqrt{\mathcal{B}\zeta(t-\zeta)} \right] f(\zeta) d\zeta + e^{-\mathcal{H}t} f(t) - \mathcal{H}\Phi(t). \quad (3.78)$$

Substituting (3.78) into (3.56) yields

$$\begin{aligned} \tilde{C}(t, x) &= \frac{M_0}{\sqrt{D_e}} \exp \left[\frac{U_e x}{2D_e} \right] \left\{ \mathcal{H}\Phi(t) - e^{-\mathcal{H}t} \int_0^t \frac{\mathcal{B}\zeta}{\sqrt{\mathcal{B}\zeta(t-\zeta)}} J_1 \left[2\sqrt{\mathcal{B}\zeta(t-\zeta)} \right] f(\zeta) d\zeta \right. \\ &\quad \left. + e^{-\mathcal{H}t} f(t) - \mathcal{H}\Phi(t) \right\}. \end{aligned} \quad (3.79)$$

Note that the $\mathcal{H}\Phi(t)$ terms cancel. Rearranging (3.79) gives

$$\tilde{C}(t, x) = \frac{M_0}{\sqrt{D_e}} \exp \left[\frac{U_e x}{2D_e} - \mathcal{H}t \right] \left\{ f(t) - \int_0^t \frac{\mathcal{B}\zeta}{\sqrt{\mathcal{B}\zeta(t-\zeta)}} J_1 \left[2\sqrt{\mathcal{B}\zeta(t-\zeta)} \right] f(\zeta) d\zeta \right\}. \quad (3.80)$$

Finally, substitution of $f(t)$ as it was defined in (3.49) into (3.80) results in the final solution:

$$\begin{aligned}
C(t, x) = & \frac{M_0}{\sqrt{D_e}} \exp \left[\frac{U_e x}{2D_e} - \mathcal{H}t \right] \left\{ \frac{\exp \left[\frac{-x^2}{4D_e t} + \left(\mathcal{H} - \mathcal{A} - \frac{U_e^2}{4D_e} \right) t \right]}{\sqrt{\pi t}} \right. \\
& - \frac{U_e}{2\sqrt{D_e}} \exp \left[\frac{U_e x}{2D_e} + (\mathcal{H} - \mathcal{A})t \right] \operatorname{erfc} \left[\frac{x}{2\sqrt{D_e t}} + \frac{U_e}{2} \sqrt{\frac{t}{D_e}} \right] \\
& + \int_0^t \frac{\mathcal{B}\zeta}{\sqrt{\mathcal{B}\zeta(t-\zeta)}} I_1 \left[2\sqrt{\mathcal{B}\zeta(t-\zeta)} \right] \left[\frac{\exp \left[\frac{-x^2}{4D_e \zeta} + \left(\mathcal{H} - \mathcal{A} - \frac{U_e^2}{4D_e} \right) \zeta \right]}{\sqrt{\pi \zeta}} \right. \\
& \left. \left. - \frac{U_e}{2\sqrt{D_e}} \exp \left[\frac{U_e x}{2D_e} + (\mathcal{H} - \mathcal{A})\zeta \right] \operatorname{erfc} \left[\frac{x}{2\sqrt{D_e \zeta}} + \frac{U_e}{2} \sqrt{\frac{\zeta}{D_e}} \right] \right] d\zeta \right\}. \quad (3.81)
\end{aligned}$$

3.3 Experimental Design and Procedures

3.3.1 Physical Description of Apparatus

A multicomponent tracer pulse was injected into the injection port of a 30 cm long glass-bead-packed water-saturated glass laboratory column with a 2.5 cm inner diameter (Kimble Kontes, New Jersey). The injection port was fitted with a stainless steel tube and septum, which allowed the injection needle to penetrate to the center of the glass-bead pack within the column. This allows both the injection point and sampling point to be directly in line in the direction of flow. To ensure consistent injections between experiments and thereby reduce experimental error in the measured dispersion of the tracer, a special syringe injector was constructed. The syringe injector consists of a syringe holder, two steel sliders, a syringe depressor, and springs. The syringe holder keeps the syringe stationary while the depressor is pulled away from the holder stretching the springs. When released the spring force pulls the depressor along the sliders into the syringe plunger and injects the tracer solution. Figure 3.1 is two photographs of the syringe injector before and after injection. The column was packed with 2 mm diameter soda-lime glass beads (Fisher Scientific, New Jersey) as a model porous media. Glass beads were chosen as model porous media

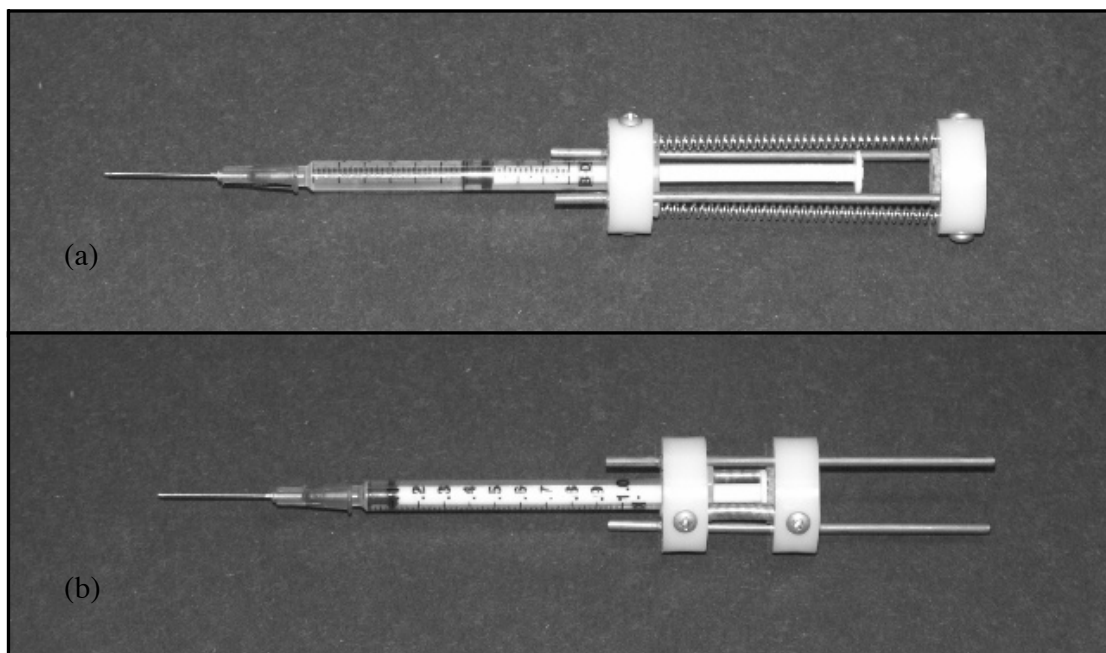


Figure 3.1: (a) A photograph of the syringe injector and syringe ready for injection with springs stretched. (b) A photograph of the syringe injector and syringe after injection with springs relaxed.

because they are uniform in size thus creating relatively uniform pore spaces, they are chemically nonreactive with the solutions used in these experiments, and they have a uniform negative surface charge [Weronski *et al.*, 2003]. The beads were retained in the column with teflon screens placed on both the influent and effluent ends of the column. The screens allow water and colloids to enter and exit the bead pack unimpeded as well as allowing acoustic wave propagation from the reservoir through the column. The teflon screens were held in place by teflon column end caps which in turn were held in place by plastic retainers that screw into threads molded in the ends of the glass column. Figure 3.2 shows how the glass-bead pack is retained in the column while allowing acoustic wave propagation. The teflon end caps were milled to accommodate 1/4 inch stainless steel fittings (Swageloc) for 3/8 inch semi-rigid plastic tubing (Fisher Scientific, Pennsylvania). Both teflon and stainless steel are chemically nonreactive with the solutions used. Constant flow of purified water at a

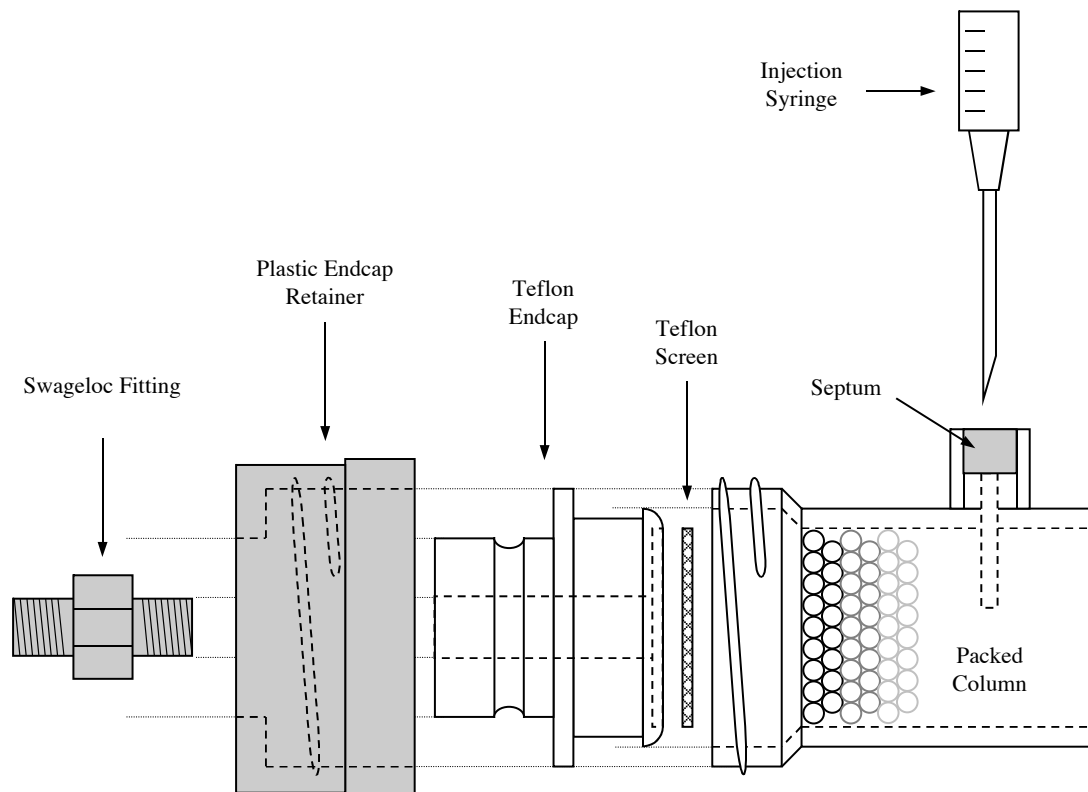


Figure 3.2: A schematic of how the glass-bead pack is retained in the column while allowing acoustic wave propagation.

rate of 0.80 mL/min was maintained through the packed column with a dual-syringe infusion pump (KDS200; KD Scientific, Massachusetts). Acoustic pressure waves were introduced into the column by the oscillation of a pressure transducer (TST37; Clark Sythesis, Colorado). The transducer was mounted securely to a laboratory countertop with a bracket specifically designed to limit vibration so that all the acoustic energy would be transferred to the column. The only physical connection of the transducer to the glass column was through a small plunger. The plunger was attached to the transducer on one end and a neoprene diaphragm on the other end. The diaphragm was secured to a specially designed reservoir milled out of plexiglass. The reservoir and the column were filled with purified water. Wave propagation through the water and porous media occurred when the diaphragm was oscillated by the transducer. The frequency of acoustic pressure oscillation was controlled by a

function generator (FG-7002C; LG Precision, California). The magnitude of acoustic pressure was controlled by an amplifier (Lab300; Lab Gruppen, Sweden) and was measured with PCB106b pressure sensors in conjunction with 480E09 ICP sensor signal conditioners (PCB Piezotronics, Inc., New York) and a digital multimeter (MXD-4660A; Metex, Korea). The pressure sensors were mounted on the influent and effluent ends of the glass-bead pack. A complete schematic of the experimental apparatus employed in this study is shown in Figure 3.3. A top-down detail of the encircled area of 3.3 is shown in Figure 3.4. This shows how the transducer,

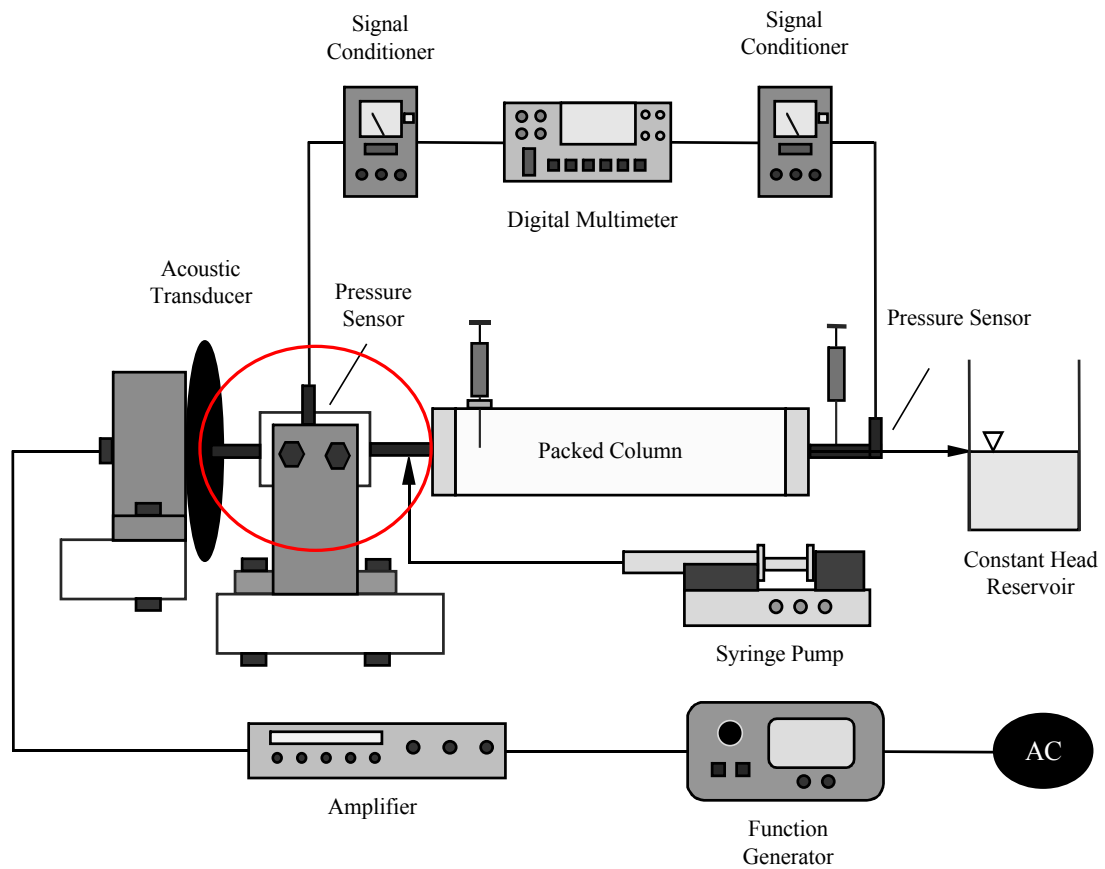


Figure 3.3: The experimental apparatus used in the acoustic experiments described.

plunger, diaphragm, and reservoir are connected for acoustic wave propagation. Effluent samples were collected at regular intervals from a dedicated needle (sampling port) mounted with its sharpened end resting against the teflon screen that retained

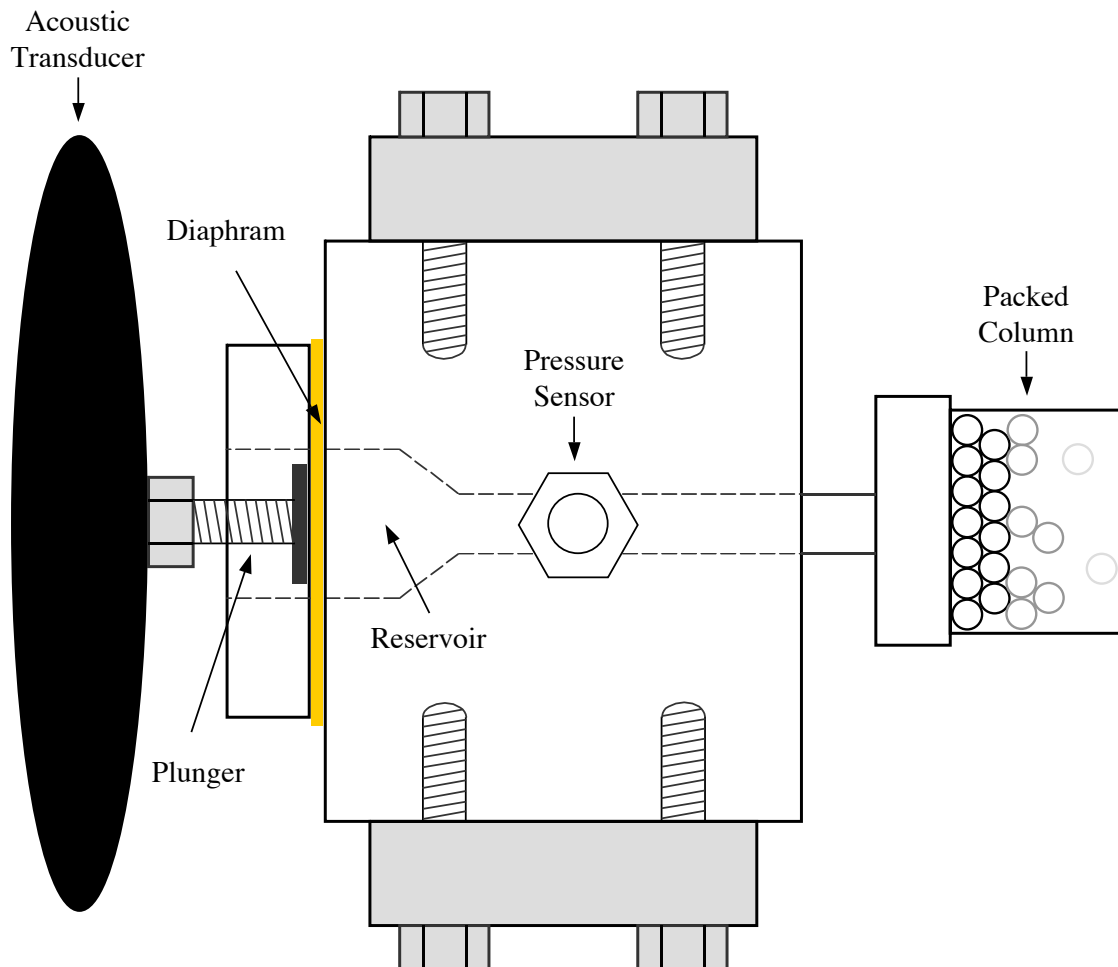


Figure 3.4: A top-down detail of the pressure transducer, plunger, diaphragm, and acoustic reservoir encircled in Figure 3.3

the glass bead pack on the effluent end of the column. Beyond the sampling port the effluent tube was bent upward and then leveled to create a constant background pressure head.

3.3.2 Experimental Procedure

Column apparatus and all accessories were carefully cleaned between experiments by pumping several pore volumes of a strong acid (HCl) followed by several pore volumes of purified degassed water, similar to the process performed by Weronki et al., 2003.

This procedure ensured that the column and media were free from contaminants and microorganisms and that solution chemistry was uniform between experiments. All water used in these experiments was purified with a Milli-Q UV plus water purification system (Millipore Corp., Massachusetts) with a filter size of $0.22 \mu\text{m}$ and UV sterilization then polished to a specific resistance of $18.2 \text{ m}\Omega\text{-cm}$. Table 3.1 shows the finished water purity parameters of the water used in these experiments. The water

Table 3.1: Water Purity Parameters

Parameter	Specification
Resistivity	$18.2 \text{ m}\Omega\text{-cm}$
Total Organic Carbon	$\leq 5 \text{ ppb}$
Particles $\geq 0.22 \mu\text{m}$	$< 1/\text{mL}$
Total dissolved solids	$< 10 \text{ ppb}$
Silicates	$< 0.1 \text{ ppb}$
Heavy metals	$\leq 0.1 \text{ ppb}$
Microorganisms	$\leq 1 \text{ cfu/mL}$

was then vacuum degassed in a clean vacuum flask for at least 15 minutes before being run through the column to remove dissolved gases and to prevent absorption of carbon dioxide (CO_2) gas. Dissolved CO_2 forms carbonic acid and can reduce the pH of the water thereby changing the transport and deposition properties of colloids. Degassing allows the pH of the water throughout these experiments to remain at pH 7.2. The effects of solution chemistry (i.e., pH) on the transport and deposition of colloids has been discussed in Section 2.3.1. After several pore volumes of purified water were pumped through the column an effluent sample was analyzed for chloride ions using an ion chromatograph (DX120; Dionex, Massachusetts) to ensure that there were no traces of HCl remaining in the column. If any HCl remained, several more pore volumes of purified water were pumped through the column and the effluent tested again until there were no traces of HCl. The multicomponent tracer

injected into the column was made prior to each experiment by combining exactly 1.0 mL of a conservative tracer stock solution, 1.0 mL of blue microsphere stock solution, and 1.0 mL of red microsphere stock solution. The conservative tracer stock solution was a 5 mg/L solution of Fluorescein Sodium Salt ($C_{20}H_{10}Na_2O_5$) commonly known as Uranine (Fisher Scientific, New Jersey). The blue and red microsphere stock solutions were one-in-twenty dilutions of commercially available one-percent-by-mass solutions of fluorescent-dyed polystyrene microspheres (Duke Scientific, California) of a specific diameter. The colors (i.e., blue and red) refer to the fluorescent properties of the microspheres and will be discussed in detail. Each color also corresponds to a specific diameter of the particles so that each stock solution contained microspheres of only one specific diameter. The flow rate of the pump was set to 0.80 mL/min and a slug of 0.6 mL of the multi-component tracer solution was instantaneously injected with the syringe injector into the column through the injection port located near the influent end of the column. Elapsed time was measured with a digital quartz chronograph (Timex, New Jersey). Five dilutions of the remaining multicomponent tracer were made in 50 mL volumetric flasks labeled C1 through C5 and a sample of each was transferred to a 1 cm pathlength disposable polyethylene cuvette (Cole Parmer Instrument Co., Illinois). Sample cuvettes were then labeled from 38 minutes to 106 minutes by two-minute increments. Sample effluent volumes of 0.5 mL were collected from the sampling port at regular two-minute intervals beginning at 38 minutes from time of injection using a dedicated disposable 1.0 mL tuberculin plastic syringe (Becton Dickinson and Co., New Jersey). The samples were then transferred to cuvettes where exactly 1.5 mL of the Millipore-purified water was added using an eppendorf reference pipette (Brinkmann Instruments, Inc., New York). This dilution was necessary because the luminescence spectrometer used to analyze the samples requires a minimum sample volume of 2 mL. The sample cuvettes were then sealed with plastic cuvette lids (Fisher Scientific, New Jersey). Ambient air temperature and thereby the temperature of water was maintained throughout the experiments at 21°C. The base case experiment was first conducted to determine background curves for Uranine (conservative tracer) and the two different-sized microsphere sus-

pensions (colloids) in the absence of acoustic waves (0Hz). Subsequent flowthrough experiments were conducted using the same procedure described for the base case, but in the presence of acoustic waves at eight different preselected acoustic frequencies. Acoustic pressure at the influent was maintained at 3.33 psi (23.0 kPa). Due to different attenuation of acoustic waves at different frequencies, the acoustic pressure at the effluent was different depending upon frequency. Generally effluent pressure remained constant throughout the experiment and was always less than the pressure at the influent.

3.3.3 Tracer Properties

Tracers are chemicals or small particles commonly used in the study of the hydrodynamic processes of many systems including rivers and estuaries, tidal zones, lakes and marshes, and groundwater aquifers. They are also used extensively in the laboratory to quantify and test theoretical analytical and numerical solutions to transport equations. Tracers may be categorized into many classes but the two most common classifications are conservative tracers, those that do not experience adsorption to the porous matrix nor decay on the timescale of the experiment or study, and nonconservative tracers, which may experience adsorption and/or decay. Therefore, when a mass of conservative tracer is injected into a packed column, the entire mass is recovered or conserved in the effluent stream. Nonconservative tracers always lose some mass either through decay or adsorption to the porous media. In the case of these experiments, the colloids are considered to experience adsorption but not decay. Each experiment was run with one conservative tracer (Uranine) and two non-conservative tracers (red and blue microspheres). Uranine is a dissolved molecular solute whereas the microspheres, due to their size, are colloids. The method of analyzing any tracer depends on the physical and chemical properties of the tracer. Ion chromatography can be used for analysis of most ionic salt tracers such as potassium bromide and other such alkali halide tracers. Spectrophotometric analysis is possible for molecular solute tracers that absorb light at certain wavelengths. Gravimetric

analysis, the physical capturing and weighing of the particles on a filter media, or particle counting, the measuring of the scattering of a laser beam passing through a sample, can be used for analysis of small particles such as colloids. Fluorescence analysis is possible for tracers that exhibit fluorescence or chemiluminescence. Fluorescence refers to the property of a chemical to emit radiation (usually visible or UV light) when excited by radiation of a lower wavelength. The physicochemical properties of the chemical must be such that electrons in lower energy orbitals can be excited to higher energy orbitals by absorbing energy when bombarded with light of a particular wavelength. These higher energy orbitals are unstable and therefore the electrons decay to their original orbitals. As their orbit decays, energy is emitted in the form of light of a higher wavelength. Chemicals that exhibit fluorescence typically have an excitation spectra (a band of wavelengths of light that will excite electrons) and an emission spectra (a band of wavelengths of light emitted by decaying electrons) each containing a maxima, or in some cases several relative maxima, which depend on the physical structure of the molecule. The advantage of using a tracer that fluoresces over other types of tracers is that very dilute concentrations can be detected. Analysis is also generally faster because the excitation and consequent emission is virtually instantaneous. Both types of tracers (i.e., molecular solute and colloids) used in these experiments were specifically selected because they exhibit fluorescence. This is advantageous because all three tracers can be detected at very low concentration and all three can be detected using the same type of fluorescence analysis equipment.

There are several reasons to use a conservative tracer in packed column experiments. Conservative tracers are commonly used in order to characterize certain parameters of the porous media or packed column (e.g., dispersion and dispersivity). In addition, the breakthrough curves of the conservative tracer give a basis of comparison to characterize the colloid breakthrough curves. Finally, the effects of acoustic wave propagation on the transport of a conservative tracer has been studied and documented [Vogler and Chrysikopoulos, 2002]. Again, because fluorescent microspheres

were used as model colloids, a conservative tracer that exhibits fluorescence was also desirable so that the same equipment could be used for analysis. However, in order to analyze samples containing three different fluorescent tracers, it was important to select a conservative tracer whose excitation and emission spectra did not interfere with those of the microspheres. After careful examination of the excitation and emission spectra of the microspheres and several different tracers, Fluorescein Sodium Salt ($C_{20}H_{10}Na_2O_5$) commonly known as Uranine (Fisher Scientific, New Jersey) was selected. Uranine has been widely used as a tracer in groundwater and surface water studies. It has a molecular weight of 376.28 g/mol, an excitation maxima at 463 nm, and a broad emission spectra.

Two suspensions of fluorescent-dyed polystyrene microspheres of different mean particle diameter were used as model colloids in these experiments. Microsphere suspensions are commercially available and are used commonly for testing of filtration media and systems, flow tracing and fluid mechanics, sedimentation and centrifugation studies, particle counter research and development, fluorescence microscopy, and medical imaging. Made of polystyrene, which itself does not fluoresce, they contain fluorescent dyes incorporated into their polymer matrix. They are packaged as suspensions of one-percent solids by mass in water. Two different-colored suspensions were used in this experiment: red and blue. The colors actually refer to the color of the wavelengths of light in the emission spectra which is dependent upon the type of fluorescent dyes incorporated into the polystyrene. Each color of microsphere suspension is available in a number of different mean diameter sizes. The red microspheres selected have a measured mean diameter of $0.028 \mu\text{m}$, an excitation maxima at 542 nm and an emission maxima at 612 nm. The blue microspheres selected have a measured mean diameter of $0.10 \mu\text{m}$, an excitation maxima at 388 nm and an emission maxima at 447 nm.

3.3.4 Method of Sample Analysis

When all the column effluent samples containing different concentrations of the three tracers were collected for an experiment as described in Section 3.3.2, they were analyzed by performing emission scans with an Aminco-Bowman series 2 luminescence spectrometer (Thermo Spectronic, New York). This section will discuss how the AB2 is used for fluorescence analysis, how emission wavelength ranges were chosen to resolve the concentration of each tracer in a sample, a confidence analysis of the measured concentrations, and the procedure used for calibrating concentrations for each experiment.

The Aminco-Bowman series 2 luminescence spectrometer (AB2) is capable of performing many different types of fluorescence and luminescence analyses including excitation scans, emission scans, synchronous scans, time traces, qualitative analyses, and polarization. Emission scans were used to determine tracer concentrations in the column effluent samples from these experiments. In an emission scan, the sample is continuously excited at one specific wavelength (usually the excitation maxima which is dependent upon the structure of the molecules and can be predetermined with an excitation scan) while a range of higher wavelengths is scanned for light emitted or fluoresced from the sample. Figure 3.5 is a schematic of the AB2 performing an emission scan. To perform an emission scan with the AB2, the sample cuvette is placed in the sample compartment and the lid is closed to shut out all ambient light. The user then selects emission scan from the applications pull-down menu as the type of analysis to be performed. In a series of dialog boxes the user inputs a number of parameters for the scan such as the excitation wavelength, excitation monochromator step size, bandpass, lower limit wavelength of the scan, upper limit wavelength of the scan, scan rate, and number of repetitions. The selection of these parameters will be discussed thoroughly. A 150 W ozone-free Xenon lamp provides a broadband excitation source in the range from 200-900 nm. The light passes through the excitation monochromator that was previously set by the user. A monochromator is a precision optical component consisting of diffraction grat-

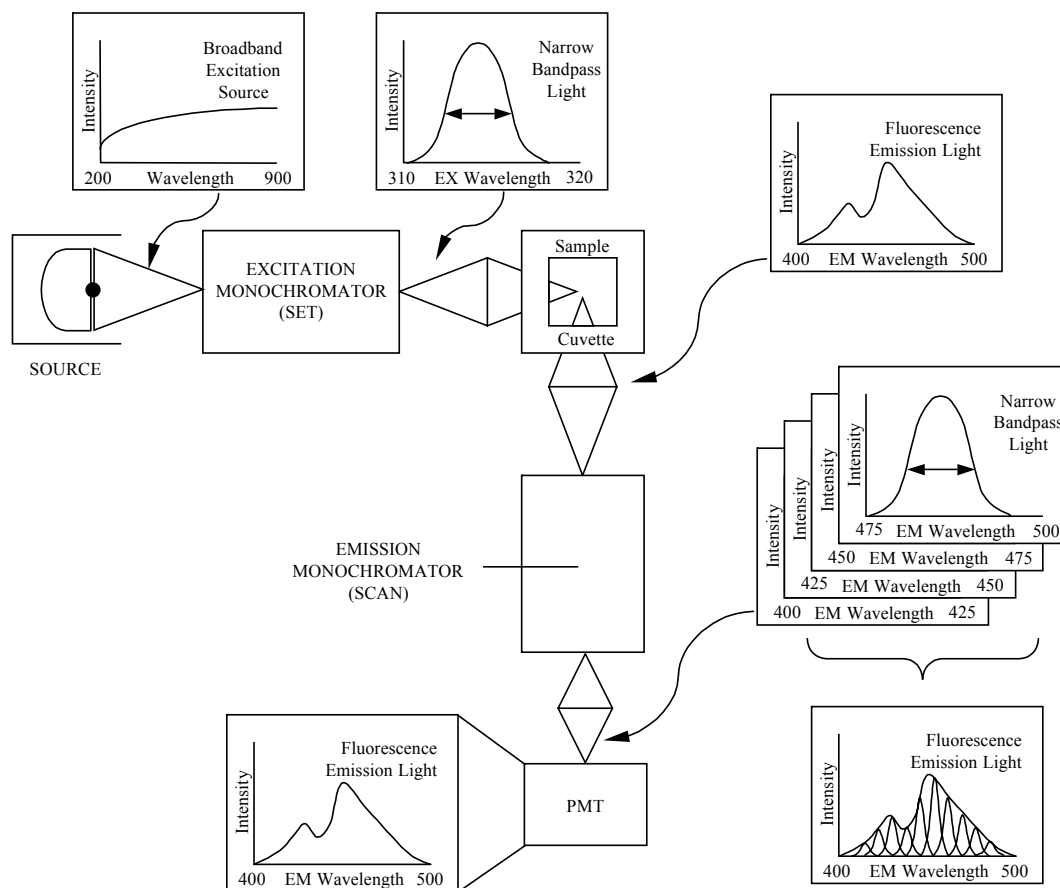


Figure 3.5: Schematic representation of the AB2 Luminescence Spectrometer performing an emission scan.

ings, mirrors, and slits used to select wavelength and bandpass values for excitation light and emitted light. The excitation monochromator selects a narrow bandwidth (group of wavelengths) from the source light. This narrow bandpass light is allowed to pass through while all other light from the source is diffracted. In the diagram, the light exiting the excitation monochromator is in the range of 310 to 320 nm. In reality, this is usually set at the excitation maxima of the sample. The excitation light is then passed through the cuvette containing the sample as a continuous beam where it excites the fluorescent molecules. The sample then emits a broad spectrum of light of higher wavelengths in all directions. This light is known as the sample's emission spectra, in this case in the range of 400 to 500 nm. Some of

this emitted light passes through the emission monochromator which is positioned at 90 degrees to the excitation beam in order to avoid any interference. The emission monochromator selects a narrow bandwidth of emission wavelengths, in this case 400 to 425 nm. Again, the emission monochromator allows light of these wavelengths to pass through while deflecting all other wavelengths. This light from the emission monochromator illuminates the photocathode of the photomultiplier tube (PMT). The PMT then converts the light to an amplified DC current which is measured by the instruments acquisition electronics. The emission monochromator is then shifted by the step size (previously set) and another acquisition obtained. This process is repeated throughout the range of the emission scan. The AB2 automates this process so that you set excitation conditions and emission range and instrument collects the data and displays it as one continuous spectrum as in the final graph at the bottom right of Figure 3.5. Three separate emission scans were performed on each effluent sample corresponding to the three settings for each of the three tracers. Each tracer's setting had an excitation maxima and emission wavelength range selected for that tracer. Thus it was possible to independently determine the concentration of Uranine, blue, and red microspheres in each sample. Before the samples could be analyzed it was necessary to carefully select excitation and emission wavelengths to minimize interference between the three tracers.

Clearly, an emission scan could be performed on any one constituent of the multicomponent tracer injection by itself, provided that the excitation wavelength maxima is known or can be determined. However, in order to determine the concentration of one tracer in a sample that contains the others, it was necessary to carefully select the emission wavelength ranges to allow for maximum fluorescence while minimizing any overlapping areas. Three emission scans with excitations at 412, 463, and 542 nm corresponding to the excitation maxima of blue microspheres, Uranine, and red microspheres respectively were performed on each of three samples. The three samples were single component samples: one of blue microspheres, one Uranine, and one red microspheres in the range of concentration they would be expected in the

effluent. By plotting the three emission spectra (blue microspheres, Uranine, and red microspheres) at each excitation wavelength, it was possible to visually inspect for overlapping areas or cross-excitation. For instance, for the 412 nm excitation the blue microspheres showed a peak excitation in the range of 434 nm to 490 nm. However, the Uranine emission spectra for the 412 nm excitation wavelength began to increase from baseline at around 465 nm. The red microspheres did not emit with this excitation wavelength. Thus the emission spectrum range selected for the blue microspheres was from 434 nm to 464 nm. In this way, a sample containing blue microspheres, Uranine, and red microspheres could be excited at 412 nm and emission spectra recorded in the range 434 nm to 464 nm, and the result would be the same as a sample containing the same concentration of blue microspheres with no Uranine nor red microspheres present. The same procedure was repeated for selection of all wavelength ranges. Table 3.2 summarizes the settings used for the emission scans. The ranges were then saved as global presets labeled in the computer as BLUE, URANINE, and RED. Thus each set of effluent samples and calibration dilutions for a given experiment was scanned under each of the three global presets and the concentration of each constituent tracer in the multicomponent tracer was determined.

Since the wavelength ranges were selected by visual inspection, it was necessary to test whether these settings were sufficient to properly resolve the concentrations of the three tracers in a single sample. To accomplish this, eleven dilutions were made with various amounts of the stock solutions to simulate effluent concentration curves where each tracer concentration was shifted by 2 minutes. We expect for the effluent concentration curves for the three tracers to either correspond to each other in each experiment (i.e., the peaks line up though the magnitudes are expected to be different) or to be shifted with respect to one another by a small amount. The most interference will occur if these shifts occur, so that if we can show the validity of measurements for shifted curves, this will also confirm the case of non-shifted curves. Figure 3.6 shows the concentration of each tracer in each of eleven dilutions

containing different amounts of each tracer. Also included on the graph are error

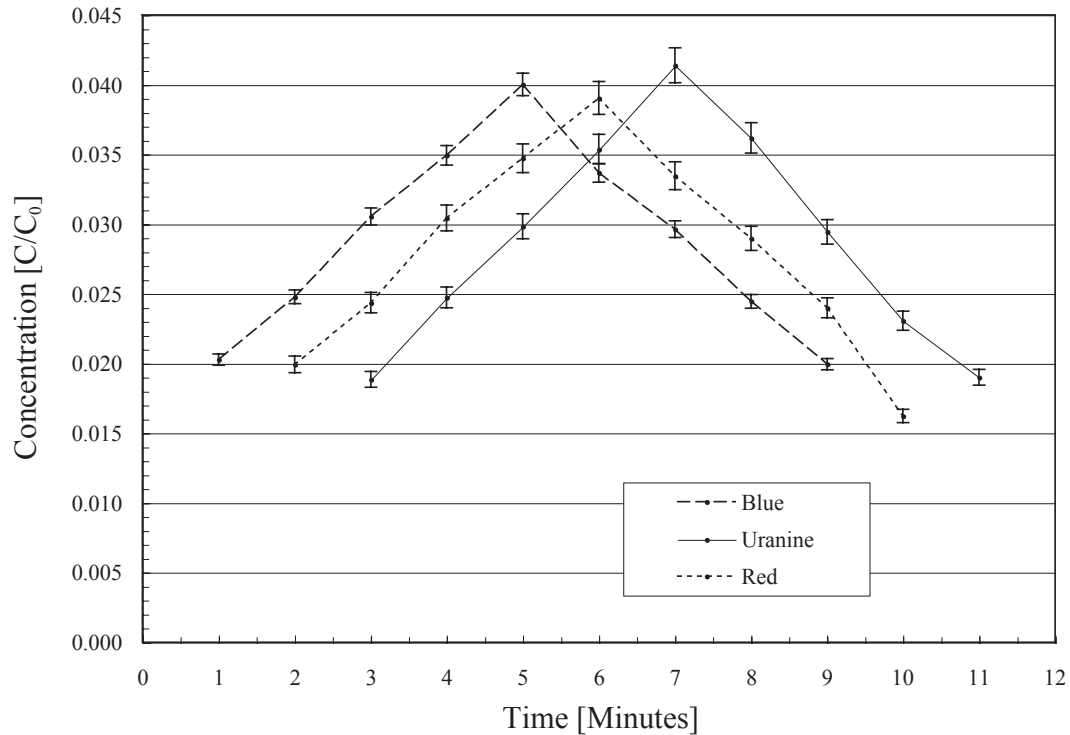


Figure 3.6: Multicomponent effluent sample concentrations made from dilutions of stock solutions to simulate a shifted curve.

bars associated with each measurement. In general any one measurement of blue microspheres or Uranine was within two percent of actual while any one measurement of red was within four percent of actual. It was found that at higher concentrations there was more interference particularly with red microspheres. Therefore it was decided to use concentrations in the range of expected effluent concentrations for calibrating each experiment.

Section 3.3.2 stated that five dilutions of the initial multicomponent tracer injection were made at beginning of each experiment. At high concentrations there is more interference between the tracers so the desire was for the dilutions to be in the range of concentrations expected in the effluent. From prior packed column experiments

it was known that the peak of the concentration curve would be approximately a one-in-twenty dilution of the actual injected concentration. Dilutions were made by pipetting 240, 300, 360, 420, and 480 μL of the multicomponent tracer injection into five 50 mL volumetric flasks and diluted to a final volume of 50 mL with purified water. The dilutions were then transferred into cuvettes, capped, and labeled C1 through C5 respectively. These were analyzed along with the samples and the values plotted with concentration on the x-axis and fluorescence on the y-axis. A linear least-squares fit calibration curve was constructed and the value of the slope was used to convert effluent sample fluorescence measurements into concentration. In order to compare concentration breakthrough curves for Uranine and blue and red microspheres on the same graph it was necessary to make the curves of the same scale. The concentrations of Uranine and red and blue microspheres used in the multicomponent tracer injection were selected due to the intensity of the light they emitted, without regard to a physical concentration. As a result, the injected multicomponent tracer solution was 1.67 mg/L Uranine and 0.067 $\mu\text{g/L}$ of both microspheres. The concentrations of microspheres reported as mass per volume are smaller by nearly five orders of magnitude than those of Uranine. This can be explained by considering that Uranine is molecular level solute and the microspheres are considerably larger particles. The microspheres have large surface areas covered with fluorescent dye and therefore emit more light and require a smaller mass concentration to measure. In addition, a mass concentration of microspheres includes both the polystyrene polymer and the fluorescent dyes incorporated into them. Therefore units of concentration such as mg/L and $\mu\text{g/L}$ are not particularly meaningful when considering colloidal particles. A dimensionless concentration was used to compare concentrations of all the tracers. The concentrations are reported as C/C_0 , where C is the measured tracer concentration in the effluent and C_0 is the concentration of the tracer injected. C/C_0 , then, is the percentage of the initial injected tracer concentration in the effluent.

3.4 Results and Discussion

3.4.1 Determination of Column Parameters

Before the analytical solution (equation 3.81) could be fit to the experimental breakthrough data, the parameters associated with the column and glass beads needed to be obtained. The relevant parameters were porosity of the column, θ , bulk density of the glass beads, ρ , and the average interstitial velocity, U . It should be noted that the variables \mathcal{H} and U_e in equation 3.81 are combined parameters that contain θ , ρ , and U . Porosity of the solid matrix (bead-pack) is given by

$$\theta = \frac{V_{voids}}{V_{total}} = \frac{V_{total} - V_{beads}}{V_{total}}, \quad (3.82)$$

where V_{voids} is the volume of the void space inside the packed column [L^3]; V_{total} is the total inner volume of the glass column [L^3]; and V_{beads} is the volume of the glass beads themselves in the column [L^3]. The total volume was calculated from the inner diameter and length of the column. The volume of the beads in the column was determined by transferring the beads to a graduated cylinder filled with water and measuring the volume of water they displaced (Archimedes' Principle). The bulk density is given by

$$\rho = \frac{M_{beads}}{V_{total}}, \quad (3.83)$$

where M_{beads} is the mass of the beads [M]; and V_{total} is the total inner volume of the glass column [L^3] as before. The average interstitial velocity is given by

$$U = \frac{q}{\theta} = \frac{Q}{A\theta}, \quad (3.84)$$

where q is the seepage or Darcy velocity [L/t]; Q is the volumetric flow rate [L^3/t]; and A is the cross-sectional area of the columns [L^2]. The volumetric flow rate was set at 0.80 mL/min (see section 3.3.1) for all experiments and the cross-sectional area was calculated from the inner diameter of the column. The parameters are listed in Table 3.3.

3.4.2 Effects of Various Model Parameters

Before analysis of the experimental data, a discussion of the effects of the various model parameters on the character of the breakthrough curves generated by the analytical solution (i.e., $C(t, x)$ at a fixed position, x) is instructive. Figures 3.7, 3.8, 3.9, and 3.10 illustrate the effects of changing a single model parameter (namely U , D , k_c , and k_r), while keeping the other model parameters constant. These figures will facilitate some qualitative insight into the causes of the observed effects in the experimental data.

Figure 3.7 illustrates the effect of changing average interstitial velocities, U , while holding the other model parameters constant. The solution was plotted with U equal

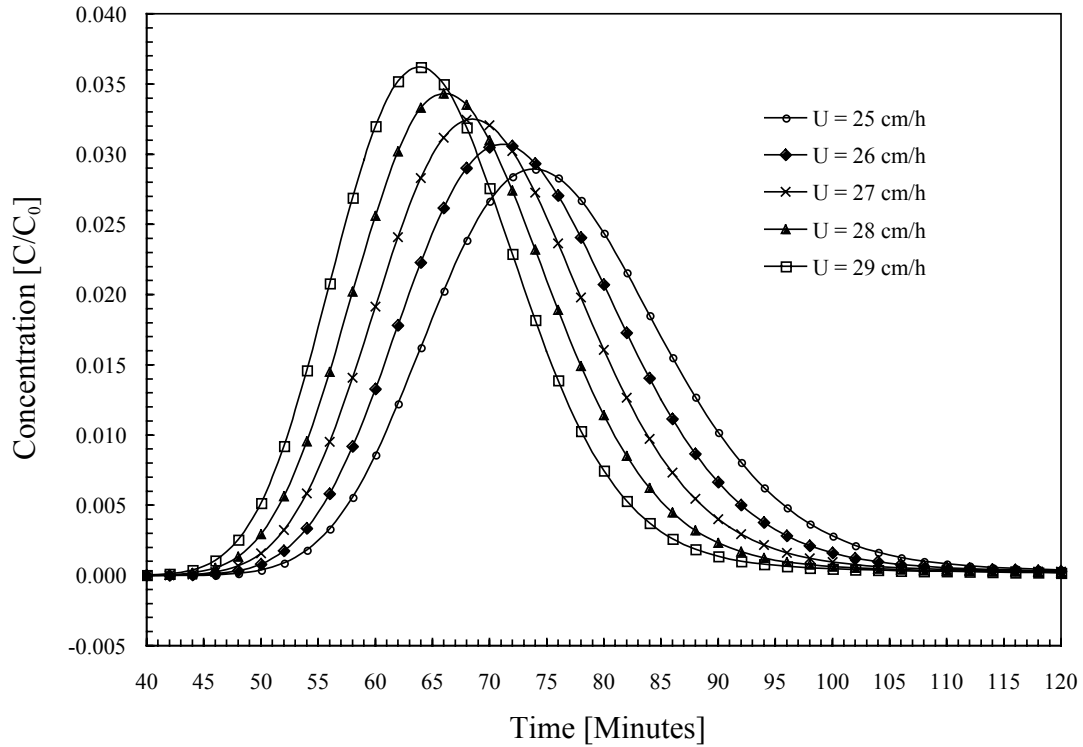


Figure 3.7: An illustration of the effect of average interstitial velocity, U , on the character of the analytical solution with $D = 7.0 \text{ cm}^2/\text{h}$, $k_c = 5.0\text{E}-02 \text{ 1/h}$, and $k_r = 2.5 \text{ 1/h}$.

to 25, 26, 27, 28, and 29 cm/h. Examination of the graph shows that greater (faster) interstitial velocity causes the curve to shift to the left indicating a faster peak breakthrough (bulk mass shift). There is also less spreading of the faster breakthrough curve, though all the curves were generated with the same hydrodynamic dispersion coefficient. This is due solely to the faster-moving curve having less time to spread than the slower moving curve on the right. It should be noted that, in reality, increasing interstitial velocity also increases the hydrodynamic dispersion coefficient due to mechanical mixing (see equation 3.3).

Figure 3.8 shows the effect of changing the hydrodynamic dispersion coefficient on the solution. The solution was plotted with D equal to 5, 7, and 9 cm²/h. Increasing

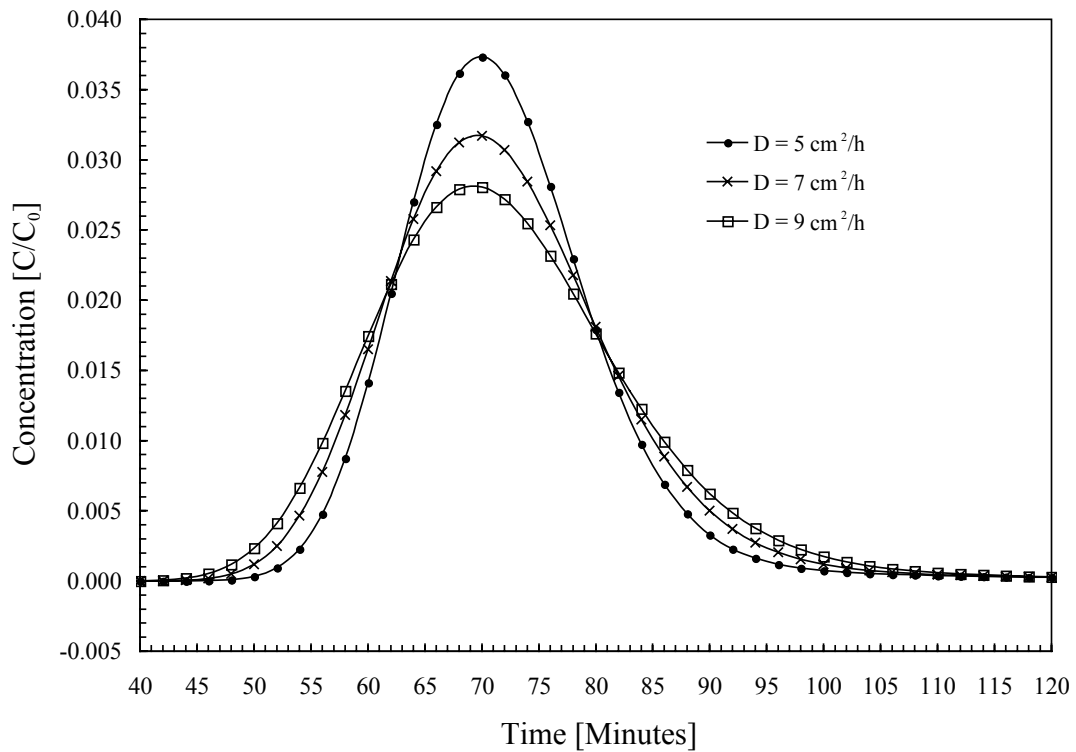


Figure 3.8: An illustration of the effect of hydrodynamic dispersion, D , on the analytical solution with $U = 26.57$ cm/h, $k_c = 5.0E-02$ 1/h, and $k_r = 2.5$ 1/h.

hydrodynamic dispersion causes the curves to spread more in both directions (i.e.,

longitudinally). The concentration in the effluent begins to increase earlier if the hydrodynamic dispersion is greater, even when the interstitial velocity is the same. This does not constitute a bulk shift, however, because the peak breakthrough time does not change.

Figure 3.9 shows the effect of changing the forward rate coefficient on the solution. The solution was plotted with k_c equal to $5.0\text{E-}02$, $1.1\text{E-}01$, and $1.7\text{E-}01$ 1/h. In

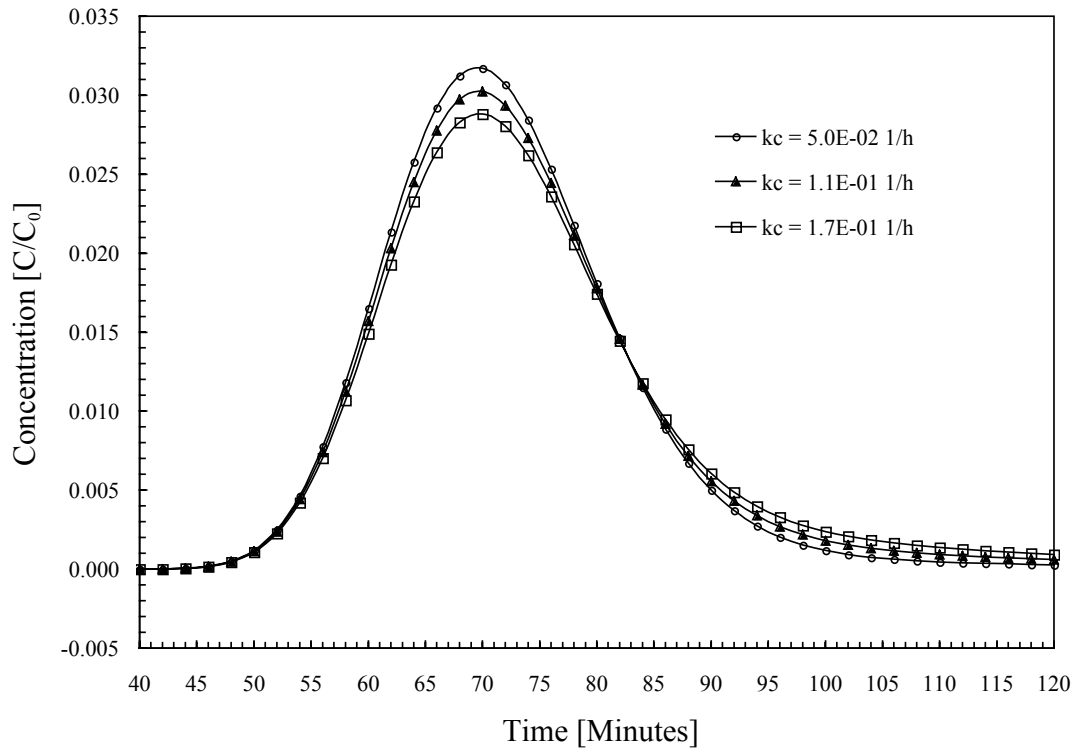


Figure 3.9: An illustration of the effect of the forward rate constant, k_c , on the character of the analytical solution with $U = 26.57$ cm/h, $D = 7.0$ cm²/h, and $k_r = 2.5$ 1/h.

general r_1 , or k_c , can be thought of as the rate of sorption or clogging. A larger r_1 causes a lower peak concentration and tailing of the curve with time. This is due to the tracer adsorbing to the solid matrix and detaching later. Thus k_c can cause a bulk shift only to the right and tailing only at later times. We must recall that, as

evinced in equation 3.4, k_c and k_r work in conjunction to affect the character of the solution.

Figure 3.10 illustrates the effect of changing the reverse rate coefficient on the solution. The solution was plotted with k_r equal to 2.5, 0.10, and 0.01 1/h. In general

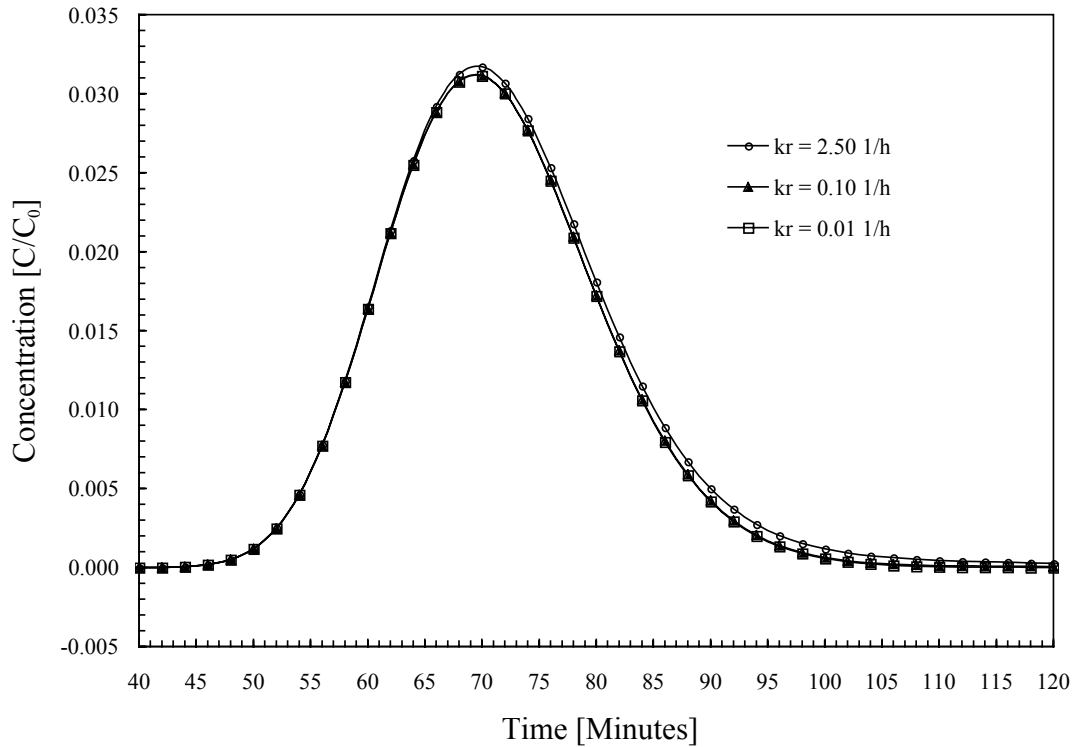


Figure 3.10: An illustration of the effect of the reverse rate constant, k_r , on the analytical solution with $U = 26.57$ cm/h, $D = 7.0$ cm²/h, and $k_c = 5.0\text{E}-02$ 1/h.

r_2 , or k_r , is the rate of release of adsorbed tracer. In this case the effect of k_r is difficult to discern because the value of k_c is very small.

3.4.3 Experimental Results

Subsequently, the Levenberg-Marquardt nonlinear least squares regression method was used with the analytical solution to determine the effective dispersion coefficient

and the effective velocity associated with each acoustic frequency. By comparing the values of effective dispersion and effective velocity at a particular frequency with the values of the base case (no acoustics), it is possible to determine D^* and U^* , the components of these parameters attributable to acoustic pressure. For the equation relating these parameters, see equations 3.2 and 3.3. The objective of the nonlinear least squares method is to obtain estimates of the model parameters that minimize the sum of squared residuals between simulated and observed data. The program utilizes the subroutine `mrqmin` for fitting the data and the subroutine `qdag` for numerical evaluation of the integral present in equation 3.81.

Figure 3.11 shows the base case experimental data for Uranine and the two colloids along with the fitted analytical solution for that data. These curves are characteristic of the curves at all frequencies tested in that the peak concentration of Uranine is always higher than that of blue or red microspheres, while the microspheres exhibit more tailing at later times. For this experimental set-up, there is very little discernable difference between the blue and red microspheres (colloids with difference diameters). It should also be noted that there is no observed early breakthrough for colloids over the conservative tracer as might be expected (see section 2.3.2). The early breakthrough effect is due to size exclusion which should not be present in this column because the pore space in 2 mm glass beads is quite large. The calculated value of interstitial velocity, U , was used and dispersion, D , was fit from experimental data. The fitted base case hydrodynamic dispersion for Uranine, blue, and red microspheres was 5.35, 7.07, and 7.12 cm^2/h , respectively. In addition r_1 and r_2 were fit for the blue and red microspheres. The fitted values of r_1 and r_2 for blue and red microspheres were $5.38\text{E-}02 \text{ h}^{-1}$ and 2.49 h^{-1} ; and $5.31\text{E-}02 \text{ h}^{-1}$ and 2.51 h^{-1} , respectively. They were considered to be constant at different acoustic frequencies. For experiments conducted with acoustic pressure oscillation, the values obtained from fitting were actually U_e and D_e (See equations 3.2 and 3.3). The values obtained from the base case were subtracted from these to obtain the components attributed to acoustics, which are depicted graphically in Figures 3.14 and 3.15. For the low

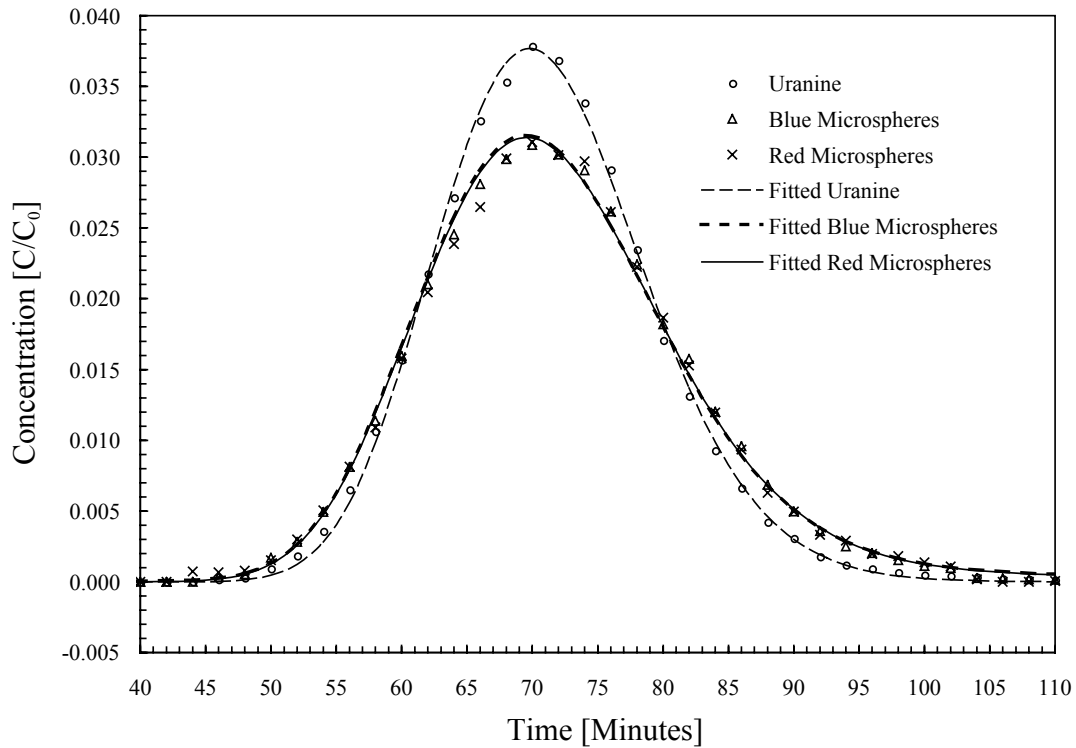


Figure 3.11: The symbols are the experimental data for the Base Case (No Acoustic Pressure) for Uranine, blue, and red microspheres. The solid lines are the fitted analytical solutions.

velocity used in these experiments, the small deposition rates obtained agree with the literature as the experimental work of Kretzschmar and Sticher, 1998, suggested a direct relationship between deposition rates and pore velocity.

Figure 3.12 shows experimental data and the fitted analytical solution at selected frequencies for Uranine, Blue, and Red Microspheres. The acoustic influent pressure was maintained at 3.33 psi (23.0 kPa). It should be noted that there is different attenuation of pressure waves at different frequencies, which causes there to be a different acoustic pressure gradient along the column even when the influent pressure is the same.

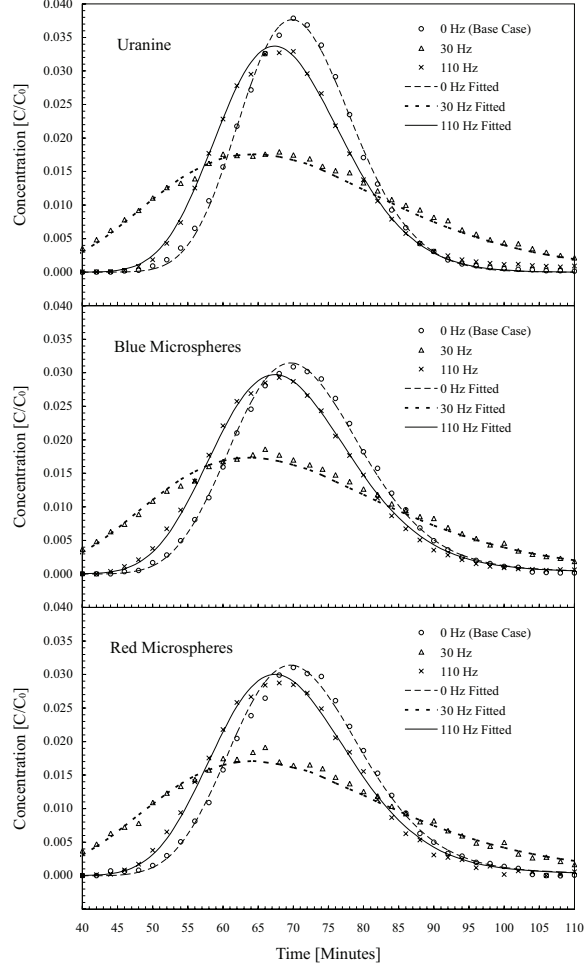


Figure 3.12: The symbols are the experimental data for the base case, 30 Hz, and 110 Hz for Uranine, Blue, and Red Microspheres. The lines are the fitted analytical solution.

The acoustic pressure gradient along the column is given by

$$\Delta P = \frac{P_2 - P_1}{L}, \quad (3.85)$$

where ΔP is the acoustic pressure gradient [kPa/cm]; P_2 is the acoustic pressure at the effluent end of the column [kPa]; P_1 is the acoustic pressure at the influent end of the column [kPa]; and L is the length of the column [cm]. Figure 3.13 shows the acoustic pressure gradient along the column at different frequencies. For the frequencies studied in these experiments the attenuation appears to be roughly linearly and inversely related to frequency. At higher frequencies there is less attenuation in the

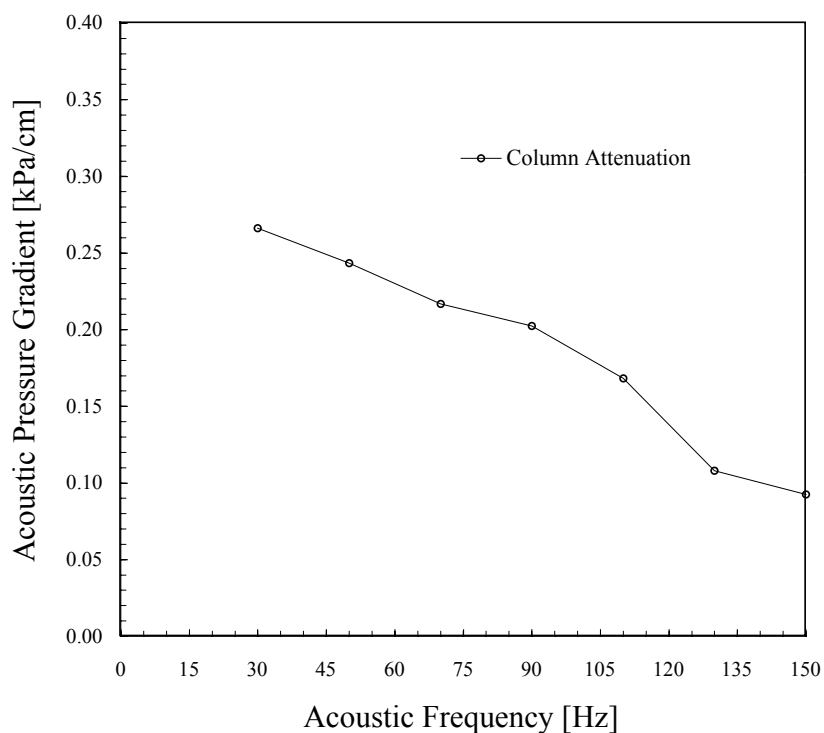


Figure 3.13: The acoustic pressure gradient along the column at different frequencies. A larger acoustic pressure gradient means greater attenuation.

column.

Similar effects were observed for colloids as well with the exception of lower peak concentrations and tailing, just as in the base case. The analytical solution fit the experimental data well.

The results of the experiments are displayed in Figures 3.14, 3.15, and 3.16 showing the components of interstitial velocity and hydrodynamic dispersion attributed to acoustics at each acoustic frequency tested.

Acoustic pressure forcing caused an increase in interstitial velocity at all frequencies for the conservative tracer and colloids of both size. The maximum increase in velocity occurred at 70 Hz. Acoustics also caused increased dispersion above the base case at all frequencies. There was a very large observed spike in dispersion at 30

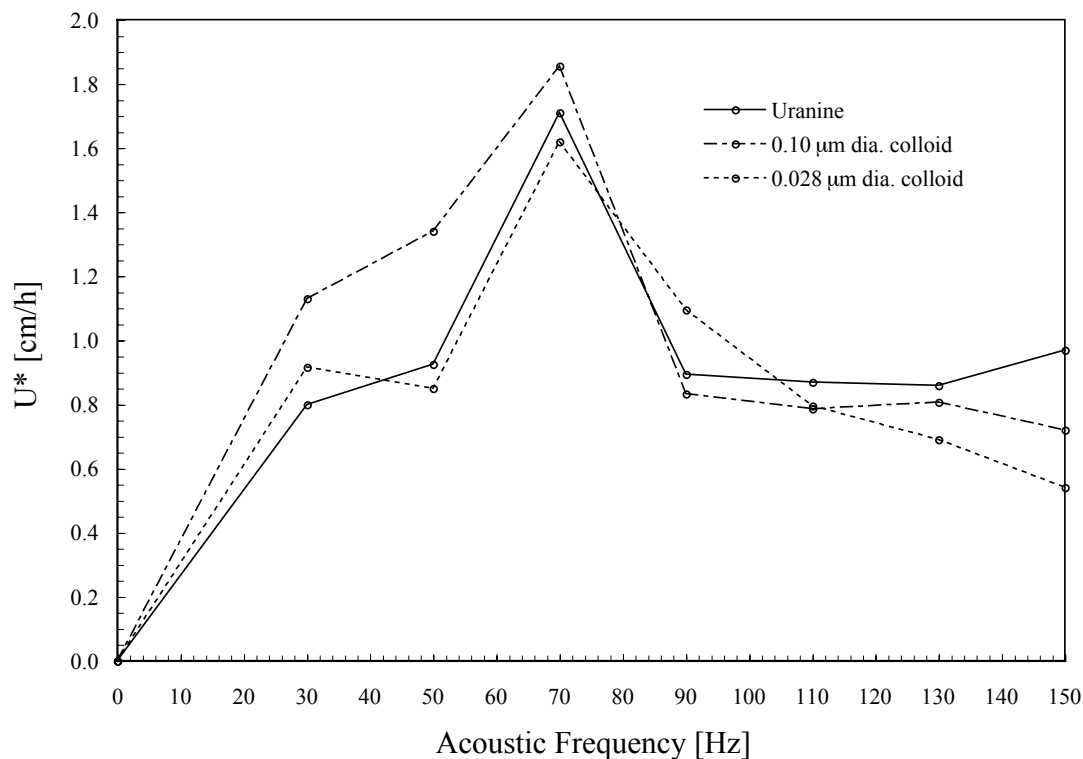


Figure 3.14: The component of effective interstitial velocity attributed to acoustics, U^* , (see Equation 3.2) versus the frequency of acoustic pressure oscillation for Uranine, blue, and red microspheres.

Hz.

3.5 Conclusions

Before analysis of the experimental data, a discussion of the effects of the various model parameters on the character of the breakthrough curves generated by the analytical solution was given. Figures 3.7, 3.8, 3.9, and 3.10 illustrate the effects of changing a single model parameter (namely U , D , k_c , and k_r), while keeping the other model parameters constant. Examination of the graph shows that greater (faster) effective interstitial velocity causes the curve to shift to the left indicating a faster

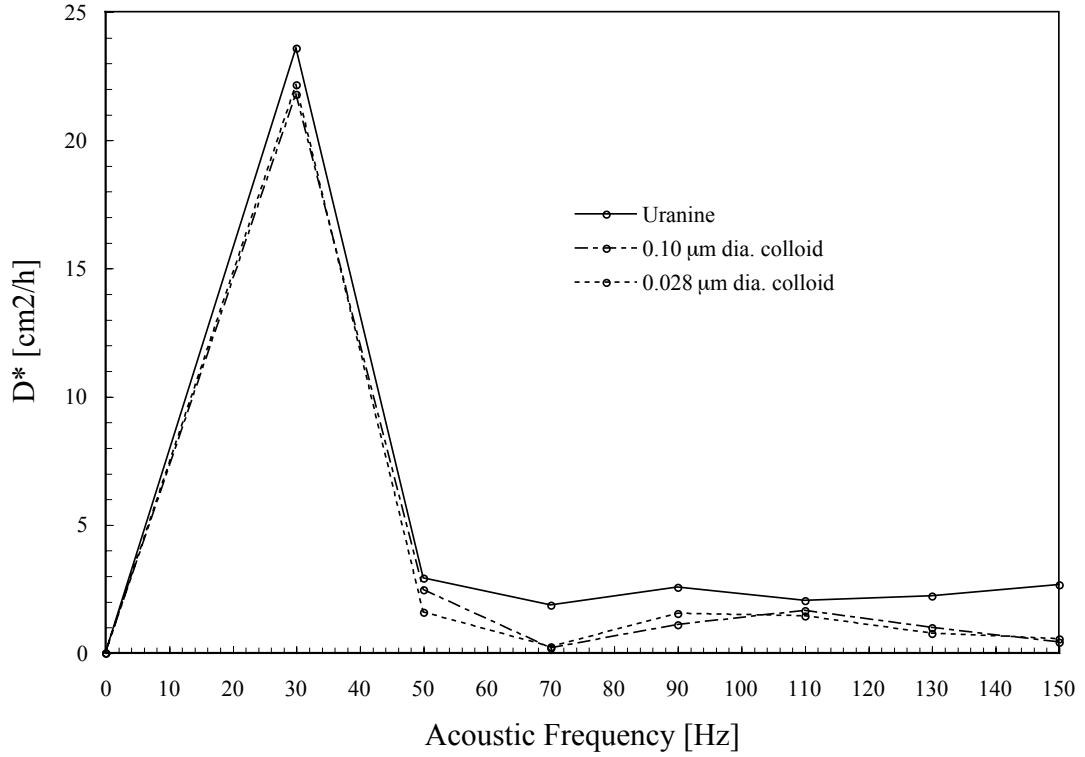


Figure 3.15: The component of effective hydrodynamic dispersion coefficient attributed to acoustics, D^* , (see Equation 3.3) versus frequency.

peak breakthrough (bulk mass shift). There is also less spreading of the faster breakthrough curve due to decreased retention time. Increasing hydrodynamic dispersion causes the curves to spread more in both directions (i.e., longitudinally). The concentration in the effluent begins to increase earlier if the hydrodynamic dispersion is greater. A larger r_1 causes a lower peak concentration and tailing of the curve with time. In this case the effect of k_r is difficult to discern. These curves are characteristic of the curves at all frequencies tested in that the peak concentration of Uranine is always higher than that of blue or red microspheres, while the microspheres exhibit more tailing at later times. For this experimental set-up, there is very little discernable difference between the blue and red microspheres (colloids with difference diameters). It should also be noted that there is no observed early breakthrough for colloids over the conservative tracer as might be expected (see section 2.3.2). The

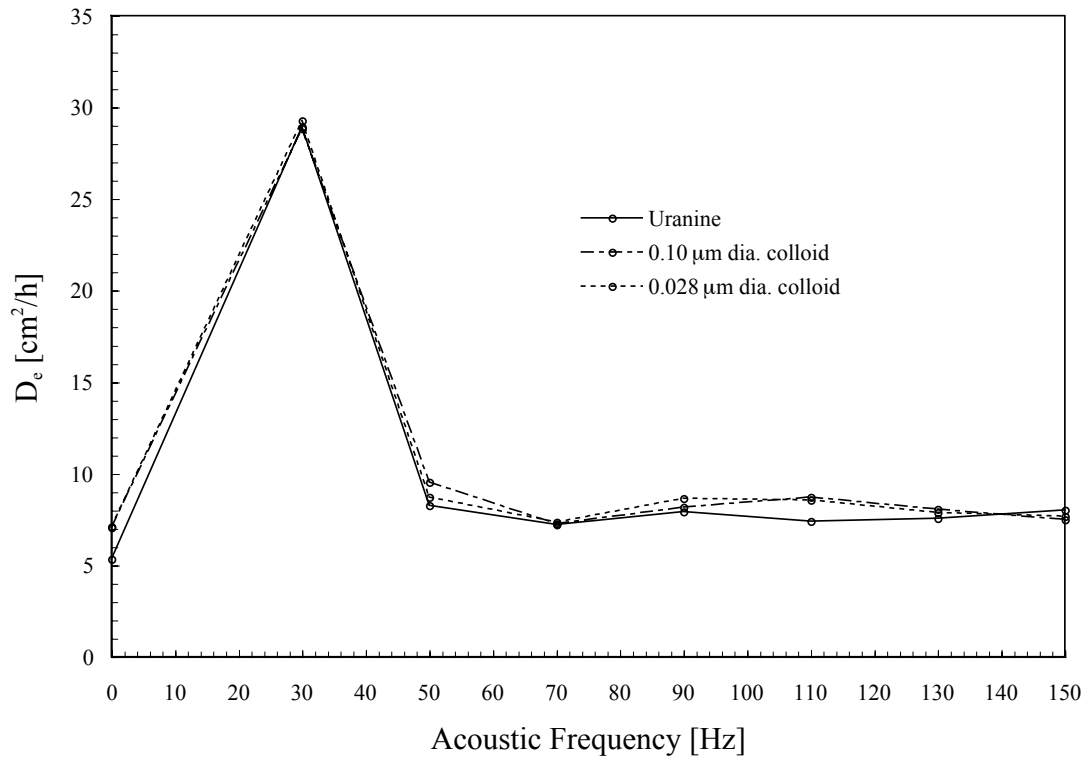


Figure 3.16: The effective hydrodynamic dispersion coefficient, D_e , (see Equation 3.3) versus frequency.

fitted base case hydrodynamic dispersion for Uranine, blue, and red microspheres was 5.35, 7.07, and 7.12 cm^2/h , respectively. The fitted values of r_1 and r_2 for blue and red microspheres were $5.38 \times 10^{-2} \text{ h}^{-1}$ and 2.49 h^{-1} ; and $5.31 \times 10^{-2} \text{ h}^{-1}$ and 2.51 h^{-1} , respectively. Acoustic pressure forcing caused an increase in effective interstitial velocity at all frequencies for the conservative tracer and colloids of both size. The maximum increase in velocity occurred at 70 Hz. Acoustics also caused increased dispersion above the Base Case at all frequencies. There was a very large observed spike in dispersion at 30 Hz. Clearly, applied acoustic pressure increases colloid transport. The exact mechanisms for this are still under investigation.

Table 3.2: Emission Scan Settings

Blue Microspheres		
Sensitivity	Auto Range C_0 at 85%	
Excitation	Wavelength	412 nm
	Step size	1.0 nm
	Bandpass	4 nm
Emission Scan	Lower	434 nm
	Upper	464 nm
	Scan rate	1.0 nm/sec
	Repetitions	1
Uranine		
Sensitivity	Auto Range C_0 at 85%	
Excitation	Wavelength	463 nm
	Step size	1.0 nm
	Bandpass	4 nm
Emission Scan	Lower	500 nm
	Upper	600 nm
	Scan rate	3.0 nm/sec
	Repetitions	1
Red Microspheres		
Sensitivity	Auto Range C_0 at 85%	
Excitation	Wavelength	542 nm
	Step size	1.0 nm
	Bandpass	4 nm
Emission Scan	Lower	600 nm
	Upper	740 nm
	Scan rate	3.0 nm/sec
	Repetitions	1

Table 3.3: Column Parameters

Parameter	Symbol	Value
Porosity	θ	0.368 [-]
Bulk Density	ρ	1.60 [g/cm ³]
Average Interstitial Velocity	U	26.57 [cm/hr]

Chapter 4

NEW EXPERIMENTAL METHODS

4.1 Chapter Abstract

In order to facilitate investigation of the mechanisms responsible for the observed increases in interstitial velocity and dispersion, a new method for accurately measuring *in situ* conservative tracer and colloid concentrations in packed columns was developed. The method consists of fabricating clear sintered glass-bead-packed columns, taking digital photographs of the column under an ultraviolet light source, and determining concentrations by measurement of the fluorescence intensity of the tracer or colloids in the photographs. The sintering process prevents changes in the geometry of the porous medium making it particularly useful for contaminant transport experiments in packed-columns in the presence of seismic or acoustic wave vibrations. Because fluorescence is measured, the method of quantification is limited to fluorescent tracers and fluorescent polystyrene microspheres (colloidal suspensions). The method is shown to be within 3% of the accuracy of traditional effluent sampling and analysis procedures and allows for quick and accurate *in situ* measurement of dissolved or suspended tracer concentrations at multiple times. However, the method

is not useful for decaying chemical species unless the decay rate constant is known in advance, because the intensity curves at all times must be scaled to the known injected mass to yield concentrations.

4.2 Introduction

Beginning with Henry Darcy's now famous packed-column experiments in 1855 and 1856, which led to the law that bears his name and established the theoretical foundation of groundwater hydrology, columns made of various materials and packed with a variety of porous media have been extensively utilized in the laboratory as models for groundwater hydrological experiments. Their extensive use has also encompassed an incredible diversity of groundwater applications and issues. A few examples of the applications and issues that have been addressed by packed-column experiments are: characterization of hydrological parameters such as porosity, dispersion, and dispersivity of natural soils [*Liu et al.*, 1992]; virus fate and transport in the subsurface environment including attachment, detachment, and inactivation [*Anders and Chrysikopoulos*, 2009; *Zhuang and Jin*, 2003; *Jin et al.*, 2000; *Keller et al.*, 2004]; bacteria transport and deposition kinetics in porous media [*Rockhold et al.*, 2006; *Tufenkji*, 2007]; transport and deposition of protozoan oocysts [*Harter et al.*, 2000]; attachment, detachment, straining, blocking, ripening, and decay, of colloids under various soil, solution chemistry, and saturation conditions [*Bradford et al.*, 2004; *Shang et al.*, 2008]; nanoparticle interactions with contaminants for environmental remediation [*Li et al.*, 2008; *Zhang*, 2003]; fate and transport of organic contaminants and pesticides; single and multicomponent reactive chemical transport [*Dai and Samper*, 2004]; application and effects of various waves (e.g., acoustic, seismic, and shock waves) on solutes, colloids, and NAPL dissolution, and mobilization [*Vogler and Chrysikopoulos*, 2002, 2004; *Chrysikopoulos and Vogler*, 2004; *Thomas and Chrysikopoulos*, 2007; *Gross et al.*, 2003]; and validation of hydrogeochemical models of saltwater intrusion [*Gomis-Yagües et al.*, 1997]. In addition, packed-column

experiments have served as the primary method for testing theoretical mathematical models developed for these applications [Gomis-Yagües *et al.*, 1997] because, in the laboratory, conditions can be precisely controlled (and often simplified) and processes measured. The staggering diversity of applications and number of packed-column experiments in the literature demonstrates their critical role as a tool for enhancing our understanding of the physical, chemical, and hydrodynamic processes governing the transport and remediation of contaminants in groundwater aquifers.

Depending upon the application, columns may be packed with natural soils and sediments or intact soil or rock cores from a field site of interest [DeNovio *et al.*, 2004], or with natural or synthetic porous media such as glass beads, quartz sand, sieved-sand fractions, or crushed rock. In a typical transport experiment water flows through the packed column in one direction, a chemical, tracer, or colloidal suspension is injected at the influent, and effluent samples are collected at various times and analyzed to determine the concentration. The method of analysis depends on the type of chemical, tracer, or colloids used. In addition, depending on both the desired application and the method of quantification, the columns themselves can be made of various materials such as aluminum [Bradford *et al.*, 2004], stainless steel [Gomis-Yagües *et al.*, 1997], acrylic [Harter *et al.*, 2000; Rockhold, *et al.*, 2006; Shang *et al.*, 2008], borosilicate glass [Sutton *et al.*, 2001; Li *et al.*, 2008], or still others. Column parameters (e.g., porosity and dispersivity), chemical reactions or dissolution, and hydrodynamic parameters (e.g., interstitial velocity and dispersion) can be determined from effluent concentrations (i.e., break-through curves). Despite their efficacy for increasing our understanding of groundwater hydrology, there are a few inherent weaknesses of these types of packed-column experiment.

First, in conventional experiments involving columns packed with a loose granular porous medium, such as sand or glass beads, the flow of water alone is enough to cause settling of the medium over time. In experiments involving seismic or acoustic wave propagation along a column, the process of settling or compaction is accelerated and exacerbated. Even a very tightly packed column will likely develop

some macroscopic void space over time. In experiments where the length of the column is oriented horizontally (i.e., flow is horizontal) the settling of the porous medium causes a preferential flow path to develop along the top inner wall of the column. This scenario is essentially the same as the presence of a fracture within a porous medium that gives rise to two separate flow velocities: a slower interstitial (seepage) velocity within the bead pack and a faster fracture (preferential) velocity within the macroscopic void space or fracture. Consequently, breakthrough curves of tracers will be inconsistent and, if the settling of the medium is not detected and accounted for, inaccurate (Parker and van Genuchten, 1984). Furthermore, the different velocities will likely be impossible to determine independently because the column porosity may continuously change over the duration of an experiment. Clearly, a rigid system of interconnected grains that cannot permanently deform nor settle would be advantageous for packed-column experiments, especially for those involving seismic or acoustic waves.

Second, measurements of the concentration of the chemical, tracer, or colloidal suspension as it flows through the column (*in situ*) cannot be determined. Consider the following quotation from Baumann and Werth (2004), which illustrates the problem: Conventional methods to investigate colloid transport often involve column studies. Here, colloid concentrations are measured at the column effluent or at selected points along the column length. Unfortunately, such methods do not clearly distinguish how spatial and temporal changes in hydrochemical and hydrodynamic conditions affect colloid transport. For example, breakthrough curves (BTCs) obtained from column effluent represent some average behavior of colloids in the column. Since different heterogeneous realizations can contribute to such BTCs, the processes that control colloid transport in the column are obscured. Therefore, a method of quantification of concentrations while the tracer, for example, is still in the column (*in situ*) during the experiment at multiple times (snapshots) is desirable.

Finally, traditional procedures involving effluent sample collection, followed by chemical analysis is labor intensive and time consuming. For example, in the experiments

of Chapter 3, standard effluent fluorescence analysis required a minimum of 30 to 40 samples collected every 2 minutes, preparation of samples by dilution, and preparation of standard solutions of known concentrations, followed by fluorescence analysis [Thomas and Chrysikopoulos, 2007]. Certainly, a method for quantification that can be performed quickly to yield the *in situ* concentrations would be beneficial.

The work presented in this chapter represents an attempt to overcome the aforementioned weaknesses: to develop a method of producing a rigid porous medium that would not deform permanently under the forces of flow nor acoustic or seismic vibration, to allow for visualization of the medium and make *in situ* concentration determinations at multiple times while experiments were in progress, and to make the concentration determinations less time consuming.

4.3 Methodology

The new method consists of fabricating optically clear sintered-glass-bead-packed columns, taking digital photographs of the tracer as it flows through the column under an ultraviolet light source, determining concentrations by measurement of the intensity of fluorescence of the tracer in photographs using the MATLAB® Image Processing Toolbox™, and calibrating with traditional effluent sample analysis to ensure the accuracy of the results obtained. The following paragraphs provide a detailed description of the various steps of our new method for *in situ* measurement of fluorescent solute and colloid tracer concentrations in glass-bead-packed columns.

4.3.1 Fabrication of Sintered-Glass-Bead Column

One way to create a porous medium that will not deform nor settle is to sinter the glass beads in place within the column. Sintering is the process of heating glass beads beyond their transition temperature, the temperature at which glass begins to deform, which causes separate beads of glass to flow together and fuse at points of

contact (called viscous flow sintering or first stage sintering). The glass must then be cooled rapidly below the transition temperature to prevent further sintering. The sintering process has some inherent difficulties. Glass is an amorphous solid produced by heating normally crystalline compounds to their melting point to produce a homogeneous mixture, then cooling the mixture rapidly so that re-crystallization cannot occur. Therefore, when glass is heated to the point that it begins to flow, molecules on the surface of the glass tend to crystallize. The crystallized surfaces are not able to flow together and therefore act as a barrier to further sintering, preventing the formation of the rigid medium we desire. Furthermore, surface crystals scatter the light shining through them, which is undesirable because this method relies on measuring the intensity of fluorescent light emitted from the tracer, which must travel through the sintered medium. We note that Plona (1980) had produced a sintered glass-bead porous medium but that it was not within a column nor was it used for transport experiments.

It is known that the sintering temperature selected can vary the relative kinetics of sintering and crystallization [Prado *et al.*, 2003]. The literature suggests that high temperatures favor sintering over crystallization [Barg *et al.*, 2008]. However, at high temperatures sintering occurs rapidly, cooling the glass below the transition temperature takes longer, and consequently, it is difficult to consistently reproduce the same degree of sintering. The temperature ranges considered in the literature are well above the transition temperature of glass. However, it is commonly known to glassblowers that fusing of glass can be accomplished at lower temperatures near the transition temperature, without producing significant crystallization. There is very little literature covering the lower range of temperatures just above the transition temperature. The goal was to determine if it was possible to produce significant sintering in this lower temperature range just above the transition temperature of the glass beads, without producing significant surface crystallization. Thus, sintering requires a furnace whose temperature can be precisely controlled to quickly heat the glass to the desired temperature and then rapidly cool the glass so that crystallization

is minimized. Preliminary sintering tests were performed with 1 mm soda-lime glass beads at temperatures just above the transition temperature (approximately 650°C), and showed that significant sintering was accomplished with little crystallization. Figure 1 shows the selected temporal temperature program input to the Isotemp® Programmable Muffle Furnace (10-650-126; Fisher Scientific, Pennsylvania), which was developed from various preliminary glass-sintering tests. The program requires

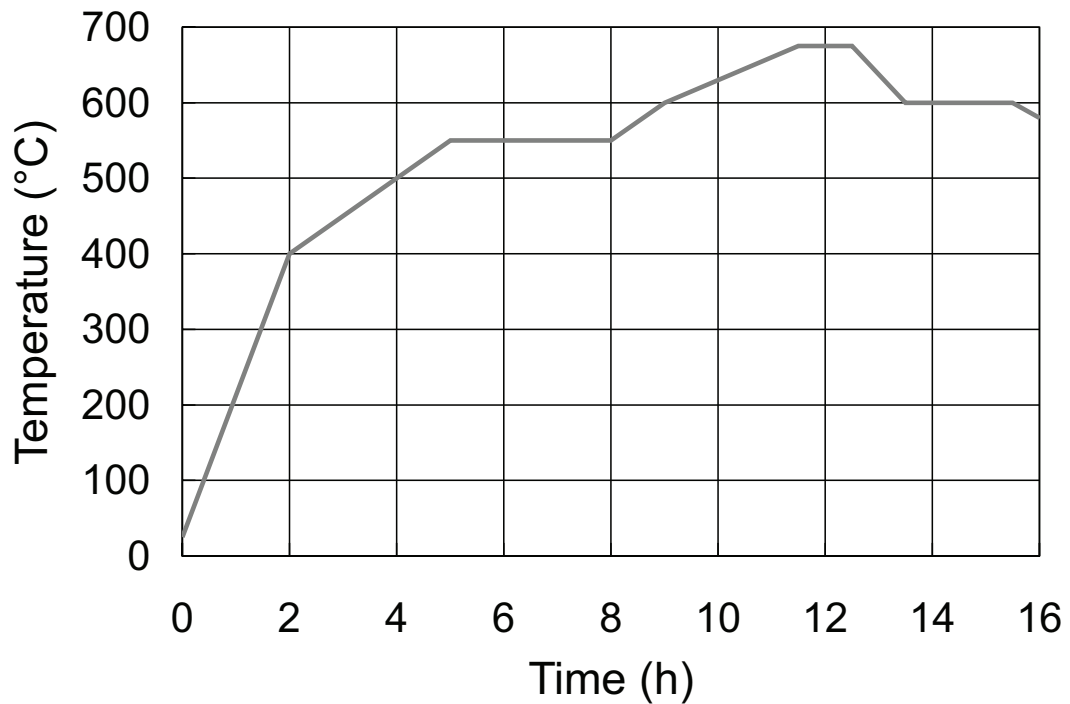


Figure 4.1: Furnace temperature temporal-variation program determined from preliminary sintering tests with 1 mm soda-lime glass beads without substantial crystallization.

bringing the beads rapidly to 400°C then more slowly to 550°C. There is a three-hour soak at 550°C which tends to smooth the surfaces of the beads. Then they are brought up to a maximum of 675°C, where sintering occurs, and soaked for 1 hour. Then the beads are rapidly cooled below the transition temperature to 600°C and soaked for 2 hours to relieve any internal stresses created, the oven is turned off, and the beads are allowed to slowly cool to room temperature over approximately 15

hours. While slightly more crystallization probably occurred at these lower temperatures than at high temperatures, the sintering was slower and the same degree of first stage sintering was more easily reproduced. Certainly, more research is needed in order to quantify the degree of crystallization. However, this is beyond the scope of this dissertation.

An injection port was fitted to the middle of a 30-cm-long borosilicate glass chromatography column with a 2.5 cm inner diameter (Kimble Kontes, New Jersey). To prevent the column from deforming during the sintering process, a mold was created by cutting a stainless steel tube in half, lengthwise. Stainless steel expands but does not deform at the temperatures used to sinter the glass. The column was enclosed between the two halves of the steel tube. The inner diameter of the tube was slightly larger than the outer diameter of the glass column to allow for thermal expansion of the glass. The tube fit into a cylindrical groove, which was ground out of red clay bricks. Red clay bricks were able to withstand the temperatures used and also acted as a stable platform to keep the column's length in a vertical orientation during sintering. This was necessary to prevent the beads from slumping and pulling away from the inner column wall, as would happen if the column were lying flat. Steel wire was wrapped through holes that were drilled in the brick and around the steel tube to hold the column in place within it. Circular pieces of fine-mesh stainless steel screen were cut to a diameter slightly smaller than the inner diameter of the column to temporarily retain the beads within the column during sintering. A stainless steel spacer was used to maintain the bottom screen at the proper location in the column so that the column end caps would still fit after the completion of sintering. The vertically oriented column was then filled with soda-lime glass beads of 1mm diameter (Fisher Scientific, New Jersey). Another screen was placed on top of the glass beads at the other end of the column and a small stainless steel weight was added. This weight applied just enough force as the beads began to slump during sintering to close the gaps created and ensure a more uniform porosity in the longitudinal direction. Figure 2 is a photograph of the column retained in the brick, and the steel

tube mold assembly. Finally, the entire mold and column filled with glass beads

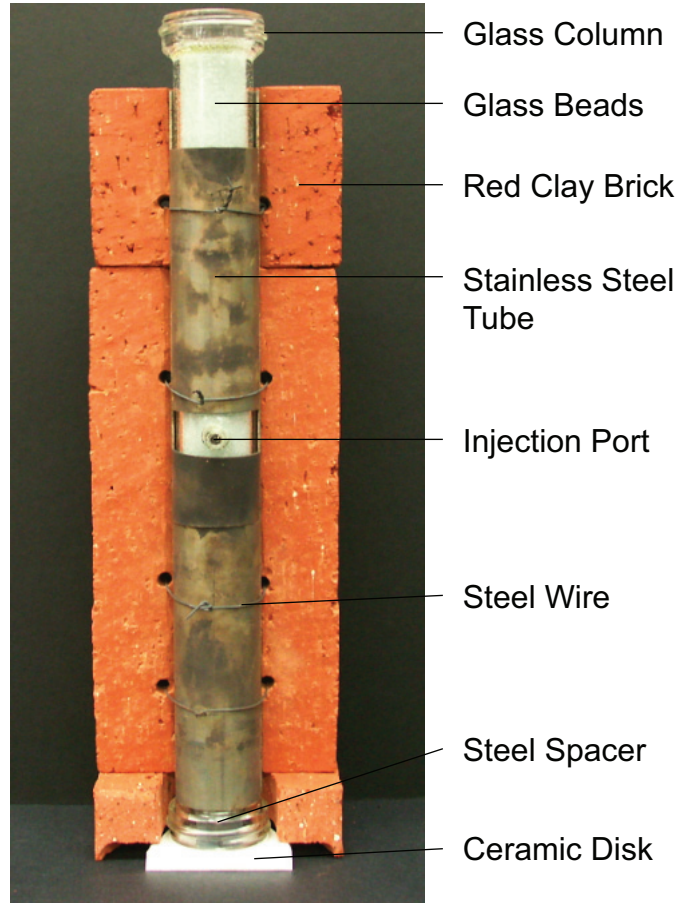


Figure 4.2: Apparatus used for sintering the experimental column. The glass column packed with 1 mm soda-lime glass beads is retained in a vertical orientation within a stainless steel tube that is fastened to red clay brick with steel wire.

were placed in a programmable furnace and heated according to the temperature program presented in Figure 1. While there was a small amount of slumping of the beads, it was determined from preliminary experiments that any changes in porosity in the longitudinal direction are practically negligible. The sintering process prevented the possibility of any changes in the geometry of the porous medium during the experiments.

The temporary screens and spacers were removed and the column was capped with polytetrafluoroethylene (PTFE) column end fittings on both the influent and effluent

ends. The end fittings were secured by plastic screw caps that screw into threads molded in the ends of the glass column. The column was connected to a dual-syringe infusion pump (KDS200; KD Scientific, Massachusetts) and a tactile sound transducer acoustic source (TST429-Platinum; Clark Synthesis, Colorado) and was filled with degassed purified water and purged of any entrapped air. Finally, small marks were etched into the glass column to be used to scale the photographs. One mark was at the point of injection correspond to zero in the x-direction, while the other mark was 14 cm down the column in the direction of flow. All experiments were performed with a constant flow of purified water at a rate of 0.2 mL/min through the column.

4.3.2 Photographic Methods

An enclosure was built around the column to shut out ambient light. The enclosure was equipped with a fluorescent ultraviolet (UV) light source (GA9718P-T8-BK-I; Good Earth Lighting, Illinois) and a 35-mm digital camera (Dimage A1; Konica Minolta, New Jersey) with a remote exposure cord. Any digital camera will work as long as it has a color mode that employs the sRGB color space, and the ability to both automatically and manually set aperture, shutter speed, camera sensitivity (ISO), and focus. The ability of the camera to take a series of photographs on a set time interval is convenient but not essential. For any long duration experiments (e.g., no flow/diffusion) heat buildup within the enclosure even from a fluorescent UV source can cause circulation flow in the column. In order to prevent this, the source was connected to a programmable outlet timer (SE-11P; UPM, Calgary, Alberta, Canada) that was set to turn on for two minutes before a photograph was taken and shut off less than one minute after. For shorter duration experiments it was determined that heat build up did not cause circulation.

Prior to running experiments for a particular tracer some preliminary photographic steps were necessary. The camera was set to the natural color mode (sRGB color

space). The tracer of the same concentration to be used in the experiments was injected into the column and a photograph taken using the auto exposure-mode setting of the camera. The maximum intensity of light emitted from the tracer and recorded for each pixel is greatest in this first photograph, where the tracer is most concentrated. Therefore, this allowed the camera to determine the proper aperture, shutter speed, and sensitivity (ISO) necessary so as not to exceed the maximum recordable intensity value, because all subsequent photographs will have lower recorded intensity for each pixel as the tracer disperses. The settings for aperture, shutter speed, and sensitivity were noted. The camera was then set to the manual mode with the aperture, shutter speed, and sensitivity determined from the first photograph. The focus was also manually set so that it did not change throughout the experiment. These steps were necessary to ensure that the intensities in subsequent photographs could be directly compared to one another without being scaled and that the maximum recordable intensity value was never exceeded.

Once the proper camera settings were determined, a calibration experiment was performed. The preliminary steps were performed and the proper aperture and shutter speed were set. The column was flushed of the tracer and set for a new experiment. A photograph was taken with the UV source on and with no tracer injected in the column (background image). Next, the tracer was injected into the column with flow conditions determined for the experiment. Digital photographs were taken at intervals determined by the flow rate and by the number of concentration curves that were desired. The photographs were processed with the method described below.

4.3.3 Image Processing

The images of the tracer in the column were processed using the MATLAB® Image Processing Toolbox™. The basic data structure in MATLAB® is the array, which is an ordered set of real or complex elements. Arrays are naturally suited to the representation of images, real-valued ordered sets of color or intensity data. An

sRGB image is essentially stored as a three-dimensional array consisting of three 2-D arrays of pixel intensities, one for red, one for green, and one for blue. Each 2-D array has x and y dimensions corresponding to the rows and columns of pixels in the image with an intensity value on a scale from 0 to 255 stored in each location. These images can be easily manipulated with matrix operations. The following is the process used in order to convert the intensity of light in the images to concentration, where all functions refer to the MATLAB® Image Processing Toolbox™ terminology.

The total number of pixels (image size) and the file type and compression rate (image quality) of the image were set in the camera, while the actual area covered by the pixels changed as the camera was zoomed in or out. For this reason and because we are interested in measuring the tracer as it moves through the column, the first step was to map the pixels in the images to actual locations along the length of the column (i.e., in the x -direction). This was accomplished by using the ‘imtool’ function to count the number of pixels between the markings etched into the column. In order to obtain the actual length per pixel, the 14-cm distance between the two markings on the column was divided by the number of pixels. Then the injection location marking was fixed as $x = 0$, and the locations of the center points of each of the pixels were fixed to actual spatial locations in the x -direction.

Next, the background image taken at the beginning of the experiment was subtracted from the subsequent tracer images using the ‘imsubtract’ function. The resultant images consist only of the fluorescent light emitted from the tracer as it moved through the column. However, the light emitted from the tracer was scattered as it traveled through the glass-bead pack and the column walls causing the tracer to appear more longitudinally dispersed than it actually is. This ‘optical dispersion’ was corrected in the calibration step.

The ‘imtool’ function was used to select rows and columns of pixels along the column’s boundaries to act as cropping limits. Then, all but the column area was cropped from the image and the resultant RGB image was separated into its red, green, and blue component images. The component image with the highest intensity

for a particular tracer was selected and further processed to determine *in situ* concentrations. The other two component images are not needed. The intensity values for the pixels in vertical columns were added and then divided by the total number of pixels in the column to obtain the column-averaged intensity. To reduce the total number of column-averaged intensity values and produce a smooth curve, a bin size of fifty columns was chosen and the column-averaged intensity values in each bin were averaged and assigned to the location of the center of the bin.

Finally, there was a slight increase in the overall brightness of all the background-image-subtracted tracer images compared to the background image because the light emitted from the tracer is reflected inside the enclosure. This shows up as a uniform baseline intensity that is greater than zero. That is, a plot of the intensity curve in the x -direction will not approach zero with distance from the tracer, but rather a baseline value of the ambient intensity inside the enclosure. A reasonable baseline intensity estimate was selected by visual inspection and subtracted from the bin-averaged intensities. What remains is a curve of intensity values at fixed locations in the x -direction along the column that must be calibrated by scaling to the total injected mass and by correcting for optical dispersion to yield the actual tracer concentrations along the column. Figure 3 illustrates how the images from an example experiment are processed in order to obtain a graph of the bin-averaged pixel intensity curve after the baseline was subtracted. Each image in Figure 3 was cropped and mapped to the true spatial location. Pixel intensity values range from 0 to 255 for 8-bit RGB images.

4.4 Calibration

There are two additional obstacles to creating accurate concentration curves from the intensity curves. First, the total intensity of the light (area under the intensity curve) emitted from the tracer that reaches the camera increases in magnitude at early times, so it is not possible to directly correlate the magnitude of intensity at a

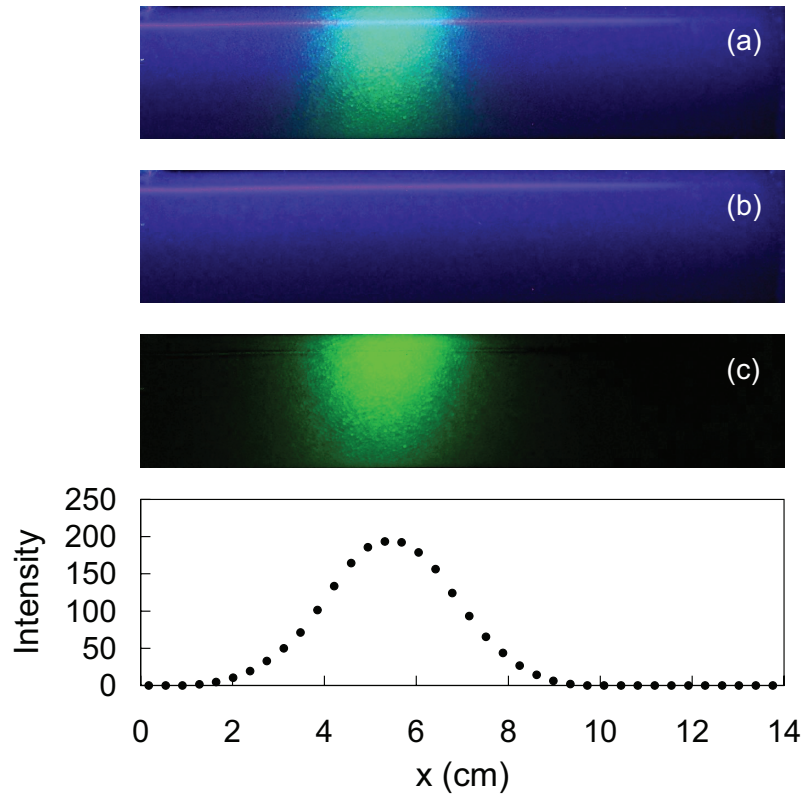


Figure 4.3: Images from an experiment with uranine tracer injection into the packed column, showing (a) the initial RGB image, (b) the background image before the tracer was injected, (c) the image of intensity of green light after the background image was subtracted, and (d) the bin-averaged pixel intensity curve after the baseline was subtracted. Pixel intensity values range from 0 to 255 for 8-bit RGB images.

single pixel location to concentration. Therefore the total intensity must be scaled to the known injected mass in order to yield the proper tracer concentrations along the column at all times. Second, there is the problem of optical dispersion that was previously mentioned. This was corrected by performing a calibration experiment with traditional effluent sampling and analysis.

4.4.1 Mass Scaling

The tracer was injected into the center of the cross-section of the column. As the tracer was carried along by the flow, it spread in the direction of flow along the length of the column (longitudinal dispersion) and outward toward the walls of the column (transverse dispersion). That is, at early times the tracer was near the center of the circular cross-section of the column and at later times it had spread towards the walls of the column due to transverse dispersion. The intensity of fluorescent light emitted from the tracer was directly proportional to the concentration of the tracer in the column. However, not all the light emitted by the tracer reached the camera. The fluorescent light emitted from the tracer in the column had to pass through the sintered-glass beads and the column wall before exiting the column and reaching the camera. Thus at early times when the tracer is concentrated near the center of the circular cross-section, the light emitted from it must pass through more sintered-glass beads than at later times when the tracer has spread closer to the column walls. Clearly the CCD in the camera only registered and recorded the intensity of the fluorescent light emitted from the tracer that actually reached the camera. Scattering of the light occurred, due primarily to refraction, as it passed into and out of individual glass-bead surfaces and water-saturated pore spaces. Thus the intensity of light that actually reached the camera, while directly proportional to tracer concentration, was inversely proportional to the number of beads it had to pass through. The combined effect of dispersion and light scattering was an increase, especially at early times, of the total intensity of light emitted from the tracer that was recorded in each image (i.e., reached the camera). Because the total intensity of the light emitted by the tracer that reaches the camera increases with time during an experiment, it was not possible to produce standards of known concentration to directly relate the recorded intensity to tracer concentration in the column. However, the total mass injected into the column does not change, so the total intensity was scaled to the known injected mass to yield concentration curves. Thus the concentration is averaged over each transverse (perpendicular to the flow)

slice of the column. It should be noted that this is analogous to the flux concentration measured at the column exit [Parker and van Genuchten, 1984; Kreft and Zuber, 1986]. This produced a concentration curve that yielded the proper total injected mass but was more longitudinally dispersed than the actual tracer in the column due to optical dispersion. Once the mass scaling was performed and concentration curves were obtained, the dispersion coefficient was corrected for optical dispersion.

4.4.2 Optical Dispersion Correction

The degree of crystallization on the surfaces of the sintered glass beads was not specifically addressed here, but it should be noted that the beads appear very clear, which means that surface crystallization did not contribute significantly to scattering. However, the simple refraction of light through many beads caused a significant amount of scattering (optical dispersion), making the tracer appear more dispersed than it actually was. This added dispersion was corrected by running a calibration experiment using the experimental methods described above, taking photographs every two minutes while the tracer remained in the column, then collecting the effluent at two-minute intervals for traditional fluorescence analysis with a Fluoromax®-4 spectrofluorometer (Horiba Jobin Yvon, New Jersey). The sample concentrations were quantified by comparing to a set of standards with known concentration. The previously derived analytical solution to the partial differential equation that describes the transport of colloidal particles in one-dimensional, homogeneous, water-saturated porous media accounting for adsorption and inactivation (3.81), was fitted to the effluent concentration curve in order to determine the actual hydrodynamic dispersion coefficient. The same analytical solution was fitted to the concentration curves obtained from each photograph after mass scaling, which yielded a constant dispersion coefficient that was greater than that obtained through effluent sampling, due to optical dispersion. Because the dispersion coefficient determined from fitting the mass-scaled intensity (concentration) curves was constant, a dispersion correction factor: $c_f = D_{Effluent}/D_{Mass-scaled}$ was calculated, where $D_{Effluent}$ and $D_{Mass-scaled}$

are the fitted dispersion coefficients for the effluent breakthrough curve and the mass-scaled intensity (concentration) curve at each time, respectively. To correct for optical dispersion in subsequent experiments, this correction factor was multiplied by the dispersion coefficient obtained from fitting the analytical solution to the concentration curves at each time. The critical assumption is that the ratio c_f is the same for other experiments with different dispersion coefficients. This was verified experimentally (see verification section). Therefore, this produced a final concentration curve for all times that was practically identical to the one obtained from directly sampling and analyzing the column effluent. Figure 4 shows the same intensity curve as in Figure 3 along with the corresponding concentration curve after mass scaling and optical dispersion correction (i.e., calibration).

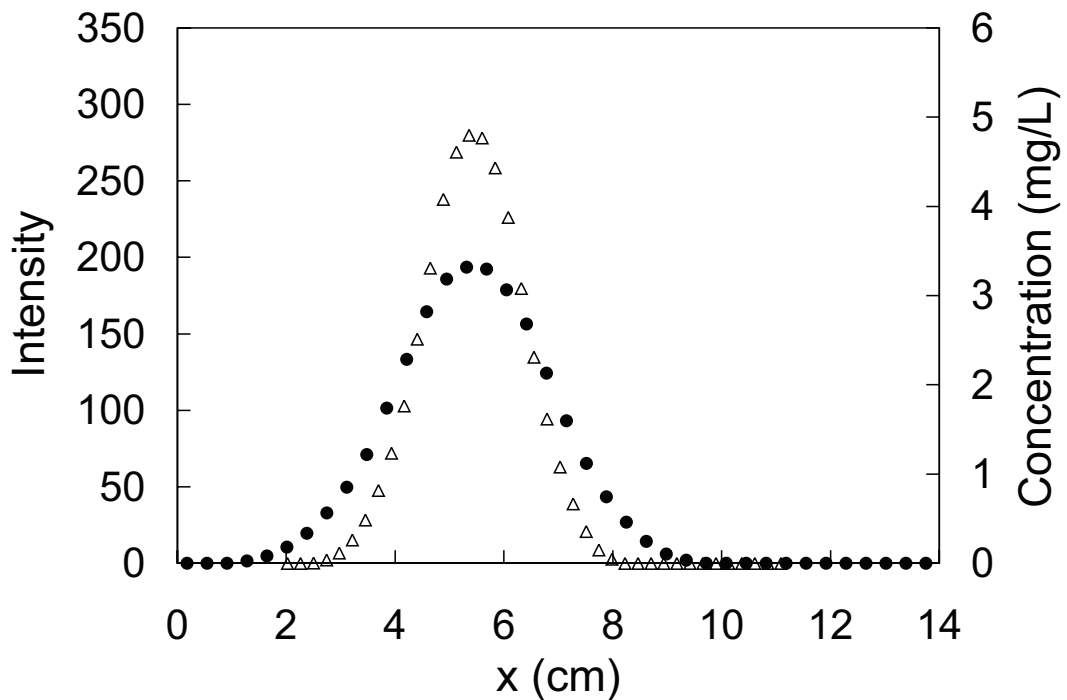


Figure 4.4: A bin-averaged pixel intensity snapshot (solid circles) and the corresponding calibrated concentration snapshot (open triangles).

4.5 Verification

Once the method was established and the dispersion correction factor determined an experiment with acoustic vibration was performed to verify that the method was accurately measuring *in situ* tracer concentrations under experimental conditions. First, the uniformity of the column porosity was verified. An injection of 40 μl of Uranine at a concentration of 500 mg/l was made into the column with a background flow rate of 0.2 ml/min and no acoustic source pressure (base case). Photographs were taken at two-minute intervals. The interstitial velocity at any location x is given by $U_x = Q/A\theta_x$, where Q is the volumetric flow rate, A is the cross-sectional area of the column, and θ_x is the porosity at location x in the longitudinal direction. Therefore, if θ_x changes in the x direction, U_x will also change, because Q and A are constant. The first moment, m_1 , of the intensity curve at each two-minute interval was calculated and plotted against time, t , as shown in Figure 5. The first moment represents the location of the center of mass as it travels in the column. For a conservative non-sorbing tracer, the center of mass travels with the interstitial velocity. A line was fitted to the plot of m_1 versus t and the R^2 statistic was calculated as 0.9997. The slope of the line given by m_1 versus t is the interstitial velocity, U_x . The R^2 statistic indicates that interstitial velocity and therefore the porosity did not significantly change along the x coordinate. Thus, the process has produced a column with uniform porosity.

Next, an injection of 40 μl of Uranine at a concentration of 500 mg/l was made into the column with a background flow rate of 0.2 ml/min, the acoustic source frequency set to 70 Hz, influent acoustic pressure amplitude set to 23.0 kPa, and photographs were taken every two minutes. The intensity curves obtained from each photograph were scaled to the known injected mass to obtain tracer concentration curves. The analytical solution previously described was fitted to the tracer concentration curves to obtain the interstitial velocity, U_x , and the hydrodynamic dispersion coefficient, $D_{Mass-scaled}$, which was corrected by multiplication with the dispersion correction factor, c_f , obtained from the calibration step, to yield the true *in situ* hydrodynamic

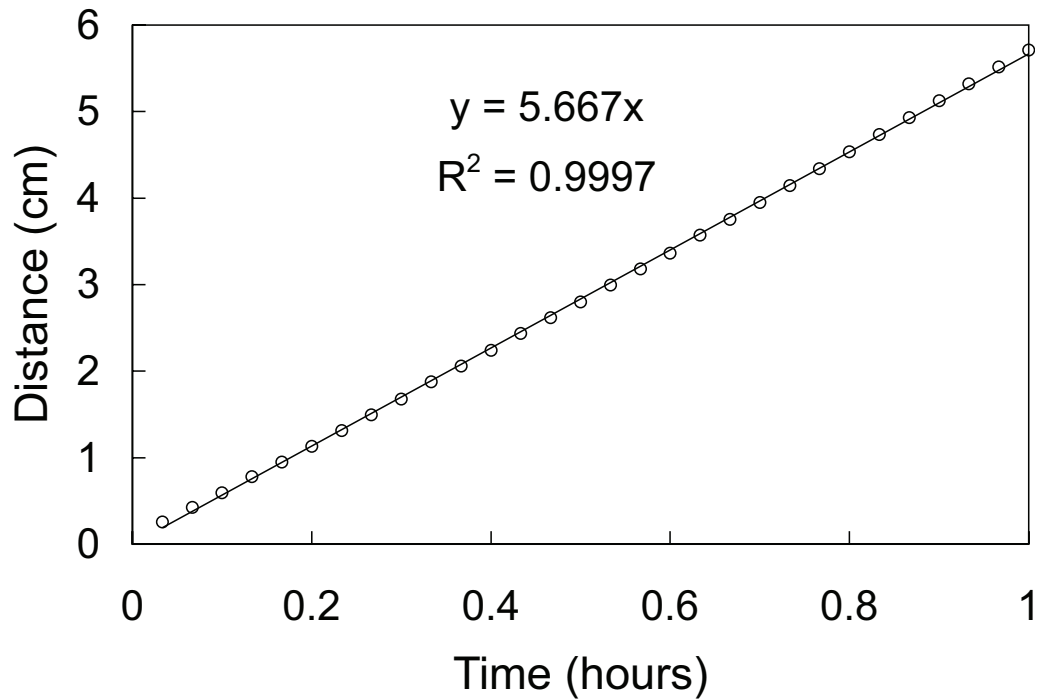


Figure 4.5: The distance from the injection point to the center of mass, m_1 , of the injected tracer versus time (open circles) and fitted linear trend line (solid line). The slope of the solid line represents the interstitial velocity, $U = 5.667$ cm/h, and the practically perfect R^2 statistic indicates that interstitial velocity and therefore porosity does not change along the length of the column.

dispersion, D . Note that this should be equivalent to $D_{Effluent}$. Finally, the effluent was collected and analyzed with a Fluoromax®-4 spectrofluorometer (Horiba Jobin Yvon, New Jersey), and the analytical solution was fitted to the measured tracer concentration curve (i.e., breakthrough curve). Both the interstitial velocity and hydrodynamic dispersion determined by this method were found to be within 3% of those determined by direct effluent sampling and analysis.

Chapter 5

INVESTIGATION OF MECHANISMS

5.1 Chapter Abstract

The work in this chapter represents an attempt to increase our understanding of the mechanisms responsible for the increased interstitial velocity and dispersion of tracers and colloids resulting from acoustic wave propagation in saturated porous media. Three sets of experiments were performed. First, transport experiments were conducted utilizing the new sintered-glass-bead packed column and the photographic methods developed in the previous chapter. In separate experiments a fluorescent tracer (Uranine) or a colloidal suspension of fluorescent polystyrene microspheres was injected as a pulse into the column with a background flow of 0.2 ml/min and an acoustic source connected on the influent end. Acoustic pressure at the influent was maintained at 23.0 kPa. Experiments were conducted at acoustic frequencies of 0 (base case), 30, 40, 50, 60, 70, 80, 90, and 100 Hz. These frequencies were chosen because this was the range of the most interesting results seen in the experiments in Chapter 3 and more resolution (i.e., every 10 Hz) was desired. Next, experiments were repeated at 0 (base case), 30, 50, and 70 Hz with the same apparatus but with

zero background flow to determine if a background flow rate is a critical component of the observed effect. Finally experiments were repeated in a column without porous media filled with water but in the absence of any porous media to see if the observed effects act at a molecular level.

5.2 Introduction

The application of acoustic waves has been shown to increase the effective interstitial velocity and effective hydrodynamic dispersion coefficient of colloids in packed-column experiments [*Thomas and Chrysikopoulos, 2007*]. However, the physical mechanisms responsible for the observed effects are not understood. This work is an attempt to increase the understanding of the physical mechanisms responsible for acoustically-enhanced transport, so that it can be effectively applied in the field for remediation of contaminated aquifers. In general, the observed effects could be the result of mechanisms that fall into three main categories: bulk processes, pore-scale processes, or microscale processes. A bulk process would be a process in which the physical parameters of the porous medium as a whole are affected thereby causing the fluid to advect at a different rate, in bulk, and carrying the tracer or colloid with it. A pore-scale process is one on the scale of a few pore lengths such as transverse mixing of the tracer or colloids as the fluid moves back-and-forth between pores. A microscale process would be one acting on the molecular level, that is, inside the individual pores on the solute or colloids directly but not dependent upon the transfer of fluid between pores. While it is not possible to discern exactly what the mechanisms are, insight can be gained through experimentation as to the type of process that dominates the system. One way to separate these types of processes is to perform several different types of experiments the results of which may eliminate the possibility of any one of these. Three sets of experiments were performed to that end.

5.3 Experimental Design and Procedures

The sintered-glass-bead column and methods developed in Chapter 4 were utilized for this investigation. The experimental apparatus employed in Chapter 3, Figure 3.3 was used. The column was capped with polytetrafluoroethylene (PTFE) column end fittings on both the influent and effluent ends. The end fittings were secured by plastic screw caps that screw into threads molded in the ends of the glass column. The column was connected to a dual-syringe infusion pump (KDS200; KD Scientific, Massachusetts) and a tactile sound transducer acoustic source (TST429-Platinum; Clark Synthesis, Colorado) and was filled with degassed purified water and purged of any entrapped air. The first set of experiments was performed with a constant flow of purified water at a rate of 0.2 mL/min through the column. Base case experiments were performed by injecting either a 40 μ /L pulse of Uranine (conservative tracer) or blue fluorescent microspheres (colloidal suspension; 0.10 μ m mean dia.) or a 100 μ /L pulse of red fluorescent microspheres (colloidal suspension; 0.028 μ m mean dia.) into the center injection port of the column with no acoustic source pressure. Because the red microspheres are much smaller in size than the blue microspheres, they required the additional volume to be injected in order to get sufficient fluorescence in the photographs. Subsequent experiments were performed with acoustic source frequencies of 30, 40, 50, 60, 70, 80, 90, and 100 Hz, and influent acoustic pressure maintained at 3.33 psi (23.0 kPa). Due to differing attenuation of acoustic waves at different frequencies, the acoustic pressure at the effluent was different depending upon frequency. Effluent pressure remained constant throughout each experiment and was always less than the pressure at the influent. Digital photographs were taken at 2-minute intervals and processed with the method described in Chapter 4. The second set of experiments was performed with no background flow but with the same injections, photographic and analytical methods, and acoustic frequencies at 0 (base case), 30, 50, and 70 Hz. A final set of experiments was performed with flow at 0.232 mL/min with a column filled only with water and no porous media to measure the effects of acoustic waves on solute at the molecular scale.

5.4 Results and Discussion

5.4.1 Parametric Investigation

The *in situ* analytical solution is given by $C(t, x) + C^*(t, x)$, where $C(t, x)$ and $C^*(t, x)$ are given by equations 3.81 and 3.5, respectively. In these experiments time, t , is fixed. A discussion of the effects of the various model parameters on the character of the *in situ* analytical solution is instructive. Figures 5.1, 5.2, 5.3, and 5.4 illustrate the effects of changing model parameter (namely U , D , k_c , and k_r), while keeping the other model parameters constant. These figures will help explain the causes of the observed effects in the experimental data.

Figure 5.1 illustrates the effect of changing average interstitial velocity, U , while holding the other model parameters constant. The solution was plotted with U equal

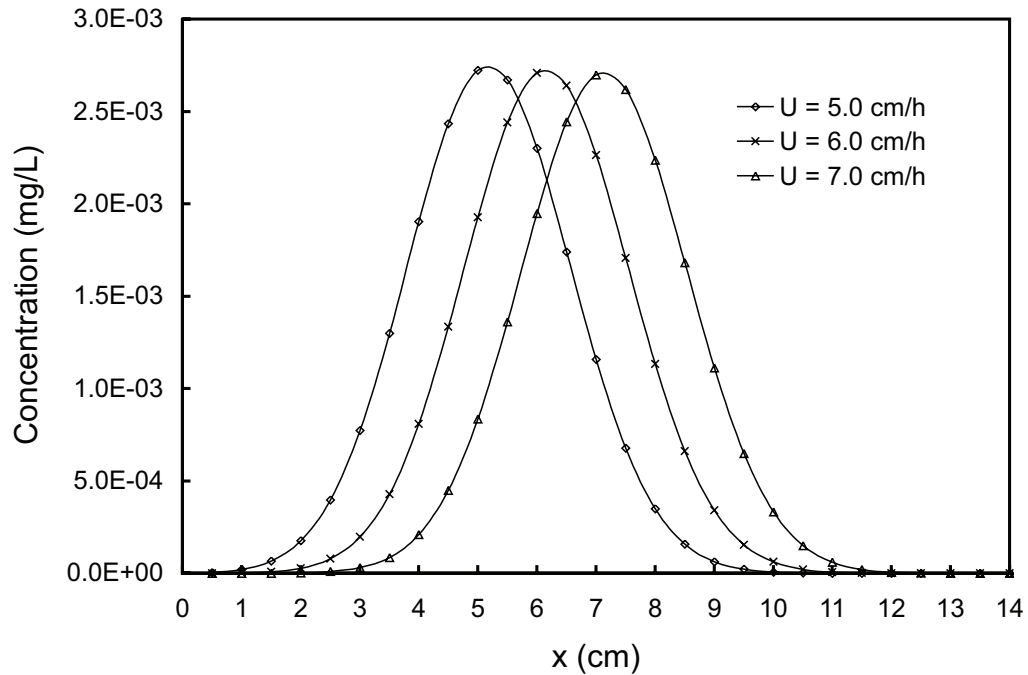


Figure 5.1: An illustration of the effect of average interstitial velocity, U , on the character of the *in situ* analytical solution with $D = 1.0 \text{ cm}^2/\text{h}$, $k_c = 0 \text{ h}^{-1}$, and $k_r = 0 \text{ h}^{-1}$ (i.e., no attachment or release), at $t = 1.0 \text{ h}$.

to 5.0, 6.0, and 7.0 cm/h. Examination of the graph shows that greater (faster) interstitial velocity causes the curve to shift to the right indicating a faster peak breakthrough (bulk mass shift). It is difficult to discern any difference in spreading of the curves as a result of the different values of interstitial velocity because the same value of hydrodynamic dispersion was used. In reality, an increase in interstitial velocity also increases hydrodynamic dispersion due to mechanical mixing (see equation 3.3).

Figure 5.2 shows the effect of changing the hydrodynamic dispersion coefficient on the solution. The solution was plotted with D equal to 0.5, 1.0, and 2.0 cm²/h.

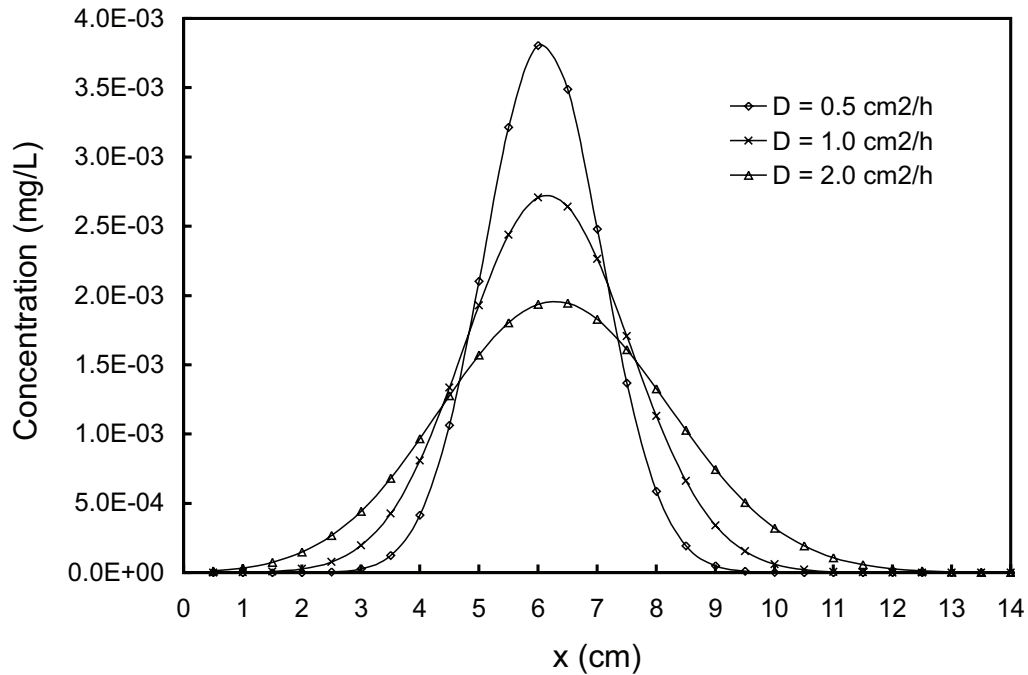


Figure 5.2: An illustration of the effect of hydrodynamic dispersion, D , on the character of the *in situ* analytical solution with $U = 6.0$ cm/h, $k_c = 0$ h⁻¹, and $k_r = 0$ h⁻¹ (i.e., no attachment or release), at $t = 1.0$ h.

Increasing hydrodynamic dispersion causes the curves to spread more in both directions (i.e., longitudinally). The concentration at the leading edge of the concentration curve begins to increase earlier if the hydrodynamic dispersion is greater, even when the interstitial velocity is the same. This does not constitute a bulk shift, however,

because the peak breakthrough time is determined by the interstitial velocity when there is no attachment or release (e.g., conservative tracer).

Figure 5.3 shows the effect of changing the forward rate coefficient on the solution. The solution was plotted with k_c equal to 0.0, 0.5, and 1.0 1/h. In general r_1 , or k_c ,

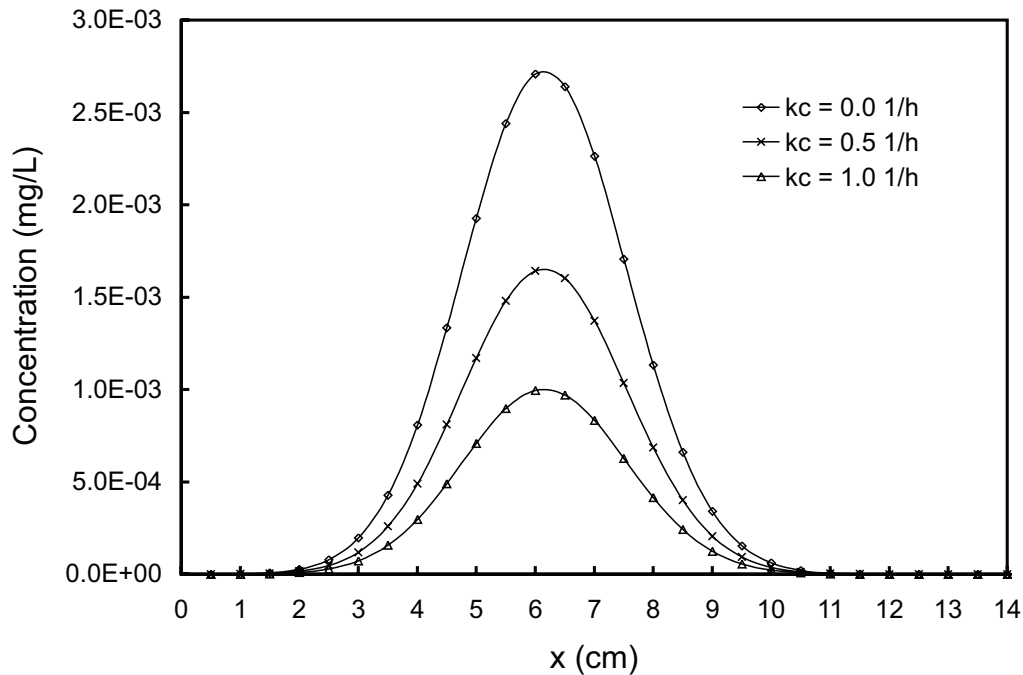


Figure 5.3: An illustration of the effect of the clogging rate constant, k_c , on the character of the *in situ* analytical solution with $U = 6.0$ cm/h, $D = 1.0$ cm²/h, and $k_r = 0$ h⁻¹, (i.e., no release).

can be thought of as the rate of sorption or clogging. Thus a larger r_1 causes a lower peak concentration. However, k_r is rarely zero when k_c is nonzero. Therefore, k_c and k_r work in conjunction to affect the character of the solution (see equation 3.4).

Figure 5.4 illustrates the effect of changing the reverse rate coefficient on The solution was plotted with k_r equal to 0.0, 1.0, and 2.0 1/h. In general r_2 , or k_r , is the rate of release of adsorbed tracer. A larger k_r adds to the trailing end of the concentration curve. This illustrates that the tail of the experimental curve will be very important in fitting the forward and reverse rate coefficients.

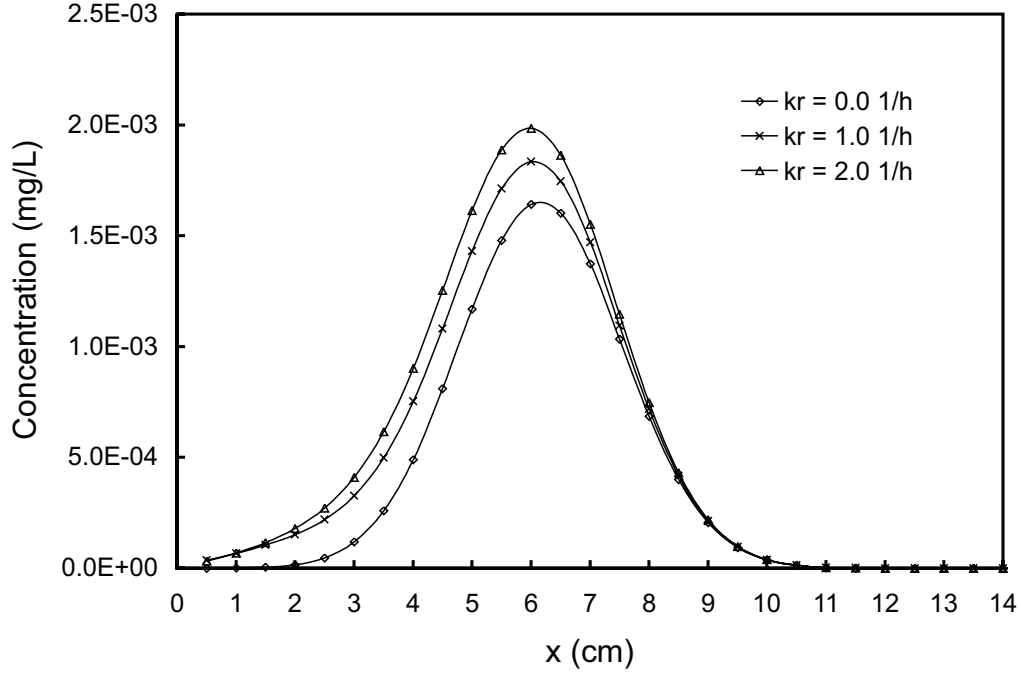


Figure 5.4: An illustration of the combined effects of the clogging and declogging rate constants, k_c and k_r , on the character of the *in situ* analytical solution with $U = 6.0$ cm/h, $D = 1.0$ cm²/h, and $k_c = 0.5$ h⁻¹.

5.4.2 Experimental Results

A new Fortran program utilizing the Levenberg-Marquardt nonlinear least squares regression method with the analytical solution was developed to determine the effective interstitial velocity and the effective hydrodynamic dispersion coefficient associated with the mass-corrected concentration curve at each acoustic frequency.

The dispersion correction factor, c_f , that was described in Section 4.4.2 was calculated for Uranine and the red and blue microspheres. The values obtained were 0.29, 2.0, and 0.46, respectively. The values of the fitted mass corrected dispersion, $D_{mass-corrected}$, for each frequency in each experiment was multiplied by the the correction factor to obtain the true hydrodynamic dispersion, D .

By comparing the values of effective dispersion and effective velocity at a particular frequency with the values of the base case (no acoustics), it is possible to determine

D^* and U^* , the components of these parameters attributable to acoustic pressure. For the equation relating these parameters, see equations 3.2 and 3.3. The objective of the nonlinear least squares method is to obtain estimates of the model parameters that minimize the sum of squared residuals between simulated and observed data. The program utilizes the subroutine `mrqmin` for fitting the data and the subroutine `qdag` for numerical evaluation of the integral present in equation 3.81.

Figure 5.5 shows the mass-corrected base case experimental data for Uranine and the two colloids along with the fitted analytical solution for that data. These curves

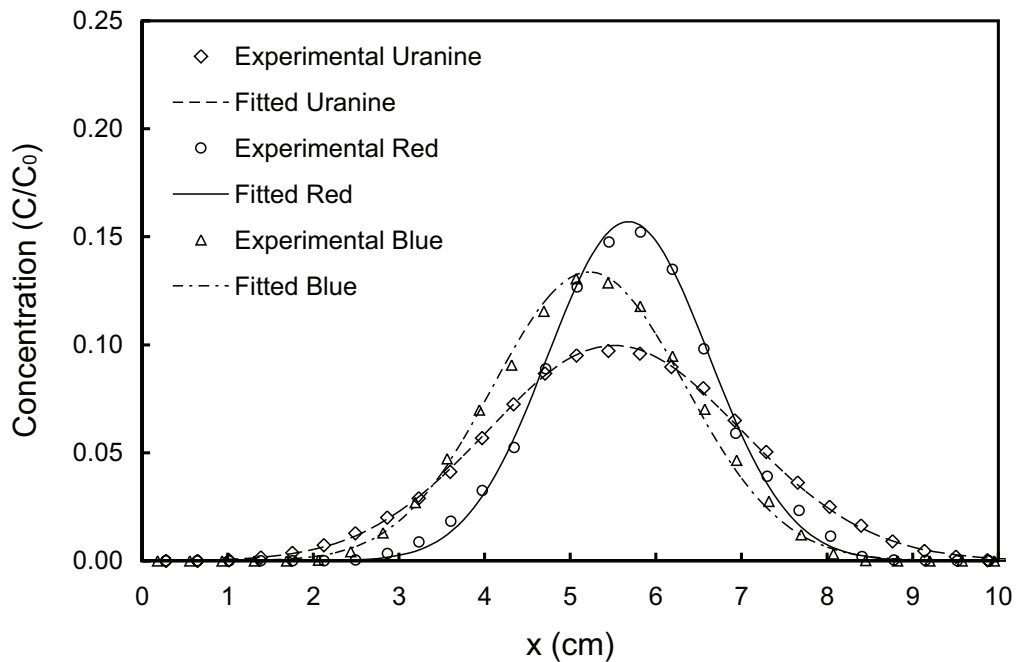


Figure 5.5: The mass-corrected concentration data and fitted curves after one hour for Uranine and Red and Blue Microspheres.

represent the *in situ* concentrations before they were corrected for optical dispersion. Figure 5.6 shows the same curves once corrected for optical dispersion. These curves represent the true *in situ* concentrations and are characteristic of the curves at all frequencies tested in that the peak concentration of Uranine is always higher than that of blue or red microspheres, while the microspheres exhibit more tailing due to attachment and more dispersion. Unlike the previous experiments in Chapter 3, the

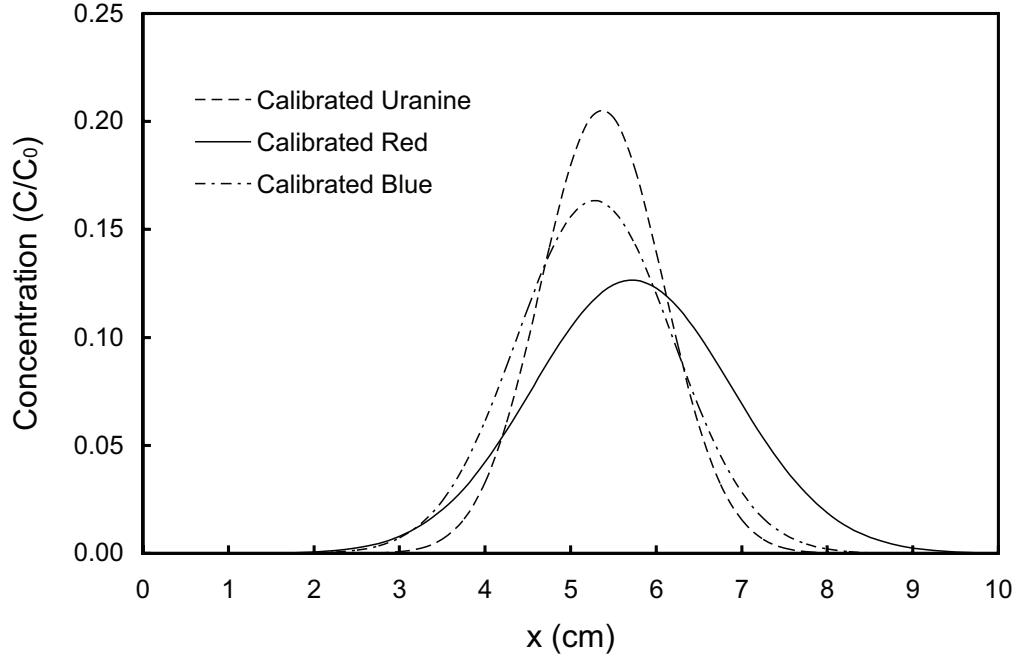


Figure 5.6: The calibrated concentration curves after one hour for Uranine and Red and Blue Microspheres.

effective interstitial velocities are markedly different. The red microspheres experience the greatest U_e , followed by uranine, and finally the blue microspheres. Early breakthrough of colloids is attributed to size exclusion but is also dependent upon adsorption to the porous media, with unfavorable deposition corresponding to early breakthrough. Furthermore, the larger the colloid diameter, the more pronounced is the early breakthrough, because larger particles do not sample the slowest moving velocities. We might expect for the blue microspheres ($0.1 \mu\text{m}$ dia.) to have the fastest U_e , followed by red microspheres ($0.028 \mu\text{m}$ dia.), followed by uranine. However this would be true only under the condition of unfavorable deposition. Because this was not observed, it is clear that the blue microspheres must have a greater attachment rate than red microspheres, which cause them to elute slower than both red microspheres and uranine. Indeed the fitted values of clogging and declogging rate k_c and k_r for red microspheres are $8.0\text{E-}2$ and 1.0 1/h and for blue microspheres $1.0\text{E-}1$ and 7.0 1/h. They were considered to be constant at different acoustic frequencies.

These values also explain the greater dispersion experienced by the red microspheres. Any attachment and release will cause greater dispersion, but the blue microspheres have a much larger declogging rate than the red microspheres. Recalling Figure 5.4, the larger k_r causes a shift in the curve to the left (i.e., it elutes slower), which is what was observed from the blue microspheres.

Figure 5.7 shows experimental data (symbols) and the fitted *in situ* analytical solution (solid lines) at selected frequencies for Uranine. A clear trend can be seen in the

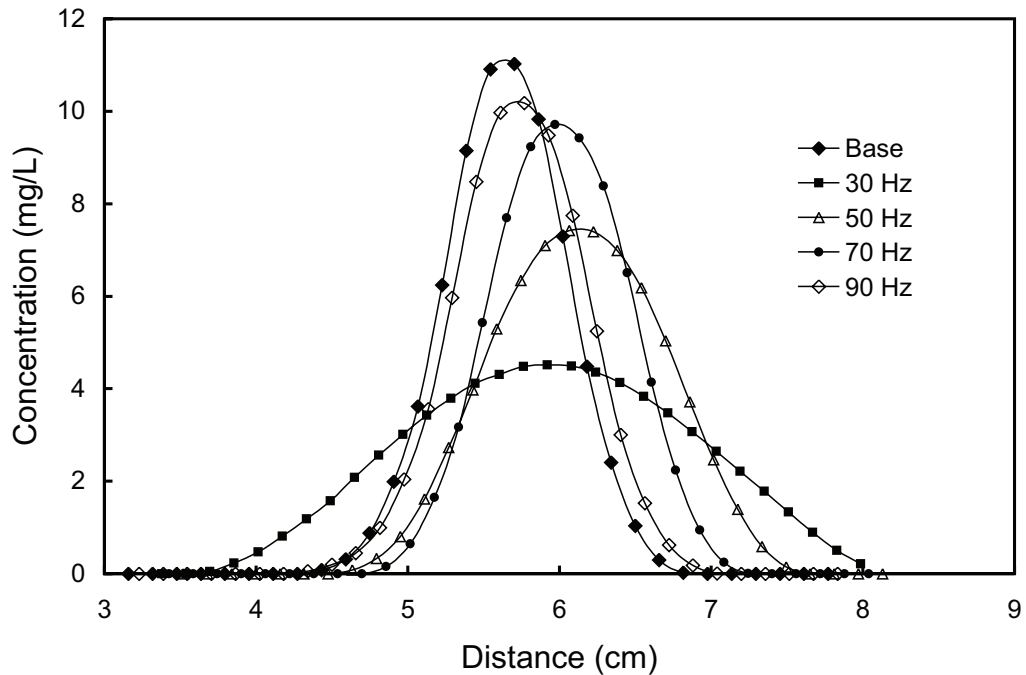


Figure 5.7: Fitted uranine concentration curves after one hour for selected experimental acoustic frequencies employed.

data. The base case curve experiences the least dispersion and the smallest interstitial velocity. The dispersion is inversely related to frequency increasing at lower frequencies. The interstitial velocity corresponds to the peak of the curve. From the curves we can see that there is some maximum interstitial velocity somewhere near 50 Hz. The curves from the remaining frequencies and for red and blue microspheres follow this trend. However, the figures become cluttered when all curves are included. Instead, U_e and D_e for each acoustic frequency employed for uranine and

red and blue microspheres are plotted in Figures 5.9 and 5.11.

The most important results of the experiments, the fitted values of U_e and D_e , are displayed in Figures 5.8, 5.9, 5.10, and 5.11. Figure 5.8 is three graphs of U_e versus frequency for uranine and red and blue microspheres. The values are displayed with standard error bars determined from replicated experiments. It is desirable to plot all of these on one axis to compare the values. However, in order to avoid clutter, they are plotted separately here with the error bars and replicates and in Figure 5.9 with the values of U_e only.

In Figure 5.9, the effective interstitial velocities for uranine and red and blue microspheres are plotted together for comparison, along with the base case values. The acoustic waves have caused an increase in U_e over the base case for all frequencies employed. Here we can see that for the base case, red microspheres experience the fastest U_e followed by uranine and then by the blue microspheres.

The values obtained from the base case were subtracted from these to obtain the component of U_e attributed to acoustics, U^* , which is depicted graphically in Figure 5.10. The values of U^* for the blue microspheres were greatest at each frequency. In general, the red microspheres had the second greatest increase in interstitial velocity due to acoustic waves, followed by uranine, with exceptions at 70, 80, and 100 Hz. However, the values at those frequencies are very close to one another and certainly within the standard error bars. So then, U^* was directly related to particle diameter.

The calibrated effective hydrodynamic dispersion coefficients, D_e , for uranine and red and blue microspheres for all frequencies are shown in Figure 5.11. The lines are power laws fitted to the data. The graph of D^* versus frequency was very similar to this graph and was not included as it did not offer any additional information. The greatest D_e occurs at the lowest frequencies for the tracer and colloids. Acoustic waves increased D_e the most for red microspheres, followed by blue microspheres, followed by uranine. This corresponds to the base case dispersion values in terms of order. We have discussed that the dispersion observed is caused by the clogging and

release rates. Therefore, these same causes of dispersion predominate in the presence of acoustic waves. The acoustic influent pressure was maintained at 3.33 psi (23.0 kPa). At lower frequencies, a larger amplitude of forcing is required to produce the same influent pressure. Thus the dispersion is primarily mechanical and is due to a larger volume of water being sloshed back and forth at lower frequencies. The fitted base case hydrodynamic dispersion for Uranine and red and blue microspheres was 0.26, 0.70, and 0.43 cm²/h, respectively.

The first moment m_1 was calculated for the no flow experiments. Even with acoustics there was no induced interstitial velocity, U^* . The increased interstitial velocity due to acoustics is dependent upon having a background flow and therefore, the process cannot be acting at the microscale. The water-column experiments were inconclusive because the tracer and the colloids immediately sink to the bottom of the column. Initially the desire was to have a dirac pulse type injection so that the analytical solution derived (3.81) could be employed. However, these density (gravity) effects make analysis with the analytical solution impossible and it is now necessary to develop a model that incorporates those effects. This analysis is being performed but was beyond the scope of this present work.

5.5 Conclusions

Both Uranine and red and blue microspheres experienced increased effective interstitial velocity U_e and effective hydrodynamic dispersion D_e at all frequencies employed. Both tracer and colloids followed the same trend with respect to U_e , with the maximum values occurring at 50 Hz. Because the maximum U_e occurred at 70 Hz for 2-mm beads, it was determined that the maximum frequency depends on grain size, though there was not enough different grain sizes to suggest a functional relationship. The greatest change in U_e above the base case (that is U^*) was observed for the largest colloids (blue), then the smaller colloids (red), then Uranine. There was no increased U_e for the no flow experiments so there is not a microscale process. How-

ever, whether the process in a bulk or pore-scale process could not be determined. The effective hydrodynamic dispersion D_e was greatest at the lowest frequencies and appears to follow a power law. This is probably due to the larger volume of water that must be moved at lower frequencies to maintain the influent pressure at 23.0 kPa. At the highest frequencies (e.g., 80, 90, and 100 Hz) D_e is nearly identical. The red microspheres experienced the greatest D_e at all frequencies, then blue microspheres, then Uranine. This order was consistent with the base case. Therefore it is probably caused by the attachment rates, which cause the dispersion in the base case, acting as fluid is being sloshed back and forth. Colloid diameter and forward and reverse attachment rates are important for determining dispersion effects. Finally, it appears that optimum conditions such as the proper frequency for the fastest U_e , or the proper frequency for the least or most D_e can be tuned for the specific system.

5.5.1 Scale Dependency

The significance of this research with respect to groundwater contamination by DNAPLs was discussed in the Introduction. One of the main motivations for this research is to increase the understanding of acoustic wave effects on colloids so that they will be able to be effectively applied for aquifer remediation. As is always the case with experimental laboratory work, issues arise with respect to scaling of these results to the field scale. While it was not possible to perform a scaled-up experiment or field study, the attenuation associated with the experimental equipment was measured. The acoustic influent pressure was maintained at 3.33 psi (23.0 kPa). There is different attenuation of pressure waves at different frequencies, which causes a different acoustic pressure gradient along the column even when the influent pressure is the same. The acoustic pressure gradient along the column (equation 3.85), is analogous to attenuation, and was calculated for the sintered-glass porous medium. Figure 5.13 shows the attenuation in kPa/m versus the acoustic frequencies employed. The attenuation decreases as frequency increases to about 80 Hz, then it rises slightly. There appears to be a minimum of attenuation along the column

between 80 and 90 Hz. Figure 5.14 shows the attenuation at one frequency (50 Hz) and various influent pressures. Attenuation appears to increase linearly as influent pressure increases. The highest attenuation corresponds to the lowest frequencies. Even the lowest rates of attenuation are approximately 7 kPa/m. At 23.0 kPa influent acoustic pressure, we would expect total attenuation in approximately three meters at this rate. However, it should be noted that these attenuation rates are approximately one-twentieth the attenuation rate of the experiments in Chapter 3 (see Figure 3.13). The experiments in Chapter 3 were performed with beads of 2-mm diameter whereas Chapter 5 experiments were performed with sintered 1-mm beads. This grain size is still much larger than normally occurs in a well consolidated soil. Therefore, in the field, the attenuation would likely be much smaller than the values recorded here. It is well known that acoustic vibrations can travel significant distances in natural aquifers [*Beresnev and Johnson, 1994*].

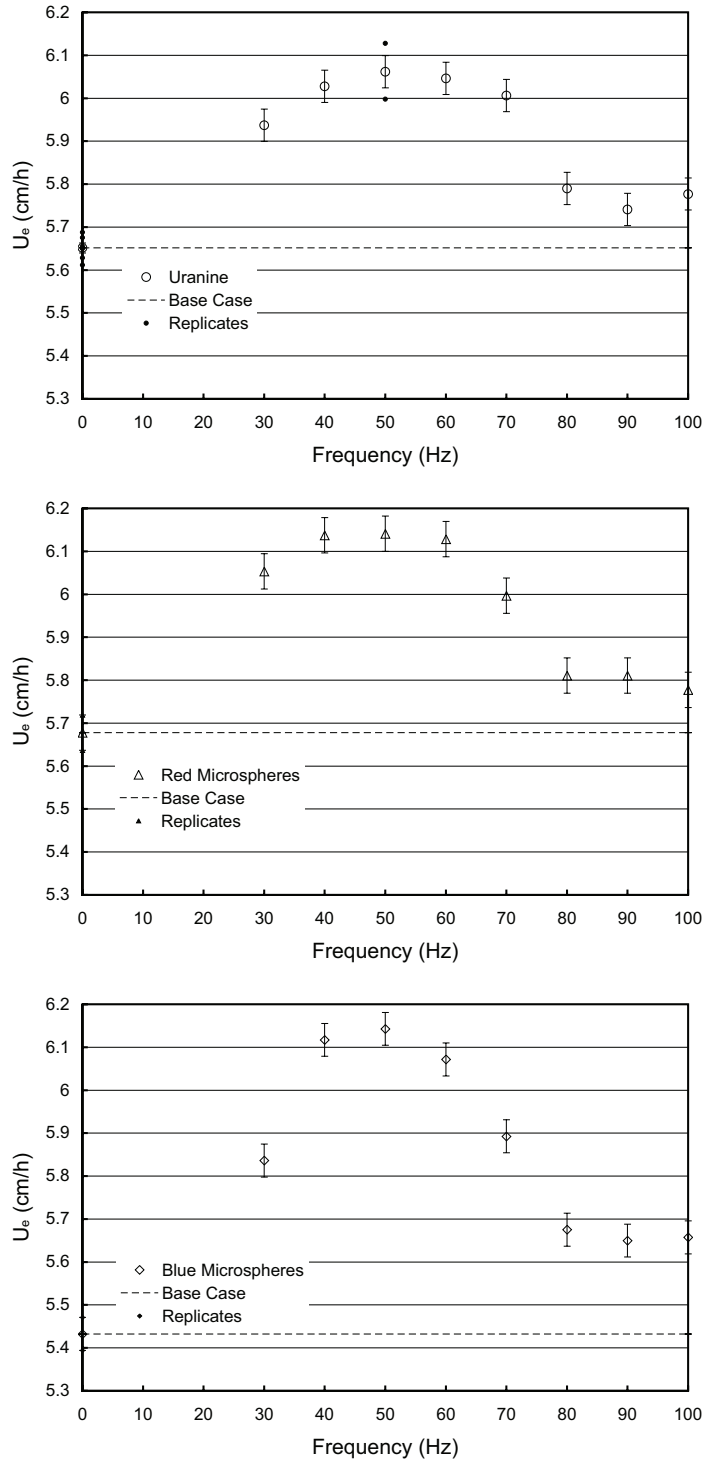


Figure 5.8: Fitted effective interstitial velocity for each experimental acoustic frequency employed for uranine, red, and blue microspheres, respectively. Solid symbols represent replicate experiments and error bars measure standard error.

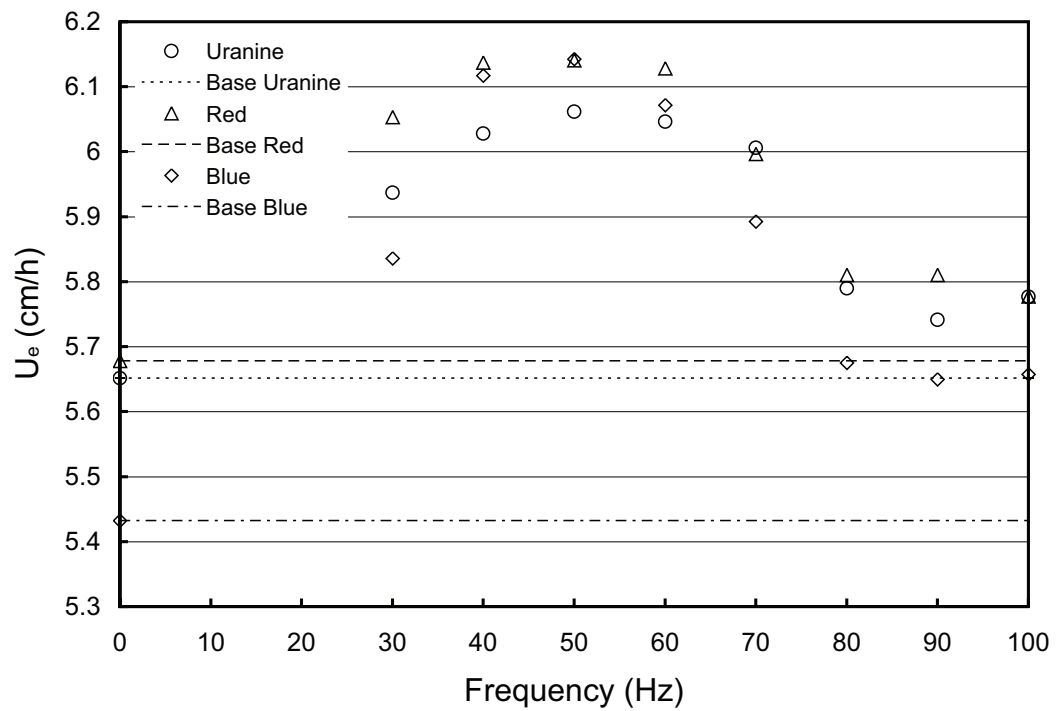


Figure 5.9: Fitted effective interstitial velocity for each experimental acoustic frequency employed for uranine, red, and blue microspheres.

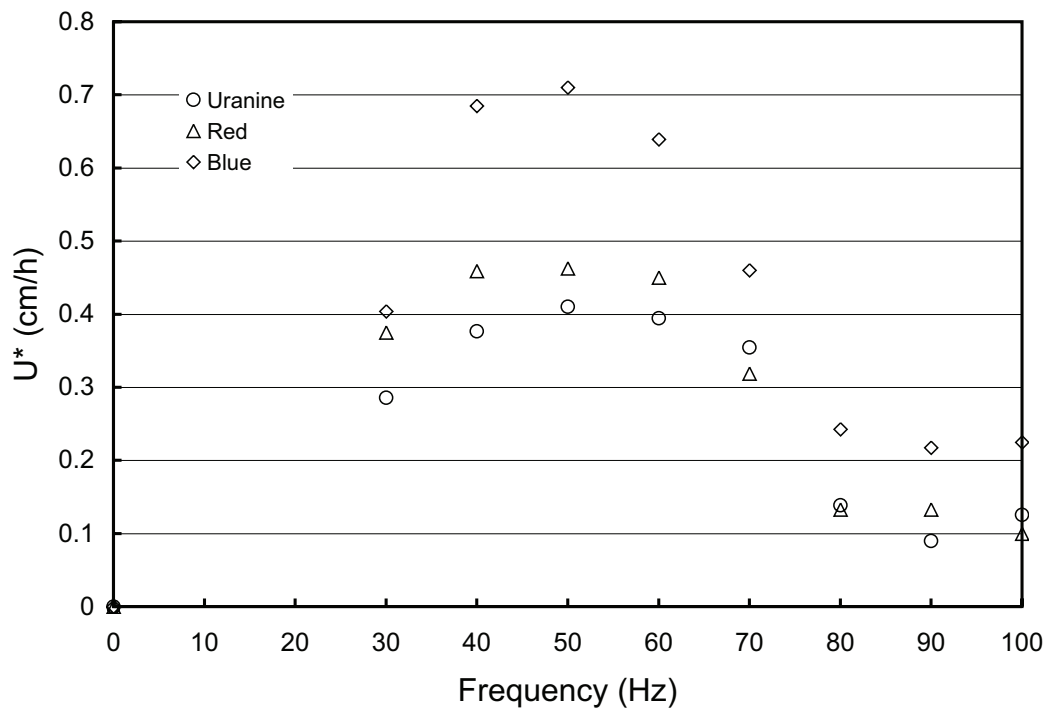


Figure 5.10: The acoustic component of the effective interstitial velocity, U^* for each experimental acoustic frequency employed for uranine, red, and blue microspheres.

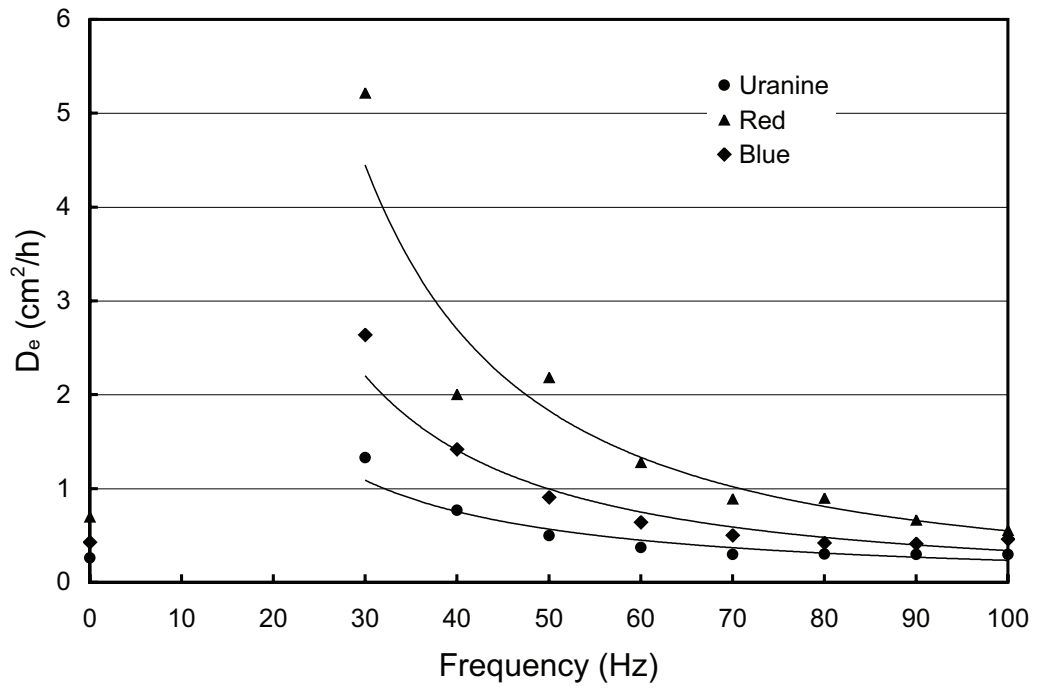


Figure 5.11: Fitted effective hydrodynamic dispersion for each experimental acoustic frequency employed for uranine, red, and blue microspheres.

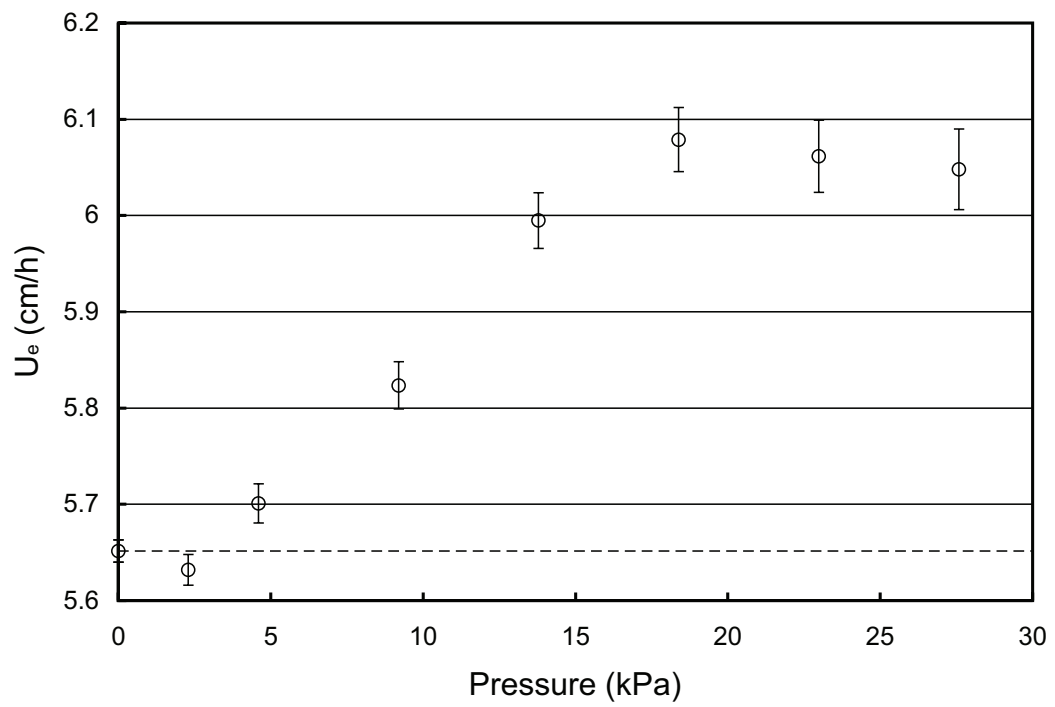


Figure 5.12: Fitted effective interstitial velocity of uranine at 50 Hz at various influent pressures.

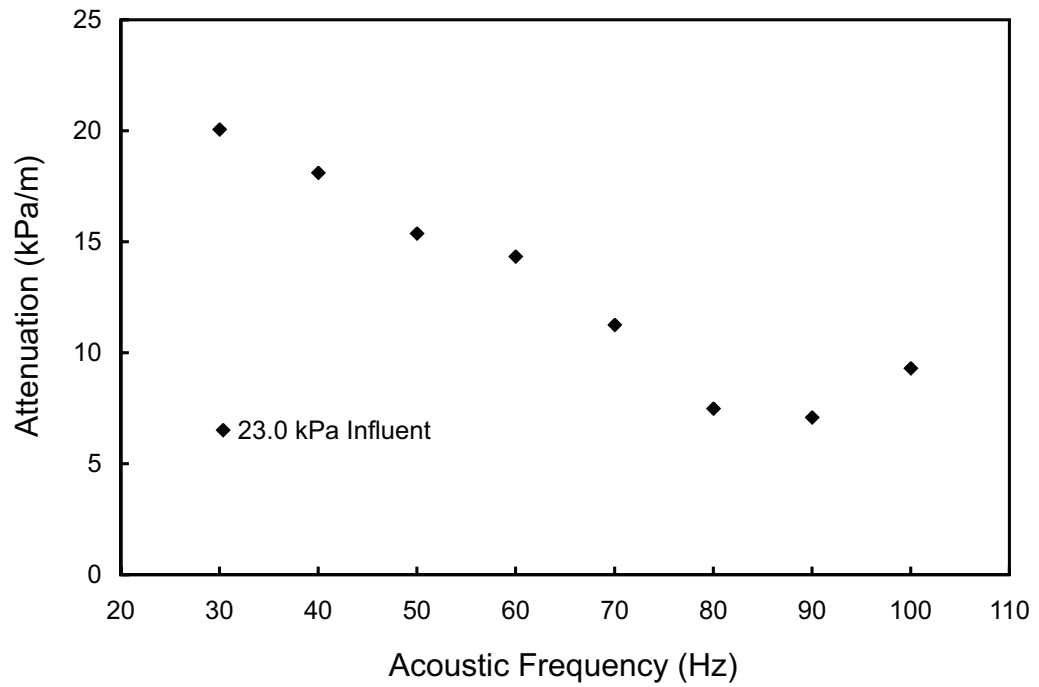


Figure 5.13: The column attenuation measured in kPa/m for various acoustic frequencies at a constant influent acoustic pressure of 23.0 kPa.

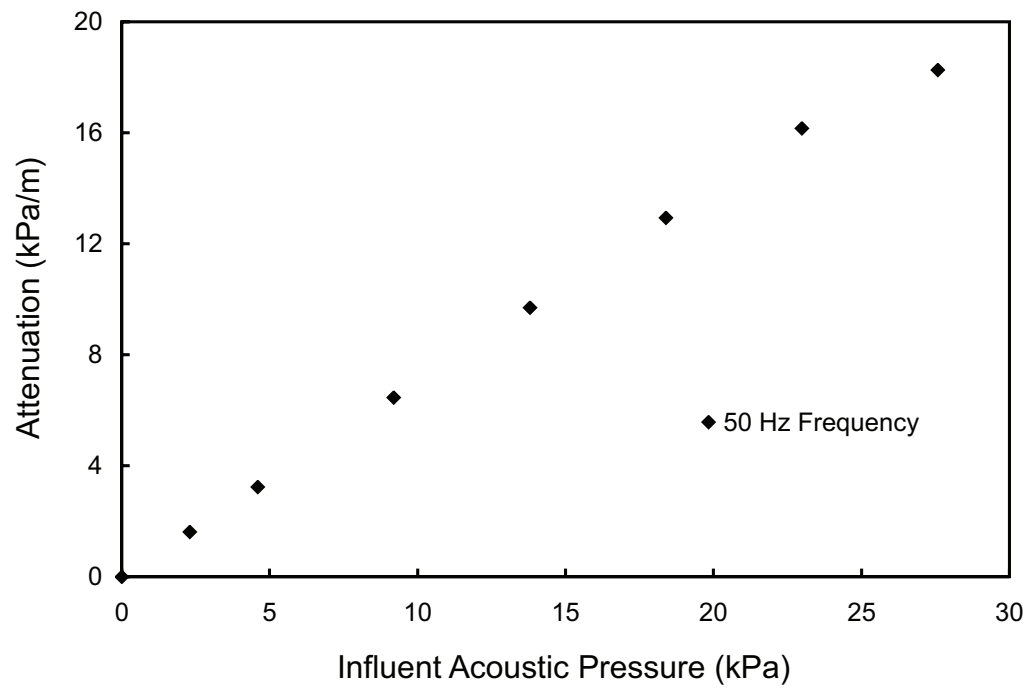


Figure 5.14: The column attenuation in kPa/m for various influent acoustic pressures at a constant acoustic frequency of 50 Hz.

Chapter 6

ACOUSTICALLY ENHANCED GANGLIA DISSOLUTION WITH COLLOIDS

6.1 Chapter Abstract

Finally, the effects of acoustic waves on the transport and dissolution of non-aqueous phase liquid (NAPL) ganglia in the presence of colloids was investigated. Porous media micro-models were fabricated utilizing a photolithographic glass etching and sintering method. A 10 μL sample of Tetrachloroethylene (TCE) was injected into the micromodel to create a single ganglion of TCE. Photographs were taken at regular one hour intervals while flow was maintained through the model. At various intervals acoustic waves were started and the effects were quantified by measurement of the ganglion in photographs and by measurement of the effluent by GC analysis. A solution of bentonite colloids was added and experimental conditions were repeated so that the only change was the addition of colloids. Acoustic waves appear to increase the dissolution of TCE by 50% while the addition of colloids caused an additional dissolution of approximately 5%. However, more quantitative analytical

methods are being developed for this data.

6.2 Introduction

Experimental evidence has shown that acoustic waves can increase both mobilization and dissolution in multi-phase systems (i.e. NAPL/water) [Beresnev and Johnson, 1994; Vogler and Chrysikopoulos, 2004; Chrysikopoulos and Vogler, 2004, 2006]. Thomas and Narayanan [2002] showed that solute mass transfer is enhanced by several orders of magnitude when the fluid medium is subject to oscillatory motion, even if there is no net total flow over a cycle of oscillation. Experimental evidence has shown that effluent aqueous DNAPL concentration increased with the application of acoustic pressure waves with the greatest dissolution enhancement occurring at different frequencies depending upon the experimental setup [Vogler and Chrysikopoulos, 2004; Chrysikopoulos and Vogler, 2004, 2006]. Furthermore, ganglia that were immobile under steady background flow were mobilized when acoustic pressure was added [Chrysikopoulos and Vogler, 2004, 2006]. There is also substantial evidence from both laboratory and field experiments that colloids are efficient sorbents for contaminants such as heavy metals, nonpolar organic compounds (e.g., DNAPL), and radionuclides [Um and Papelis, 2002; Mill et al., 1991; McCarthy, 1998]. However, to the authors knowledge, no one had studied the effects of acoustic waves on DNAPL ganglia dissolution in the presence of colloids.

6.3 Experimental Design and Procedures

Measuring the dissolution of DNAPL with a photographic method requires a thin, pseudo-two-dimensional porous medium so that the total volume of DNAPL in the system can be clearly seen at all times. Etched-glass micromodel pore networks of various geometries were created. First, mask files were created in Adobe Illustrator. A mask file is a black and white negative image representation of a pore channel

geometry desired. Figure 6.1 is an example of the mask file. The image from the mask file is transferred to photographic film to produce a negative film-based image of the channel geometry. The McKeller and Wardlaw [1982] method was used with some modifications, which were developed in the Transport Phenomena Laboratory of the Chemical Engineering Department of the University of Patras in Greece. Figure 6.2 summarizes the important points of the method. Figure 6.3 is a photo of the pore network. Experiments were performed by injecting 100 μL of TCE into the micromodels with steady background flow of 0.1 mL/min. Figure 6.4 shows the injected TCE in the pore network with background flow. An acoustic source generated acoustic waves that traveled through the medium. Experiments were conducted at 0, 30, 50, and 70 Hz frequency and constant influent pressure of 5.75 kPa. Figure 6.5 shows how the TCE is mobilized with the acoustic source. The dissolution and/or mobilization was measured by taking photographs every hour and analyzing the effluent using an HP 5890 Series II Gas Chromatograph (Agilent Technologies, California) with an ECD detector. Once the base case values were obtained, the experiments were repeated with a constant flow of a bentonite colloidal suspension at a concentration of 500 mg/L.

6.4 Preliminary Results and Discussion

The results presented here are qualitative and preliminary in nature. The volume of free-phase TCE in each photograph was determined using the MATLAB® Image Processing Toolbox™. It was clear that in the presence of the colloids, the volume of free-phase TCE remaining in the model decreased at a faster rate. This is due to colloid-facilitated transport. However, in order to correctly quantify the TCE in the system a numerical model is needed to determine the flow and transport of the TCE. This model is under development. Acoustic waves appear to increase the dissolution of TCE by approximately 50% while the addition of colloids caused an additional dissolution of approximately 5%.

6.5 Future Processing

A lattice boltzmann model is being created to model fluid flow conditions in the pore network and to incorporate two-phase flow with DNAPL dissolution.

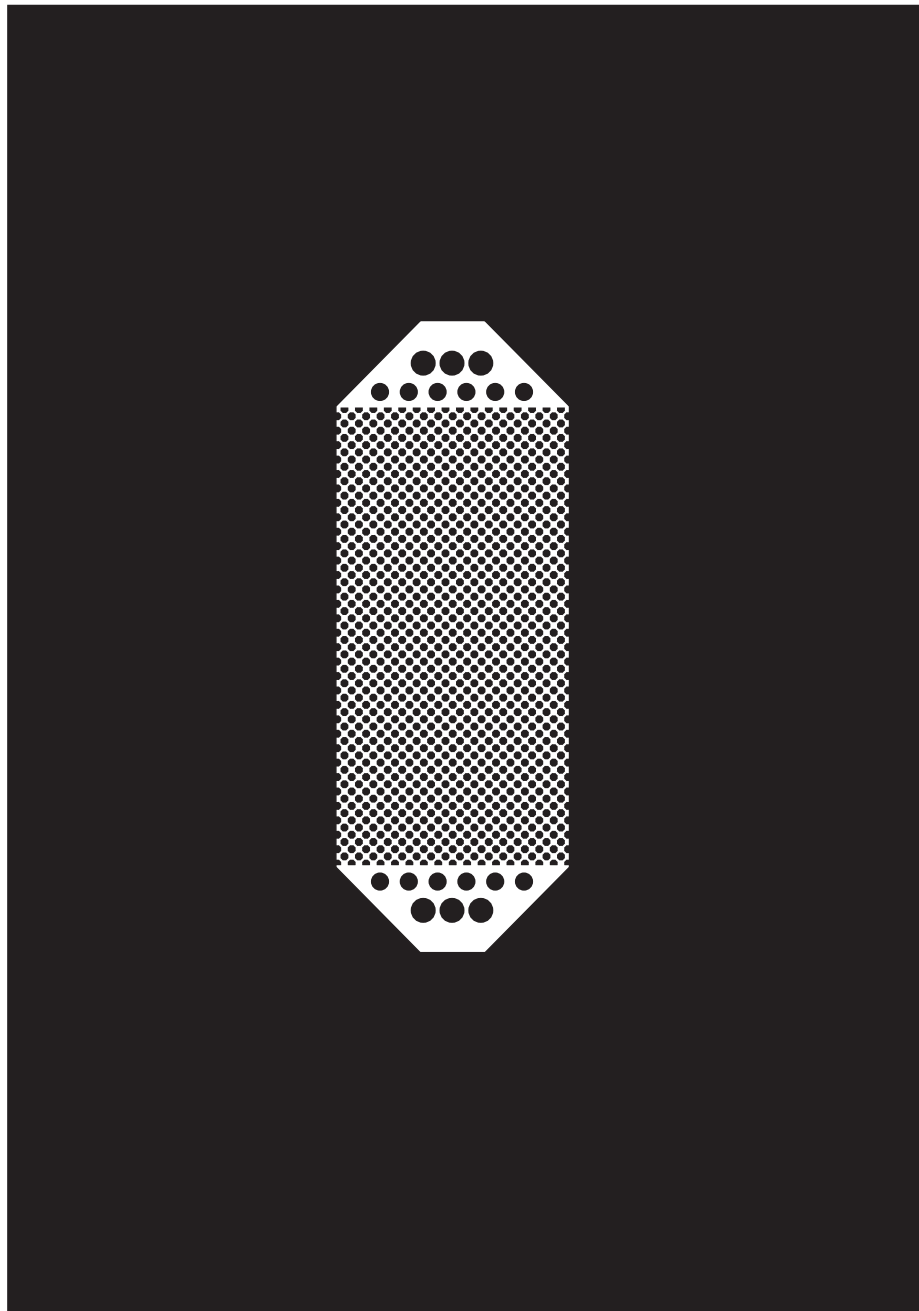


Figure 6.1: A mask file is created, which is a negative image of the pore channel geometry that is desired.

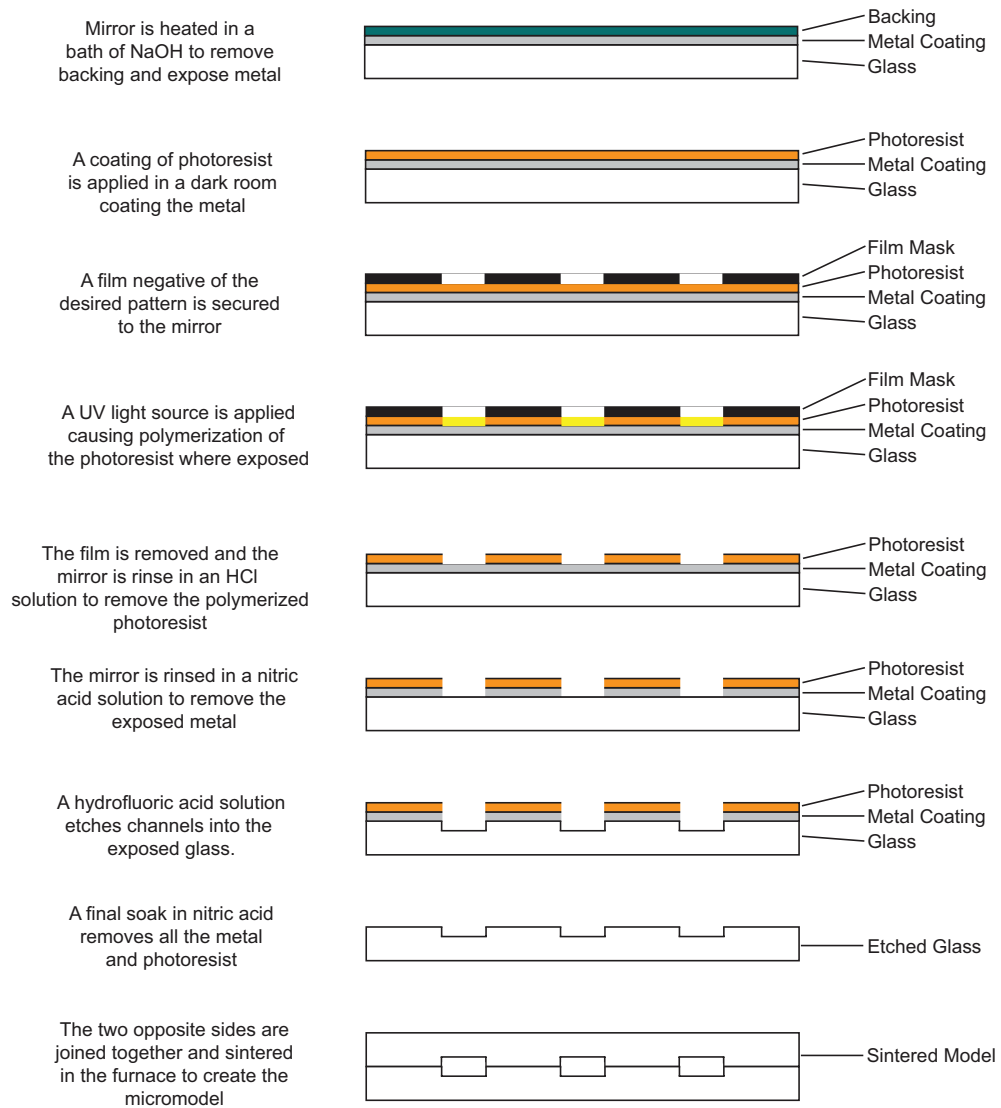


Figure 6.2: An overview of the process used to fabricate etched glass micromodels

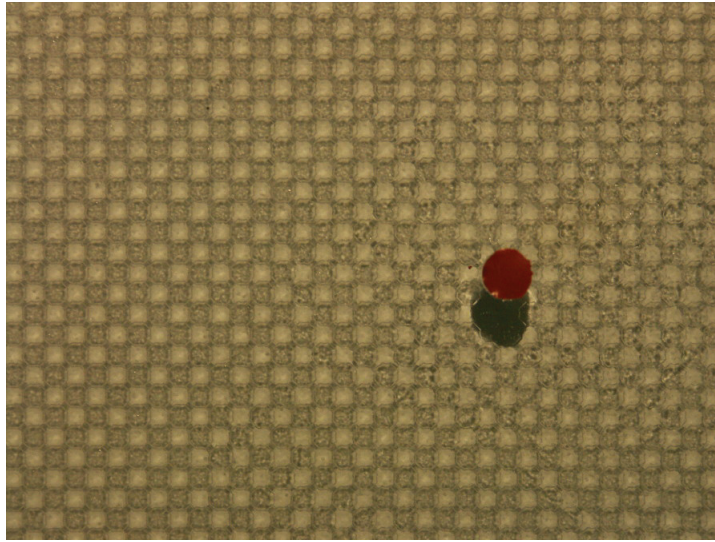


Figure 6.3: A photographs of one of the micromodels that was fabricated and used in the DNAPL studies.

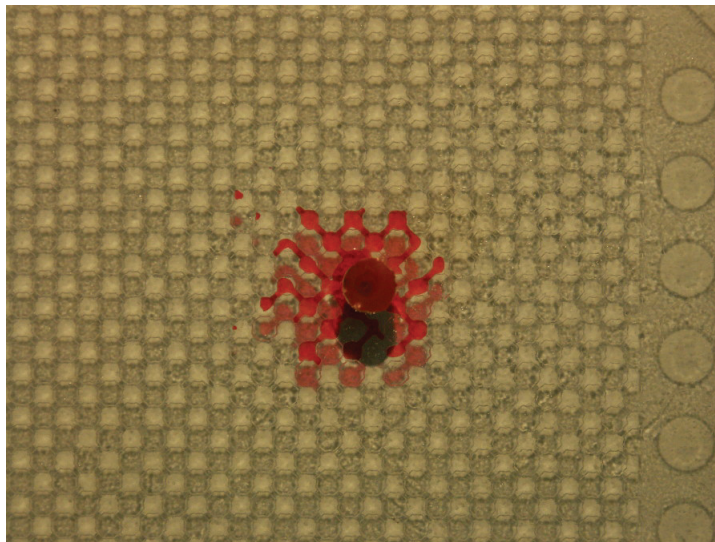


Figure 6.4: A photo of TCE injected in the micromodel.

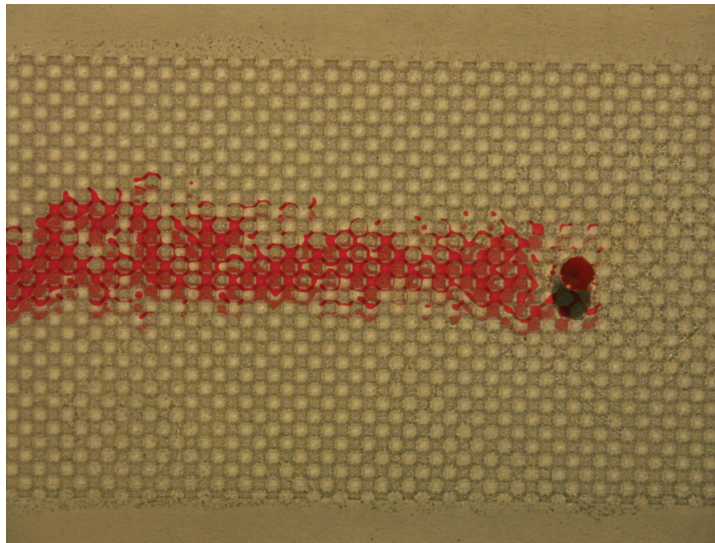


Figure 6.5: The TCE has been mobilized by the acoustic source with colloids present.

REFERENCES

- Abdel-Salam, A.; Chrysikopoulos, C. V. Analytic solutions for one-dimensional colloid transport in saturated fractures, *Adv. Water Resour.*, *17*, 283-296, 1994.
- Abramowitz, M.; Stegun, I. A. eds. *Handbook of Mathematical Functions*, 9th Edition, Dover, Mineola, N. Y., 1972.
- Anders, R.; Chrysikopoulos, C. V. Transport of viruses through saturated and unsaturated columns packed with sand. *Transp. Porous Med.*, *76*, 121-138, 2009; DOI 10.1007/s11242-008-9239-3
- Bao, W. M. J.; Vogler, E. T.; Chrysikopoulos, C. V. Nonaqueous liquid pool dissolution in three-dimensional heterogeneous subsurface formations, *Environ. Geo.*, *43*, 968-977, 2003.
- Barg, S.; Koch, D.; Pulkin, M.; Grathwohl, G. Modeling of glass sintering applied for the fabrication of porous glass bodies. *J. Mater Sci.*, *43*, 483-488, 2008; DOI 10.1007/s10853-007-1873-6
- Baumann T.; Werth, C. J. Visualization and modeling of polystyrol colloid transport in a silicon micromodel. *Vadose Zone J.*, *3*, 434-443, 2004.
- Beresnev, I. A.; Johnson, P. A. Elastic-wave stimultaion of oil production: A review of methods and results, *Geophysics*, *59*, 1000-1017, 1994.
- Biot, M. A. Theory of Propagation of Elastic Waves in a Fluid-Saturated Porous Solid. I. Low-Frequency Range, *J. Appl. Phys.*, *28*(2), 1956a.
- Biot, M. A. Theory of Propagation of Elastic Waves in a Fluid-Saturated Porous Solid. II. Higher Frequency Range, *J. Appl. Phys.*, *28*(2), 1956b.
- Bouhairie, S. A study of the entrapment process in a recirculation flow by video-imaging method. M.S. Thesis, McGill University, Montreal, Canada, 1998.

- Bradford, S. A.; Bettahar, M.; Simunek, J.; van Genuchten, M. Th. Straining and attachment of colloids in physically heterogeneous porous media. *Vadose Zone J.*, 3, 384-394, 2004.
- Bradford, S. A.; Rathfelder, K. M.; Lang, J.; Abriola, L. M. Entrapment and dissolution of DNAPLs in heterogeneous porous media, *J. Contam. Hydrol.*, 67, 133-157, 2003.
- Camesano, T. A.; Unice, K. M.; Logan, B. E. Blocking and ripening of colloids in porous media and their implications for bacterial transport, *Colloids and Surfaces A: Physicochem. Eng. Aspects*, 160, 291-308, 1999.
- Champ, D. R.; Schroeter, J. Bacterial transport in fractured rock: A field-scale tracer test at the Chalk River Nuclear laboratories, *Water Sci. Technol.*, 20, 81-87, 1988.
- Chiou, C. T.; Malcolm, R. L.; Brinton, T. I.; Kile, D. E. Water solubility enhancement of some organic pollutants and pesticides by dissolved humic and fulvic acids, *Environ. Sci. Technol.*, 20(20), 502-508, 1986.
- Chrysikopoulos, C. V.; Vogler, E. T. Acoustically enhanced ganglia dissolution and mobilization in a monolayer of glass beads, *Transp. Porous Media*, 64, 103-121, 2006.
- Chrysikopoulos, C. V.; Vogler, E. T. Acoustically enhanced multicomponent NAPL ganglia dissolution in water saturated packed columns, *Environ. Sci. Technol.*, 38(10), 2940-2945, 2004.
- Chrysikopoulos, C. V.; Hsuan, P.; Fyrrillas, M. M. Bootstrap estimation of the mass transfer coefficient of a dissolving nonaqueous phase liquid pool in porous media, *Water Resour. Res.*, 38(3), 1-8, 2002.
- Chrysikopoulos, C. V.; Abdel-Salam, A. Modeling colloid transport and deposition

- in saturated fractures, *Colloids and Surfaces A: Physicochem. Eng. Aspects*, *121*, 189-202, 1997.
- Chrysikopoulos, C. V.; Sim, Y. One-dimensional virus transport in homogeneous porous media with time-dependent distribution coefficient, *J. Hydrol.*, *185*, 199-219, 1996.
- Chrysikopoulos, C. V. Effective parameters for flow in saturated heterogeneous porous media, *J. Hydrol.*, *170*, 181-198, 1995.
- Chrysikopoulos, C. V.; Kitanidis, P. K.; Roberts, P. V. Generalized Taylor-Aris moment analysis of the transport of sorbing solutes through porous media with spatially-periodic retardation factor, *Transp. Porous Media*, *7*(2), 163-185, 1992.
- Chrysikopoulos, C. V.; Kitanidis, P. K.; Roberts, P. V. Analysis of one-dimensional solute transport through porous media with spatially variable retardation factor, *Water Resour. Res.*, *26*(3), 437-446, 1990.
- Corapcioglu, M. Y.; Bear, J. eds. *Transport Processes in Porous Media*, Kluwer Academic Publishers, Boston, 1991.
- Corapcioglu, M. Y.; Jiang, S. Colloid-facilitated groundwater contaminant transport, *Water Resour. Res.*, *29*, 2215-2226, 1993.
- Dai, Z.; Samper, J. Inverse problem of multicomponent reactive chemical transport in porous media: Formulation and applications. *Water Resour. Res.*, *40*, W07407, 2004; DOI 10.1029/2004WR003248
- DeNovio, N. M.; Saiers, J. E.; Ryan, J. N. Colloid movement in unsaturated porous media: recent advances and future directions. *Vadose Zone J.*, *3*, 338-351, 2004.
- Enfield, C. G.; Bengtsson, G.; Lindqvist, R. Influence of macromolecules on chemical transport, *Environ. Sci. Technol.*, *23*, 1278-1286, 1989.

- Frind, E. O.; Sudicky, E. A.; Schellenberg, S. L. Micro-scale modelling in the study of plume evolution in heterogeneous media. *Stochastic Hydrol. Hydraul.*, 263-279, 1987.
- Gomis-Yagües, V.; Boluda-Botella, N., Ruiz-Beviá, F. Column displacement experiments to validate hydrogeochemical models of seawater intrusions. *J. Contam. Hydrol.*, 29, 81-91, 1997.
- Graham, D. R.; Higdon, J. J. L. Oscillatory forcing of flow through porous media. Part1. Steady flow, *J. Fluid Mech.*, 456, 213-235, 2002.
- Grindrod, P. The impact of colloids on the migration and dispersal of radionuclides within fractured rock, In: J. I. Kim and G. de Marsily (Editors), Chemistry and migration of actinides and fission products, *J. Contam. Hydrol.*, 13, 167-182, 1993.
- Grindrod, P.; Edwards, M. S.; Higgs, J. J. W.; Williams, G. M. Analysis of colloid and tracer breakthrough curves, *J. Contam. Hydrol.*, 21, 243-253, 1996.
- Gross, A.; Besov, A.; Reck, D. D.; Sorek, S.; Ben-Dor, G.; Britan, A.; Palchikov, E. Application of waves for remediation of contaminated aquifers. *Environ. Sci. Technol.*, 37, 4481-4486, 2003.
- Harter, T.; Wagner, S.; Atwill, E. R. Colloid transport and filtration of cryptosporidium parvum in sandy soils and aquifer sediments. *Environ. Sci. Technol.*, 34, 62-70, 2000.
- Hiemenz, P. C.; Rajagopalan, R. Principles of Colloid and Surface Chemistry, Third Edition, Marcel Dekker, Inc. New York, 1997.
- Higgs, J. J. W.; Williams, G. M.; Harrison, I.; Warwick, P.; Gardiner, M. P.; Longworth, G. Colloid transport in a glacial sand aquifer. Laboratory and field studies, *Colloids and Surfaces A*, 73, 179-200, 1993.

- Jin, Y.; Chu, Y.; Li, Y. Virus removal and transport in saturated and unsaturated sand columns. *J. Contam. Hydrol.*, 43, 111-128, 2000.
- Kabala, Z. J.; Sposito, G. A stochastic model of reactive solute transport with time-varying velocity in a heterogeneous aquifer, *Water Resour. Res.*, 27(3), 341-350, 1991.
- Keller, A. A.; Sirivithayapakorn, S.; Chrysikopoulos, C. V. Early breakthrough of colloids and bacteriophage MS2 in a water-saturated sand column. *Water Resour. Res.*, 40(8), W08304, 2004; DOI 10.29/2003WR002676
- Kreft, A.; Zuber, A. Comments on Flux-averaged and volume-averaged concentrations in continuum approaches to solute transport by J. C. Parker and M. Th. van Genuchten, *Water Resour. Res.*, 22(7), 1157-1158, 1986.
- Kretzschmar, R.; Robarge, W. P.; Amoozegar, A. Influence of natural organic matter on transport of soil colloids through saponite, *Water Resour. Res.*, 31, 435-445, 1995.
- Kretzschmar, R.; Sticher, H. Colloid transport in natural porous media: Influence of surface chemistry and flow velocity, *Phys. Chem. Earth*, 23(2), 133-139, 1998.
- Lapidus, L.; Amundson, N. R. Mathematics of adsorption in beds, VI, The effect of longitudinal diffusion in ion exchange and chromatographic columns, *J. Phys. Chem.*, 56, 984-988, 1952.
- Lenhart, J. J.; Saiers, J. E. Colloid mobilization in water-saturated porous media under transient chemical conditions, *Environ. Sci. Technol.*, 37, 2780-2787, 2003.
- Li, Y.; Wang, Y.; Pennell, K. D.; Abriola, L. M. Investigation of the transport and deposition of fullerene (C60) nanoparticles in quartz sand under varying flow conditions. *Environ. Sci. Technol.*, 42, 7174-7180, 2008; DOI 10.1021/es801305y

- Liu, W.; Lo, J.; Tsai, C. On-line method for measurement of the dispersion coefficient of radionuclide migration using a column method. *J. Radioanal. Nucl. Chem.*, *163*(2), 373-384, 1992.
- Loveland, J. P.; Bhattacharjee, S.; Ryan, J. N.; Elimelech, M. Colloid transport in a geochemically heterogeneous porous medium: aquifer tank experiment and modeling, *J. Contam. Hydrol.*, *65*, 161-182, 2003.
- MathWorks, Inc., The. Image Processing Toolbox™ User's Guide; Natick, MA, 2008.
- McCarthy, J. F. Colloid-facilitated transport of contaminants in groundwater: Mobilization of transuranic radionuclides from disposal trenches by natural organic matter, *Phys. Chem. Earth*, *23*, 171-178, 1998.
- McCarthy, J. F.; Wobber, F. J. eds. Manipulation of Groundwater Colloids for Environmental Restoration, Lewis Publishers, Boca Raton, Florida, 1993.
- McCarthy, J. F.; Zachara, J. M. Subsurface transport of contaminants, *Environ. Sci. Technol.*, *23*, 496-502, 1989.
- McKellar, M.; Wardlaw, N. C. A method of making two-dimensional glass micro-models of pore systems, *J. Can. Petrol. Technol.*, *21*, 1-3, 1982.
- Mill, W. B.; Liu, S.; Fong, F. K. Literature review and model (COMET) for colloid/metals transport in porous media, *Ground Water*, *29*, 199-208, 1991.
- Niehren, S.; Kinzelbach, W. Artificial colloid tracer tests: development of a compact on-line microsphere counter and application to soil column experiments, *J. Contam. Hydrol.*, *35*, 249-259, 1998.
- O'Melia, C. R.; Hahn, M. W.; Chen, C. T. Some effects of particle size in separation processes involving colloids, *Water Sci. Technol.*, *36*, 119-126, 1997.
- Parker, J. C.; van Genuchten, M. Th. Flux-averaged and volume-averaged concen-

- trations in continuum approaches to solute transport. *Water Resour. Res.*, 20(7), 866-872, 1984.
- Plona, T. J. Observation of a second bulk compressional wave in a porous medium at ultrasonic frequencies. *Appl. Phys. Lett.*, 36(4), 259-261, 1980; DOI 10.1063/1.91445
- Prado, M. O.; Fredericci, C.; Zanutto, E. D. Isothermal sintering with concurrent crystallization of polydispersed soda-lime-silica glass beads. *J. Non-Cry. Sol.*, 331, 145-156, 2003; DOI 10.1016/j.jnoncrysol.2003.08.076
- Reimus, P. W.; Robinson, B. A.; Nuttall, H. E.; Kale, R. Simultaneous transport of synthetic colloids and a nonsorbing solute through single saturated natural fractures, *Mat. Res. Soc. Symp. Proc.*, 353, 363-370, 1995.
- Roberts, P. M.; Sharma, A.; Uddameri, V.; Monagle, M.; Dale, D. E.; Steck, L. K. Enhanced DNAPL transport in a sand core during dynamic stress stimulation. *Environ. Eng. Sci.*, 18(2), 67-79, 2001.
- Roberts, G. E.; Kaufman, H. *Table of laplace Transforms*, W. B. Saunders, Philadelphia, Pennsylvania, 1966.
- Rockhold, M. L.; Yarwood, R. R.; Niemet, M. R.; Bottomley, P. J.; Selker, J. S. Experimental observations and numerical modeling of coupled microbial and transport processes in variably saturated sand. *Vadose Zone J.*, 4, 407-417, 2005; DOI 10.2136/vzj2004.0087
- Shang, J.; Flury, M.; Chen, G.; Zhuang, J. Impact of flow rate, water content, and capillary forces on in situ colloid mobilization during infiltration in unsaturated sediments. *Water Resour. Res.*, 44, W06411, 1-12, 2008; DOI 10.1029/2007WR006516
- Sim, Y.; Chrysikopoulos, C. V. Analytical models for one-dimensional virus trans-

- port in saturated porous media, *Water Resour. Res.*, *31*(5), 1429-1437, 1995.
(Correction, *Water Resour. Res.*, *32*(5), 1473, 1996)
- Srivithayapakorn, S.; Keller, A. Transport of colloids in saturated porous media: A pore-scale observation of the size exclusion effect and colloid acceleration, *Water Resour. Res.*, *39*, 1-9, 2003.
- Smith, P. A.; Degueudre, C. Colloid-facilitated transport of radionuclides through fractured media, *J. Contam. Hydrol.*, *13*, 143-166, 1993.
- Spiegel, M. R. Schaum's outline of theory and problems of Laplace transforms, McGraw-Hill, New York, 1990.
- Stumm, W. Aquatic Colloids As Chemical Reactants: Surface Structure and Reactivity, *Colloids and Surfaces A*, *73*, 1-18, 1993.
- Sutton, D. J.; Kabala, Z. J.; Francisco, A.; Vasudevan, D. Limitations and potential of commercially available rhodamine WT as a groundwater tracer. *Water Resour. Res.*, *37*(6), 1641-1656, 2001.
- Tatalovich, M. E.; Lee, K. Y.; Chrysikopoulos, C. V. Modeling the transport of Contaminants originating from the dissolution of DNAPL pools in aquifers in the presence of dissolved humic substances, *Trans. Porous Media*, *38*, 93-115, 2000.
- Tien, N.; Li, S. Transport of a two-member decay chain of radionuclides through a discrete fracture in a porous rock matrix in the presence of colloids, *Nuc. Technol.*, *140*, 83-93, 2002.
- Thomas, J. M., and C. V. Chrysikopoulos. Experimental investigation of acoustically enhanced colloid transport in water-saturated packed columns. *J. Colloid and Interface Sci.*, *308*, 200-207, 2007; DOI 10.1016/j.jcis.2006.12.062
- Thomas, A. M.; Narayanan, R. A comparison between the enhanced mass transfer

- in boundary and pressure driven oscillatory flow, *Int. J. Heat and Mass Transf.*, *45*, 4057-4062, 2002.
- Tufenkji, N. Modeling microbial transport in porous media: Traditional approaches and recent developments. *Adv. Water Resour.*, *30*, 1455-1469, 2007.
- Valocchi, A. J. Spatial moment analysis of the transport of kinetically adsorbing solutes through stratified aquifers, *Water Resour. Res.*, *25*(2), 273-279, 1989.
- Van Genuchten, M. Th.; Parker, J. C. Boundary conditions for displacement experiments through short laboratory soil columns. *Soil Sci. Soc. Am. J.*, *48*, 703-708, 1984.
- Vogler, E. T.; Chrysikopoulos, C. V. An experimental study of acoustically enhanced NAPL dissolution in porous media. *AIChE Journal*, *50*(12), 3271-3280, 2004; DOI 10.1002/aic.10221
- Vogler, E. T.; Chrysikopoulos, C. V. Experimental investigation of acoustically enhanced solute transport in porous media. *Geophysical Res. Lett.*, *29*(15), 1-4, 2002; DOI 10.1029/2002GL015304
- Vogler, E. T.; Chrysikopoulos, C. V. Dissolution of nonaqueous phase liquid pools in anisotropic aquifers, *Stochastic Environ. Res. Risk Assess.*, *15*, 33-46, 2001.
- Weroniski, P.; Walz, J. Y.; Elimelech, M. Effect of depletion interactions on transport of colloidal particles in porous media, *J. Colloid Int. Sci.*, *262*, 372-383, 2003.
- Zhang, W. Nanoscale iron particles for environmental remediation: an overview. *J. Nanoparticle Res.*, *5*, 323-332, 2003.
- Zhuang, J.; Jin, Y. Virus retention and transport through Al-oxide coated sand columns: effects of ionic strength and composition. *J. Contam. Hydrol.*, *60*, 193-209, 2003.